Complex deformation at shallow depth during the 30 October 2016 Mw6.5 Norcia earthquake: interference between tectonic and gravity processes?

Arthur Delorme, Raphael Grandin, Yann Klinger, Marc Pierrot-Deseilligny, Nathalie Feuillet, Eric Jacques, E. Rupnik, Yu Morishita

Tectonics

RESEARCH ARTICLE
10.1029/2019TC005596

Special Section:
The 2016 Central Italy Seismic Sequence: Insights, implications and lessons learned

Complex Deformation at Shallow Depth During the 30 October 2016 M_w6.5 Norcia Earthquake: Interference Between Tectonic and Gravity Processes?

A. Delorme[1], R. Grandin[1], Y. Klinger[1], M. Pierrot-Deseilligny[2], N. Feuillet[1], E. Jacques[1], E. Rupnik[2], and Y. Morishita[3]

[1]Université de Paris, Institut de physique du globe de Paris, CNRS, F-75005, Paris, France, [2]LaSTIG, IGN, ENSG, Université de Paris-Est F-94160, Saint-Mandé, France, [3]Geospatial Information Authority of Japan, Tsukuba, Japan

Abstract The relation between slip at the near surface and at depth during earthquakes is still not fully resolved at the moment. This deficiency leads to large uncertainties in the evaluation of the magnitude of past earthquakes based on surface observations, which is the only accessible evidence for such events. A better knowledge of the way slip distributes over distinct rupture strands within the first few kilometers from the surface would contribute greatly to reduce these uncertainties. The 30 October 2016 M_w6.5 Norcia earthquake has been captured by a variety of geodetic techniques, which provide access to the slip distribution both at depth and at the ground surface, with an unprecedented level of detail for a normal-faulting earthquake. We first present coseismic surface offset measurements from correlation of optical satellite images of submetric resolution, which are compared to field observations made shortly after the earthquake. Based on a joint inversion of optical data together with InSAR and GPS data, we then propose a rupture model that explains the observations both at far-field and near-field scales. Finally, we explore different rupture geometries at shallow depth, in an attempt to better explain the near-field deformation (i.e., within the first hundreds of meters around the fault) observed at the surface. Despite the fact that the solution is not unique, several lines of evidence suggest that gravity processes could be locally involved, which interfere with the dominant tectonic processes.

Key Points:
- Correlation of optical images covering the Norcia earthquake allows inference of the slip distribution at depth and at the surface
- Decrease of slip toward the surface inferred from elastic modeling of interferograms contradicts high slip values measured at the surface
- Gravity processes, which interfere with dominant tectonic processes, could be locally involved and explain slip excess at the surface

Supporting Information:
- Supporting Information S1
- Table S2
- Table S3

Correspondence to:
A. Delorme,
delorme@ipgp.fr

Citation:
Delorme, A., Grandin, R., Klinger, Y., Pierrot-Deseilligny, M., Feuillet, N., Jacques, E., et al. (2020). Complex Deformation at Shallow Depth During the 30 October 2016 M_w6.5 Norcia Earthquake: Interference Between Tectonic and Gravity Processes? *Tectonics*, *39*, e2019TC005596. https://doi.org/10.1029/2019TC005596

Received 22 MAR 2019
Accepted 24 DEC 2019
Accepted article online 3 JAN 2020

1. Introduction

Between August 2016 and January 2017, the Central Apennines region in Italy was struck by an earthquake sequence (Figure 1), which included three moderate to large events (Chiaraluce et al., 2017). This sequence caused 299 fatalities and severely damaged buildings and infrastructures in a region of 20 km by 40 km around the epicenter (Galli et al., 2017).

On 24 August 2016, the sequence started with a M_w6.0 earthquake that occurred close to the towns of Accumoli and Amatrice. Two months later, on 26 October 2016, a second earthquake, with magnitude M_w5.9, hit ~25 km NNW from the first earthquake, near the town of Visso. On 30 October 2016, the third and largest event, with a magnitude of M_w6.5, occurred close to the town of Norcia. This third earthquake is the largest Italian earthquake since the 1980 M_w6.9 Irpinia earthquake. Finally, on 18 January 2017, a series of four smaller events, with magnitude culminating at 5.5 (Chiaraluce et al., 2017), occurred 10 km south of Amatrice.

Overall, the 2016–2017 sequence ruptured NW-SE oriented, mainly SW dipping, normal fault systems over a length of 60 km (Chiaraluce et al., 2017).

The sequence is located in-between the two previous largest normal-faulting sequences that occurred along the Apennines (Figure 1; Chiaraluce et al., 2017, and references therein): To the NW, the 1997 M_w6.0 Umbria-Marche sequence ruptured a 40-km-long SW dipping fault system; to the SE, the 2009 M_w6.1 L'Aquila sequence ruptured a 50-km-long SW dipping fault system.

Currently in the Apennines, extension in a NE direction is occurring at a rate of ~1.6 to 3 mm/year, which is accommodated through such moderate- to large-magnitude (M6.0–7.0) earthquakes (D'Agostino, 2014). Evidence for historical earthquake sequences sharing similar features with the 1997, 2009, and 2016–2017

10.1029/2019TC005596

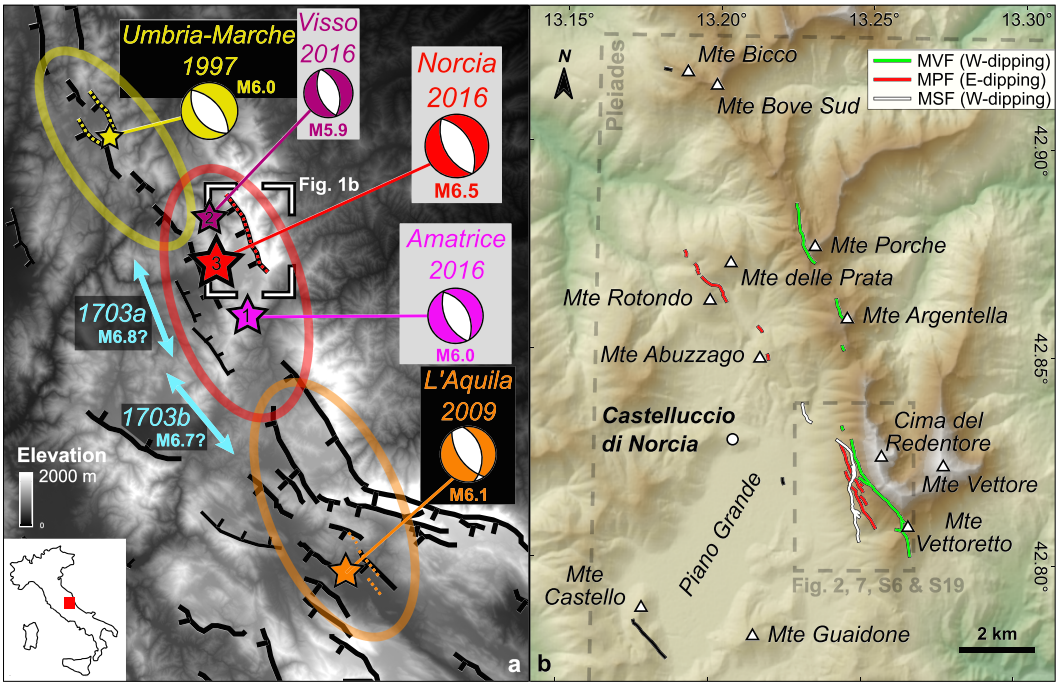

Figure 1. (a) General view of the Central Apennine in Italy, with the major active normal faults in black (mapping from Schlagenhauf, 2009; Schlagenhauf et al., 2011). The 1703 historical earthquakes are indicated with their estimated extensions (in cyan; Cello et al., 1998; Galadini & Galli, 2000). The ellipses show the extent of the two previous largest normal-faulting sequences that occurred along the Apennines—Umbria-Marche (1997; in yellow) and L'Aquila (2009; in orange)—and of the 2016–2017 sequence (in red). Surface ruptures associated with these sequences (Cinti et al., 2000; 2009: EMERGEO Working Group, 2010; 2016: this study) are indicated by thin colored dashed lines. The focal mechanisms and moment magnitudes correspond to the main events of these sequences (Lundgren & Stramondo, 2002; 2009: Walters et al., 2009; 2016: TDMT solutions for the three mainshocks [http://cnt.rm.ingv.it/]). For the 2016–2017 sequence, the area affected by the 30 October Norcia earthquake (3) is located between the two areas affected by the 24 August Amatrice (1) and 26 October Visso (2) previous events. (b) Close-up view of the studied area (see the white box in Figure 1a for location) with the 30 October coseismic ruptures mapped from the Pleiades results: in green the ruptures associated with the west dipping "Monte Vettore" fault (MVF); in red those associated with the east dipping "Monte delle Prata" fault (MPF); in white the ruptures associated with the west dipping "Middle Slope" fault (MSF). The remaining mapped ruptures are represented in black. The Pleiades images common footprint is indicated by a dashed line. The background image is a shaded relief map derived from the ALOS World 3D topography from JAXA (http://www.eorc.jaxa.jp/ALOS/en/aw3d30). Locations names after Civico et al. (2018).

sequences has long been reported in the literature (e.g., Boschi et al., 2000; Guidoboni et al., 2007, and references therein). These sequences are generally interpreted as representing the individual events, that together build the spectacular Holocene fault scarps observed in the field, such as the Magnola fault or the Norcia fault (e.g., Blumetti et al., 1993; Galadini & Galli, 2000; Piccardi et al., 1999). Surface offsets associated with the largest of these past earthquakes are recognized in paleoseismic trenches and by cosmogenic dating of incremental exhumation of limestone bedrock along fault scarps, thereby providing a foundation for assessing earthquake recurrence intervals (e.g., Galli et al., 2005; Palumbo et al., 2004; Pantosti et al., 1996; Schlagenhauf et al., 2011).

However, it remains difficult to derive earthquake magnitude from fault offsets measured at paleoseismic sites, even in cases of complete and useful stratigraphy. Indeed, along-strike variability of slip distribution (Rockwell et al., 2002) is often not known for past earthquakes due to sparseness of measurements and, even at one individual site, relations between coseismic slip at depth and in the near surface are not yet fully understood. This lack of understanding partly stems from the difficulty to properly measure the slip distribution and fault geometry at depth during large surface-rupturing earthquakes, as this information is actually contained in the off-fault elastic deformation field, which is inaccessible in the absence of preearthquake

observations. Actually, the full amount of coseismic offsets at the surface is often difficult to recognize and to measure accurately in the field, especially when deformation occurs on many individual faults forming a broad, distributed fault zone (Klinger et al., 2018; Vallage et al., 2015), as it is often the case for normal-faulting earthquakes (e.g., Caskey et al., 1996; EMERGEO Working Group, 2010; Jacques et al., 2011; Meyer et al., 1996). On the other hand, far-field deformation, which is best captured by space geodetic techniques such as interferometric synthetic aperture radar (InSAR), allows for retrieving reasonably well the slip distribution at depth through solving an inverse problem (Saint Fleur et al., 2015). Conversely, retrieving near-fault deformation at the surface from InSAR is often hampered by a combination of factors including (1) the loss of coherence in the near-field due to surface changes or extreme strain, (2) the limited spatial resolution of the images, and (3) discontinuities of surface ruptures and existence of local ruptures not directly related to primary faulting (e.g., Guerrieri et al., 2010; Meyer et al., 1996). For these reasons, scaling laws relating surface slip to earthquake magnitude (e.g., Wells & Coppersmith, 1994) rely on limited data and overly simplistic assumptions, leading to substantial epistemic uncertainty when it comes to estimating rupture parameters for past earthquakes.

Here, we first derive the three-dimensional coseismic surface deformation for the 30 October 2016 M_w6.5 Norcia event from the correlation of optical satellite images of submetric resolution (hereafter VHR, for very high resolution). Then, from surface deformation maps, for every fault strand we can identify (i.e., when the deformation signal exceeds the detection threshold), we extract a slip distribution for both the horizontal and the vertical components of the slip vector at the surface. These slip measurements are compared and validated against field measurements compiled by the Open EMERGEO Working Group (Civico et al., 2018; Villani, Civico, et al., 2018). Eventually, we perform a joint inversion of InSAR, GPS, and optical data to propose a rupture model that explains both the far-field and near-field observations. Our modeling indicates that some degree of horizontal, slope-parallel deformation, possibly of gravitational origin, is needed, in addition to dominant tectonic deformation, to explain at best the different data sets, although at this stage the detail of model geometry remains nonunique.

2. Optical Satellite Data

Image correlation techniques allow for analyzing differences between images acquired respectively before and after an earthquake to measure horizontal coseismic displacements at the ground surface (Leprince et al., 2007; Michel et al., 1999a, 1999b; Van Puymbroeck et al., 2000). The smallest detectable displacement is directly related to the image resolution and is about 0.05 pixels at best (Leprince et al., 2007). This accuracy can only be achieved under specific conditions: (1) a precise knowledge of the geometry of acquisition and (2) the use of an accurate digital surface model (DSM) to correct for nontectonic sources of distortions within the images (e.g., the geometry of the sensor, the topography, the relative position between images, i.e., the stereoscopic effect). Furthermore, limited temporal changes between images acquired at different dates are required to avoid decorrelation. This technique has been used to describe coseismic earthquake ruptures (i.e., Binet & Bollinger, 2005; Klinger et al., 2018; Socquet et al., 2019; Vallage et al., 2015, 2016), rifting events (i.e., Grandin et al., 2009; Hollingsworth et al., 2013), glacial flow (Berthier et al., 2005; Heid & Kääb, 2012), and landslides (Booth et al., 2013; Stumpf et al., 2014).

2.1. Data Processing

The technique described here has been commonly used during the last two decades to process images with decametric resolution (Dominguez et al., 2003; Grandin et al., 2009; Klinger et al., 2006). However, the recent advent of VHR satellite images introduced some new complexities in the processing that calls for a detailed description.

The Pleiades 1A and 1B satellites provide images with a ground sampling distance of 50 cm for the panchromatic band. Under optimal conditions, such data should thus allow for measuring horizontal surface displacements at centimeter scale. This threshold is appropriate to capture the horizontal surface displacement that is expected for a normal-faulting earthquake of magnitude 6 or larger. To be able to measure accurately the coseismic displacement, all other distortions must be accounted for. Hence, first, images are orthorectified to a cartographic projection to remove the effects of the sensor geometry and topography. To limit as much as possible the impact of stereoscopy, images are selected with the closest possible angles of incidence and also as close as possible to nadir. The larger the stereoscopic effect, the more residual topographic

artifacts should be expected. However, with modern VHR satellites (such as Pleiades), which operate in agile modes, obtaining two images acquired at different dates that comply with such angular constraints is difficult. To address this problem, for each date, a stereo acquisition can be processed to derive a high-resolution DSM, later used in the orthorectification process, thus improving the accuracy of the generated orthoimages.

In this work, we obtained two Pleiades tri-stereo acquisitions (i.e., two sets of three images), with the first acquisition on 29 October 2016, before the 30 October 2016 event, and the second acquisition after the event, on 1 December 2016 (Table 1). It is worth noting that (1) the 26 October 2016 earthquake is not captured by this data set; (2) about 1 month of postseismic signal also contributes toward the coseismic signal. The data are processed with MicMac, a free open-source software for photogrammetry (Pierrot-Deseilligny & Paparoditis, 2006; Rosu et al., 2015; Rupnik et al., 2017). To deal with computational limitations, processing is divided into two geographical zones, north and south. Each image is cropped accordingly and new RPCs (rational polynomial coefficients, which describe the geometry of acquisition of the image) are computed from the initial RPCs, to fit the smaller area. To better constrain the geometry, for each zone, RPC-based bundle block adjustment—that is, the geometries of all the acquisitions are refined during a single process, based on a least squares method—is performed (Rupnik et al., 2016), using all six images as input. This way the geometry of a given image, besides being better constrained, is consistent within the whole data set, which allows producing coregistered DSMs and orthoimages. Reprojection residuals of the tie points between the images, before and after the process, are shown in Table S1 in the supporting information. For each zone, the refined geometry enables a localization precision in the range of 0.4 pixels, corresponding to 20 cm on the ground.

During bundle block adjustment, all tie points between images acquired at different dates are considered as relating to the same coordinates on the ground. However, for zones affected by the earthquake deformation, this assumption is not valid, because target pixels moved as a result of coseismic displacement. Nevertheless, such violation in our assumptions is not critical as changes in geometry introduced by these erroneous tie points are characterized by long wavelength, whereas the tectonic signal has a short wavelength. Hence, the tectonic signal is not significantly affected, as shown by comparison of deformation maps derived from ALOS-2 and Pleiades (see section 3.1).

From this point on, the preevent and postevent images are processed separately to produce, in each case, a DSM and three orthoimages at ground sampling distance equal to 0.5 m. Then, subpixel correlation is performed on each pair of preevent and postevent orthoimages. Thanks to MicMac capability to handle a small correlation window (in our case 9 by 9 pixels) with a low level of noise (Rosu et al., 2015), two 0.5-m resolution horizontal surface deformation maps are obtained, one for the E-W deformation and one for the N-S deformation (Figures 2a and S1). This enables us to fully benefit from the high resolution of modern optical satellites, in order to investigate details of geometric complexities along the earthquake ruptures.

Besides being used for active fault mapping and orthorectification of the images, the preevent and postevent DSMs can also be used to assess the vertical component of the deformation. A vertical deformation map is computed (Figures 2b and S1), taking into account the horizontal deformation field obtained during the previous step (Figure 2e); the DSMs and horizontal deformation maps being coregistered, for each pixel of the preevent DSM, the corresponding horizontal displacement value is used to locate the same pixel in the postevent DSM. By subtracting the altitudes at the respective positions in the two DSMs, we are able to estimate the change in elevation for each pixel. This approach eliminates the effect of spurious elevation changes that would appear with a direct DSMs subtraction, in case of a combination of horizontal motion and preexisting topographic slope (Mackenzie & Elliott, 2017).

To mitigate noise and especially spatial aliasing in the horizontal deformation maps, we take advantage of the redundancy in our results. Weighted average of the nine maps that were previously calculated (one for each pair of orthoimages) is computed, using the correlation score generated during the correlation steps as the weight, to obtain, for each direction, a map of average deformation. Although we performed no quantitative assessment of the noise level evolution, the result shows a noticeable visual decrease of the noise, while the signal is well preserved (Figure S2).

Several additional sources of noise are also identified, which can be at least partly addressed. Inaccuracies in the estimation of the satellite attitude lead to residual signals in the correlation maps. The dominant residual

Table 1
Information Relative to the Pleiades and ALOS-2 Data Used to Study the 30 October Norcia Earthquake

Pleiades tri-stereo	Date	Scene ID
Preearthquake	29/10/2016 10:07 UTC	DS_PHR1B_201610291007430_FR1_PX_E013N42_0418_03676
Postearthquake	01/12/2016 10:03 UTC	DS_PHR1B_201612011003473_FR1_PX_E013N42_0420_02408

ALOS-2	Date	Path
Preearthquake	24/08/2016	Ascending
Preearthquake	31/08/2016	Descending
Preearthquake	28/10/2016	Ascending
Postearthquake	02/11/2016	Ascending
Postearthquake	09/11/2016	Descending
Postearthquake	11/11/2016	Ascending

Note. Dates are formatted as DD/MM/YYYY.

signal, in the satellite across-track direction, relates to pitch variations. The wavelength of this signal is long in comparison with the tectonic deformation. In addition, in our case, this residual signal is almost perpendicular to the ruptures. Thus, the impact of this residual signal on our analyses should be limited. To reduce the impact of this signal further, we extract stacked profiles from a region with no significant tectonic signal to fit a long wavelength spline function, which is next subtracted from the deformation map. A second residual signal, in the satellite along-track direction, relates to charge-coupled device misalignments and jitter artifacts (Ayoub et al., 2008). In our case, the direction of this signal is almost parallel to the ruptures direction. As there is no wide-enough area free from tectonic signal where its spectral pattern could be estimated, it is impossible to correct this artifact following similar methodology as previously for the across-track artifact, without jeopardizing the tectonic signal. Despite the use of high-resolution DSMs in the orthorectification process, some residual topographic artifacts are still visible in the deformation maps (Figure S2), which cannot be fully corrected. Finally, temporal changes (snow and shadows in particular) between the two tri-stereo acquisitions, which are 33 days apart, lead to poor correlation scores in certain areas, where horizontal surface offset measurements are therefore more difficult to perform, if not impossible.

As for the horizontal surface deformation maps, some noise is also present in the vertical map. Similarly to what was done for the horizontal deformation results, a long wavelength, across-track pattern is estimated and removed. The impact of temporal changes between the two tri-stereo acquisitions, however, remains limited on the vertical map, as each DSM is computed with images acquired in a single pass, which limits potential for decorrelation.

2.2. Coseismic Offsets Measurements

In the following, we use the terms defined in Mackenzie and Elliott (2017) for the different components of the slip vector: lateral slip (horizontal, along strike), heave (horizontal, strike perpendicular), throw (vertical), and dip slip (the vector sum of heave and throw).

Detailed mapping of the coseismic surface ruptures from aerial images and field observations is available in Civico et al. (2018). We also map coseismic surface ruptures in detail (Figure 1b), using the computed horizontal and vertical surface deformation maps, DSMs, and orthoimages (Figure S3). In a second step, the mapping is slightly simplified: (1) The sinuosity is reduced manually. This way the measurements performed are less sensitive to very local, potentially large changes in the rupture azimuth; (2) small, discontinuous surface ruptures are grouped in a single line. Stacked profiles are generated along each rupture every 30 m in 30-m-wide, 750-m-long boxes (Figure 2), using the dedicated tool available in the COSI-Corr software (Leprince et al., 2007), to measure surface offsets in both horizontal and vertical directions (Tables S2 and S3). In places where deformation is distributed across multiple subparallel fault strands, we pay attention to constrain our offset measurement using only data located in direct vicinity of the rupture. This is in order to ensure that comparison with field data is meaningful (see section 2.3). Furthermore, measurements impacted by short wavelength topographic artifacts—for example, a drainage channel cutting through the rupture—are discarded.

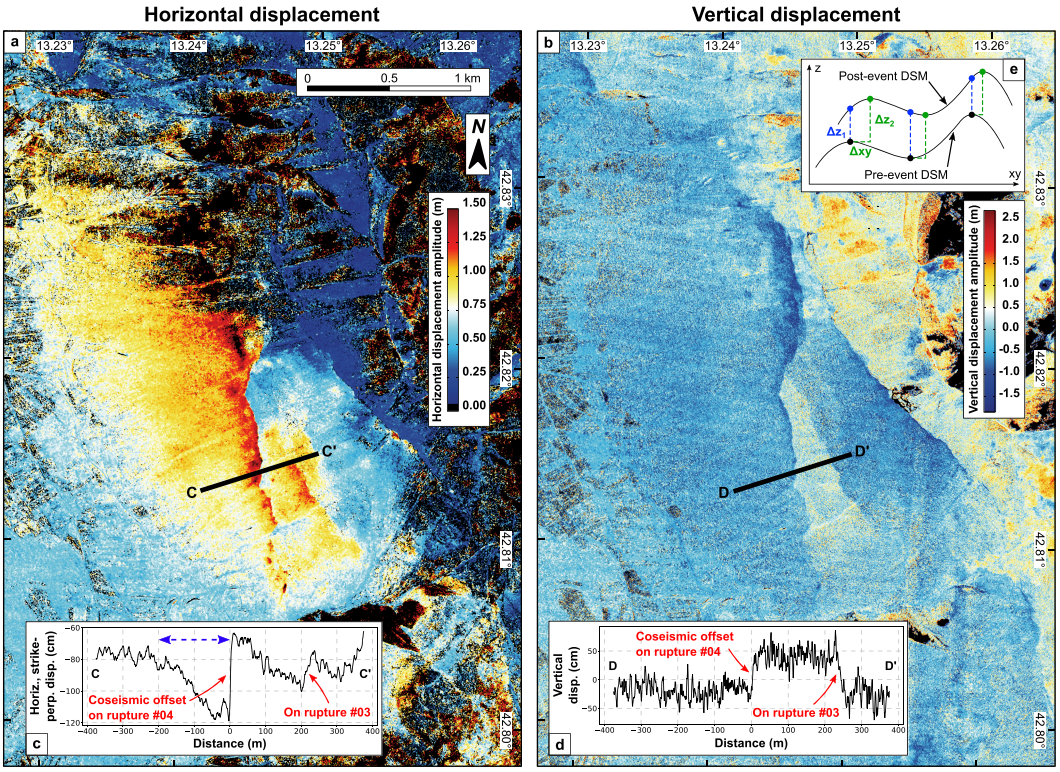

Figure 2. Subset of the (a) horizontal—absolute amplitude of the displacement—and (b) vertical surface deformation maps in the Monte Vettore area (see Figure 1b for location), where multiple surface ruptures with metric offsets are clearly visible. Pixels for which the correlation score—from the orthoimages correlation process, which produces the horizontal deformation maps, for (a); from both DSMs computation for (b)—is less than 0.1 appear in black. For (a), pixels for which the displacement is larger than 3 m also appear in black. According to our measurements and to Villani, Civico, et al. (2018), the horizontal displacement never reaches this threshold. Therefore, amplitudes above 3 m can be considered as bad correlation results. Coseismic offsets (see Figures 3 and 4) are measured on stacked profiles in 30-m-wide, 750-m-long boxes, every 30 m along the ruptures. (c) (respectively d) shows the amplitude of the horizontal displacement perpendicular to the local azimuth of the rupture trace (respectively vertical displacement) along Stacked Profile C-C′ (respectively D-D′). In this example, a positive heave (i.e., the difference between the displacement east of the rupture and the displacement west of the rupture is positive) on Ruptures #03 and #04 (see the map in Figure 3a) denotes extension, that is, normal faults, and a positive throw on Rupture #04 (respectively a negative throw on Rupture #03) implies that this normal fault is dipping toward the west (respectively east). Displacement values are relative in those maps (no reference is set), so only displacement differences have a meaning. (e) Summary of the approach used to compute the vertical deformation map. During the earthquake, deformations affected the surface. A direct approach (in blue) consists of a pixel-to-pixel difference to obtain a vertical displacement Δz_1. The approach adopted in this study (in green) makes use of the horizontal deformation maps to obtain a vertical displacement Δz_2.

On the western flank of Monte Vettore, a complex 3.6-km-long, N155°E trending network of ruptures, both synthetic and antithetic to the principal dip direction—toward the SW—(Chiaraluce et al., 2017; Villani, Civico, et al., 2018; Brozzetti et al., 2019) was activated. In this area, measurements made in our deformation maps show a median of 25 cm for the heave and of 37 cm for the throw (ruptures in green, white, and red colors in the small dashed rectangle in Figure 1b). Located on multiple subparallel fault strands, 15% of the heave measurements exceed 50 cm (with a maximum of 145 cm) and 9% of the throw measurements exceed 1 m (with a maximum of 193 cm). Monte Rotondo, 6 km NE of Monte Vettore, is cut by a 1-km-long NE dipping antithetic N40°W striking rupture (red line in Figure 1b), on which the median values for heave and throw are equal to 36 and 37 cm, respectively. Facing Monte Rotondo, 6 km north of Monte Vettore, Monte Porche is cut by a 1.6-km-long, N170°E striking synthetic rupture (green line in Figure 1b), on which the median values for heave and throw are equal to 24 and 43 cm respectively. SW of Piano Grande, on Monte Castello, a 1.3-km-long, N140°E striking rupture (black line in Figure 1b) was also activated, with

no significant heave nor throw—the median values are equal to 1 and 0 cm, respectively—but right-lateral strike slip with a median value equal to 21 cm (Figure S4).

2.3. Measurements From Deformation Maps and Comparison With Field Data

Systematic offset measurements are performed every 30 m along the surface ruptures mapped from optical results. These offset measurements are compared with field observations collected between the 31 October 2016 and the 16 July 2017 (90% were collected before the 22 December 2016), consisting of 7,323 records of coseismic surface rupture data (Villani, Civico, et al., 2018; see Text S1 for more information about field data integration). Figures 3 and 4 show, respectively, the measurements of throw and heave at the surface. For each heave measurement from optical results, the strike-perpendicular direction considered is relative to the rupture local azimuth.

Three main normal fault systems are described hereafter. They are used as an input in the inversion detailed further in section 3, where their geometry is described in more details, but they are briefly introduced here for the sole purpose of helping to describe the measurements. Their trace at the surface is deduced from the mapping of surface ruptures from optical results. Each mapped surface rupture is assigned to a fault system, according to the rupture dip direction (derived from the throw measurements performed on the rupture, see Figure 3) and location. The major "Monte Vettore" fault (MVF) is a west dipping fault that reaches the surface over a length of ~12 km. It accounts for most of the seismic moment release (e.g., Cheloni et al., 2017; Scognamiglio et al., 2018). A second fault named "Monte delle Prata" fault (MPF), antithetic to the MVF, nearly intersects the MVF at the latitude of Monte Vettore, then moves westward, away from the MVF, when one goes north. The two antithetic fault systems of MVF and MPF together form an asymmetric graben-like structure at large scale (Figure 1b). A third smaller, synthetic fault, named "Middle Slope" fault (MSF), is located in the hanging wall of the MVF. The MSF intersects the MPF (see between km 12 and 13 in Figure 3a) and locally introduces further complexity in the surface deformation signal.

The locations of the measurements made from optical results are most probably different from that of the field measurements. Thus, isolated measurements cannot be compared rigorously. We compare instead the maximum values and the median values on selected areas, to get a first-order estimation of the degree of agreement between the two data sets. On the southern flank of both Monte Bicco and Monte Bove Sud, numerous measurements of coseismic displacement were reported in the field (see between km 0 and 2 along Section A in Figure 3b), with up to 23 cm of heave (the median is equal to 0 cm) and 80 cm of throw (the median is equal to 32 cm). However, in the deformation maps, only very few offsets can be detected, around km 0.5, with four heave measurements with a median of 25 cm and one throw measurement of 4 cm. Wedmore et al. (2019) detected coseismic surface deformation due to the Norcia earthquake, on a section of the Monte Bove fault that ruptured during the 26 October 2016 Visso earthquake. The measured displacements are <10 cm and are not detectable in our horizontal and vertical deformation maps, possibly because the signal stays under the detection threshold. Moreover, the correlation score in the horizontal deformation maps is low in the area considered in this study. This area is located ~900 m from the location of the measurements from the deformation maps reported in Section A and ~500 m outside of the buffer zone around the mapped surface ruptures, used in our study to select the field measurements from Villani, Civico, et al. (2018). Those field measurements were all collected after the 30 October Norcia event. Therefore, there is no certainty whether the ground displacements measured in the field inside our buffer zone could be related to the 30 October event. Instead, they could be related to the 26 October event, and those structures would not have been remobilized significantly during the subsequent events, as they do not appear in the deformation maps, despite field measurements of significant amplitude. Indeed, the study by Wedmore et al. (2019), along with an ALOS-2 interferogram between 5 February and 28 October 2016 (http://www.gsi.go.jp/cais/topic161108-index-e.html; Figure S5), clearly show that the 26 October 2016 event ruptured the surface in this area. Between km 2 and 3.6 (Section B in Figure 3b), no evidence of slip on a coseismic rupture is observed at the surface, neither in the field nor in our deformation maps. However, evident surface deformation caused by shallow landslides, already documented by Villani, Civico, et al. (2018), are detected. These deformations are ignored in the subsequent analysis. On the MPF, from km 3.6 to 10 (Section C in Figure 3b), slip evidence is reported in the field, which can only be partly observed in the deformation maps, where decorrelation due to temporal changes between the acquisitions and forested areas prohibit measurement in some areas. Heave reaches up to 64 cm (the median is

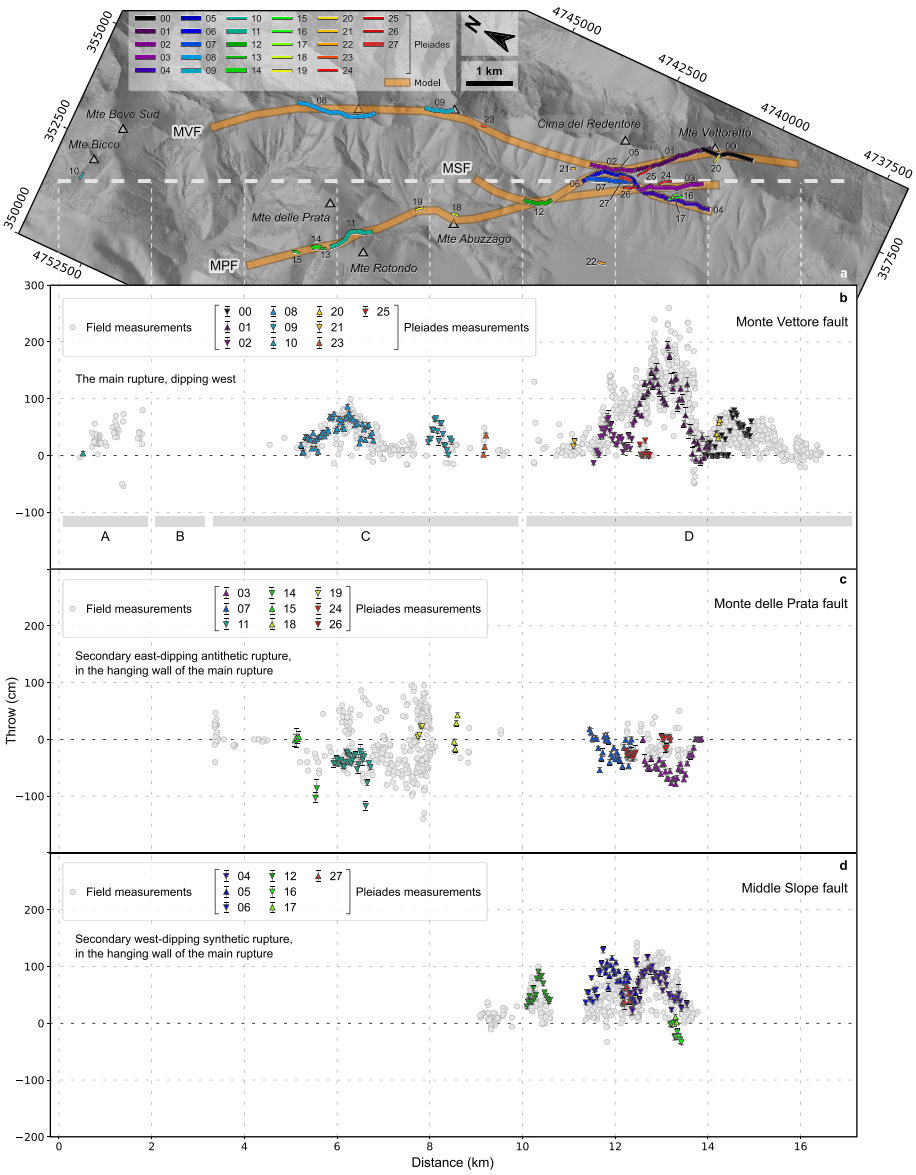

Figure 3. (a) Map of the coseismic ruptures, from the deformation maps, DSMs and orthoimages computed from optical data, on which offset measurements are performed (thin traces). Ruptures that recorded at least 50 cm of throw locally are represented thicker than the other ruptures. The thick orange traces represent the three main fault systems—MVF, MPF, and MSF—used as an input in the inversion. They are shown here only to explain the distribution of the data in three families: each set of measurements from optical data—one set by rupture mapped—and each field measurement is assigned to one of the three main fault systems, according to its dip direction and location on the map. The shaded DSM is composed of the Pleiades preevent DSM, complemented by the AW3D30 DSM (©JAXA). (b–d) For each fault system, throw at the surface, measured from the Pleiades vertical deformation map (colored triangles) and collected in the field by Villani, Civico, et al. (2018; gray disks). Each measurement location is projected along a baseline of azimuth N155°E (dashed gray line in panel a), arbitrarily divided into Sections A–D (see panel b) to facilitate the description. For normal faults, a positive (respectively negative) throw implies a dip toward the west (respectively east).

equal to 13 cm) for field measurements and 60 cm (the median is equal to 29 cm) in the deformation maps. Throw reaches up to 140 cm (the median is equal to 40 cm) for field measurements and 118 cm (the median is equal to 36 cm) in the deformation maps. Along the MPF, for most of the measurements, the dip direction is antithetic to the dip direction of the MVF (Figure 3c). Also in Section C, facing the MPF, the MVF experienced noticeable synthetic slip. Field observations report up to 46 cm of heave (the median is equal to 8 cm), where the deformation maps show 50 cm (the median is equal to 27 cm). Throw reaches up to

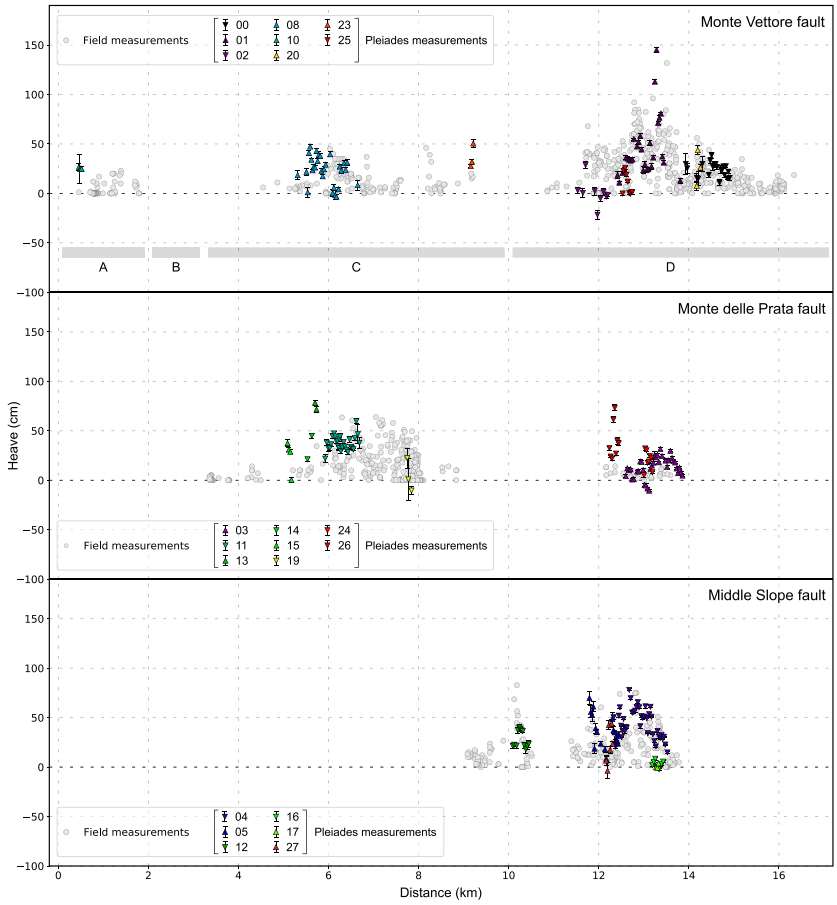

Figure 4. Heave at the surface, measured in the Pleiades horizontal deformation maps (colored triangles) and collected in the field by Villani, Civico, et al. (2018; gray disks). Each set of measurements from optical data—one set by rupture mapped—and each field measurement is assigned to one of the three main fault systems—MVF, MPF, and MSF—used as an input in the inversion (Figure 3a). Each measurement location is projected along a baseline of azimuth N155°E (Figure 3a). The strike-perpendicular direction in which heave is measured is relative to the rupture local azimuth. A positive (respectively negative) offset indicates extension (respectively compression).

100 cm for field data (the median is equal to 21 cm) and 86 cm (the median is equal to 40 cm) in the deformation maps. No measurements can be achieved in the horizontal deformation maps for Rupture #09, due to temporal decorrelation in this area. On the other hand, impact of temporal decorrelation is more limited in the vertical deformation map (see section 2.1), thus allowing us to successfully measure throw offsets on this rupture. Around km 10, the signal seems to weaken and almost disappear along the MVF and MPF faults, with very few coseismic slip observations in the field and no signal in the deformation maps. On the MSF, however, consistent series of measurements are made both in the deformation maps and in the field. From km 10 to 17 (Section D in Figure 3b), the rupture zone narrows to concentrate on the Monte Vettore western flank, as described before. Table 2 summarizes the measurements made. Figure S6 shows the throw measurements in a close-up view of the western slope of Monte Vettore. Between km 11 and 12.25, temporal decorrelation complicates or even prohibits measurements in the horizontal deformation maps. Hence, there is no horizontal measurement on the MSF for Rupture #06, on the MPF for Rupture #07 and on the MVF for Rupture #21. On Rupture #02 of the MVF, a few horizontal measurements are considered reliable enough to be kept.

The comparison between offset measurements made from our deformation maps and field observations shows that while the two data sets are consistent for many sites, they also diverge significantly at a few locations. Along the MVF, which hosts the largest coseismic slip, field measurements tend to be consistent or larger than measurements derived from deformation maps. Along the MPF and MSF, where deformation

Table 2
Heave and Throw at the Surface, Measured on the Deformation Maps Derived From Pleiades, in the Field and Deduced From the Model, Focused on the Western Flank of Monte Vettore (Section D of the Baseline Drawn in Figure 3)

		Heave (cm)		Throw (cm)	
Fault name	Data set	Maximum	Median	Maximum	Median
Monte Vettore	Field	132	18	260	47
	Pleiades	145	25	193	38
	Pleiades (sum)	145	21	193	53
	Model	100	76	70	53
Monte delle Prata	Field	14	6	50	20
	Pleiades	73	18	79	28
	Pleiades (sum)	70	0	83	37
	Model	16	1	42	3
Middle Slope	Field	83	18	142	45
	Pleiades	78	33	129	56
	Pleiades (sum)	94	44	184	91
	Model	16	12	90	70

Note. The measurements are distributed over the three main fault systems proposed for interpretation. Data sets named "Pleiades (sum)" are the maximum cumulative slip envelopes, computed to make the Pleiades measurements comparable with the inversion results, whenever the slip is distributed over multiple ruptures (Figure S16). For the line named "Pleiades," for a given offset measurement, the strike-perpendicular direction for heave is the same as the azimuth of the stacked profile at the measurement point (i.e., a "local" azimuth). Thus, the way heave is represented in the optical results is close to the way field measurements were collected, which is desirable for a comparison purpose. For the line named "Pleiades (sum)" on the other hand, because the objective is to compare the optical results with the inversion results, the azimuth considered is the azimuth of the closest patch from the model fault, the measurement point is assigned to.

is generally smaller, hidden in grassy mat and loose rocky soil, and cumulative scarps are more subdued, if they exist at all, offset measurements derived from deformation maps tend to be either consistent or larger than field measurements. In that configuration, field measurements might lead to underestimation of actual fault displacement.

Hence, in the context of a complex faulting geometry, where many of the ruptures are actually small and partly masked by vegetation and loose soils, deformation measurements through image correlation, provided there is no major temporal decorrelation, might constitute a critical data set to better constrain the 2016 Norcia rupture process by providing a homogeneous data set of surface-rupture measurements.

3. Joint Inversion of InSAR, GPS, and Optical Data

The 2016–2017 Italian earthquake sequence has been investigated in detail and an exceptional wealth of data has been accumulated. On one hand, several studies have focused on resolving various aspects of the kinematics and dynamics of the earthquake seismic source, using seismological and/or geodetic data (e.g., Cheloni et al., 2017; Chiaraluce et al., 2017; Huang et al., 2017; Pizzi et al., 2017; Scognamiglio et al., 2018; Walters et al., 2018; Xu et al., 2017). On the other hand, many groups have put their effort in common to document surface ruptures (Brozzetti et al., 2019; Civico et al., 2018; Perouse et al., 2018; Pucci et al., 2017; Smeraglia et al., 2017; Villani, Pucci, et al., 2018). Combining the two approaches, however, in order to produce an earthquake source model that would satisfy both low-resolution regional-scale data and high-resolution local-scale data, remains difficult. In the next part, as we have demonstrated in the previous sections that offset measurements derived from optical image correlation compare well with field data, we will combine our high-resolution local-scale data with lower-resolution regional-scale geodetic data to propose a set of models accommodating these different data sets.

3.1. Data

In order to estimate the distribution of coseismic slip at depth, we perform a static slip inversion of the 30 October 2016 earthquake, using a combination of surface deformation maps derived from radar and optical imagery, along with displacement vectors estimated from GPS measurements. The relatively large magnitude of the 30 October earthquake, combined with a shallow depth, is adequate to achieve precise measurements of the surface deformation field using InSAR. However, due to the occurrence of two M_w~6 shocks at short time interval (26 and 30 October), it is difficult to isolate the contribution of each single event in the InSAR signal. Furthermore, the deformation gradient close to the surface ruptures of the M_w6.5 30 October event leads to steep fringe patterns that cannot be easily unwrapped in X- and C-bands (e.g., Cheloni et al., 2017). Hence, we combine two ascending ALOS-2 L-band acquisitions from 28 October and 11 November 2016 to map the line-of-sight surface deformation field associated with the 30 October 2016 (Figure 5e and Table 1). The interferogram shows intense surface strain on the western flank of Monte Vettore, consistent with observations of surface ruptures there.

Unfortunately, no complementary descending interferogram allows for the separation of the M_w6.0 26 October and M_w6.5 30 October events. Therefore, we also incorporate the descending ALOS-2 interferogram (31 August to 9 November 2016) and apply a mask in the area of the M_w6.0 26 October event to ensure consistency with the rest of the data set. Finally, in order to compare with Pleiades 3-D displacement maps, we also include the quasi-east-west (E-W) and up-down (U-D) decomposition derived from two ascending and descending interferograms (e.g., Fujiwara et al., 2000) that captured both the 26 and 30 October events but not the 24 August event (24 August to 2 November 2016 and 31 August to 9 November 2016, respectively).

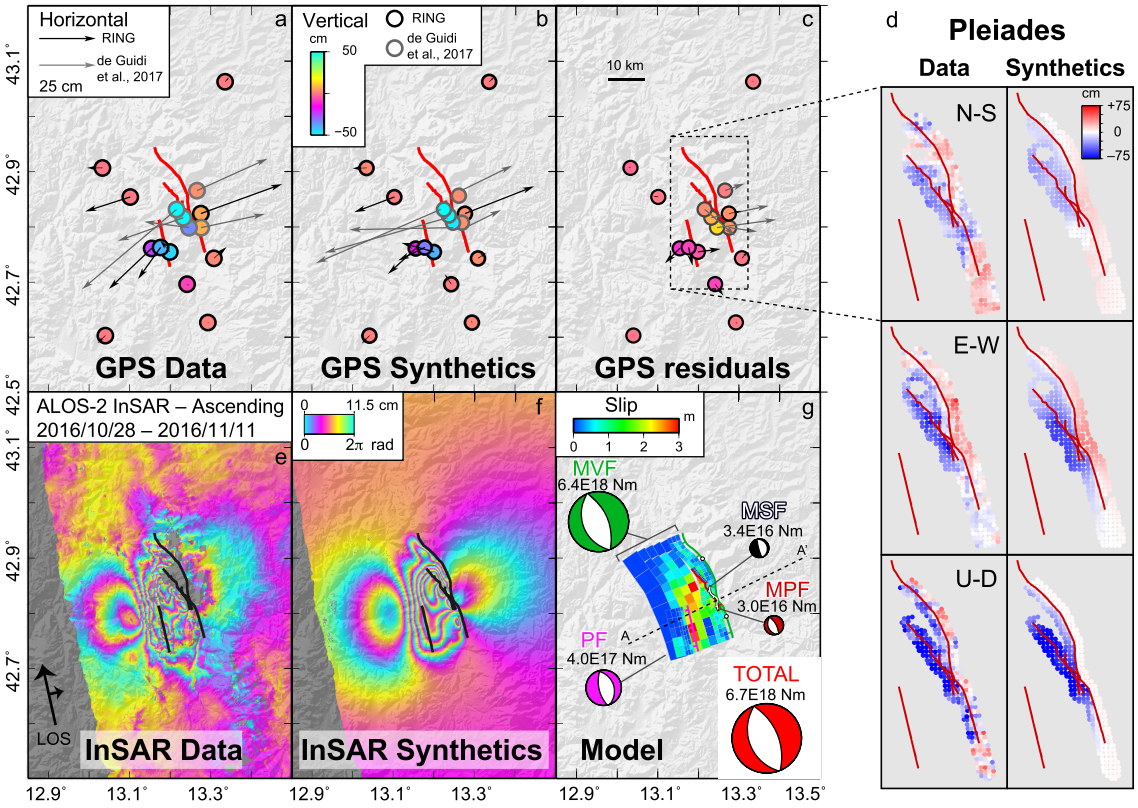

Figure 5. Comparison of (a) observed coseismic GPS displacements and (b) synthetic displacements predicted by the best model deduced from the joint inversion of GPS, InSAR, and optical correlation. (c) The residual displacements. Colored circles represent the vertical component of displacement, whereas vectors represent the horizontal components. The two GPS data sets are displayed in black (RING) and gray (De Guidi et al., 2017). Red lines are the surface trace of the modeled fault planes (MVF, MPF, and MSF) or the orthogonal projection of the upper edge of the fault plane when the fault does not reach the surface (PF). (d) The three-dimensional deformation obtained from optical correlation, downsampled to a resolution of 250 m for modeling purposes. (e) The observed line-of-sight deformation from ascending ALOS-2 InSAR and (f) the predicted deformation. (g) The slip distribution, in map view. Only slip on the main MVF and PF is represented here for clarity. Slip on the MPF and MSF is represented in Figures 6 and S10. Focal mechanisms and seismic moments (assuming a shear modulus of $G = 3 \times 10^{10}$ Pa) are indicated for each fault plane. Dashed line shows the location of the cross section in Figures 6d and S10.

The area affected by the 26 October earthquake is masked in the data sets that include the contribution of this event, based on prior knowledge of the extent of the area deformed by this event (Cheloni et al., 2017; Walters et al., 2018) to ensure consistency with the rest of the data set. This decomposition indicates that significant displacement (>10 cm) is recorded up to distances of 7–10 km from the MVF (Figure S7), except on the vertical component for pixels located on the footwall of the MVF, which everywhere show very little uplift (<10 cm). Relative displacement across the fault reaches slightly more than 100 cm horizontally and approximately 80 cm vertically. Comparison with horizontal and vertical displacements from Pleiades shows an excellent agreement between the two data sets in the distance range of 1 to 7 km away from the fault trace (Figure S7). Unfortunately, this comparison cannot be carried out near the fault trace due to decorrelation of InSAR.

GPS data covering the 30 October 2016 earthquake have been collected, processed, and harmonized by the Rete Integrata Nazionale GPS (RING) group and made available at ftp://gpsfree.gm.ingv.it/amatrice2016/static/Cosismico_30Oct2016_GPS_GdL_V1.dat (Avallone et al., 2010; Devoti, 2012). This data set consists of a few continuous GPS stations, complemented by campaign GPS measurements at benchmarks that had been already installed and surveyed prior to the 2016 sequence. The benchmarks were reoccupied after the 24 August 2016 earthquake and recorded the 26 and 30 October 2016 shocks. The contribution of the 30 October earthquake was isolated from continuous GPS measurements using daily solutions. This data set covers both the footwall and the hanging wall of the main fault (Figure 5). A clear E-W extension is visible across the fault, whereas contraction is observed away from the fault. Sites located on the hanging wall

exhibit a clear subsidence reaching −45 cm, whereas sites on the footwall, in spite of a very close distance from the fault trace (~2 km for site VETT), show small uplift, consistent with ALOS-2 and Pleiades results (Figure S7).

We also include the data set published by De Guidi et al. (2017), which consists of five additional campaign sites located within 1 to 4 km away from the trace of the MVF. These benchmarks were first surveyed in early October 2016 and then resurveyed in November 2016, so that this data set includes the contribution of both the 26 and 30 October 2016 earthquakes. Nevertheless, the location of the De Guidi et al. (2017) network is mainly centered on the area where the most prominent surface ruptures of the M_w6.5 30 October 2016 were observed, whereas the M_w5.9 26 October 2016 event appears to be located further to the north (Figure S5). Therefore, in first approximation, we may consider that this data set mainly captures coseismic deformation due to the 30 October earthquake. Similar to the RING data set, horizontal extension is recorded close to the fault, with a maximum of 86 cm relative horizontal displacement between sites VTW1 and VTW5. Up to −77 cm of subsidence are measured on the hanging wall, whereas less than 10 cm of uplift are measured on the footwall. In spite of its potential limitations (contribution of the 26 October earthquake and potential post-seismic signal), thanks to its exceptionally close location with respect to the surface ruptures, the GPS data from De Guidi et al. (2017) allow for validating the deformation field derived by ALOS-2 and Pleiades in the very near field (Figure S7).

Overall, the ALOS-2 data set allows for accurately measuring displacement in the midfield and far field of the earthquake (i.e., >1 km from the fault), thereby illuminating the slip distribution at depth, whereas the Pleiades data set covers the midfield and near field (i.e., <5 km from the fault), providing information about slip at shallow depth and at the surface. On the other hand, GPS data bring a strong reference frame to the data set, effectively constraining the maximum extension of slip at depth, as well as the main features of the seismic moment tensor of the earthquake.

3.2. Methods

The inversion is carried out using the Classic Slip Inversion package (Jolivet et al., personal communication) using a standard approach whereby surface displacement is modeled by superimposing elementary displacement field due to rectangular dislocations embedded in a linear elastic homogeneous isotropic half-space, using Okada's (1985) equations. We first decimate the ALOS-2 and Pleiades deformation maps using a quadtree algorithm (e.g., Grandin et al., 2009) (Figure S8). ALOS-2 InSAR data are resampled to a homogeneous 1-km posting in the area within 15 km of the epicenter and to 8-km posting beyond. ALOS-2 quasi-E-W and U-D decompositions are resampled to 2-km posting close to the fault and 8 km further away. Both data sets are masked within 1 km of the surface trace of the MVF, MSF and MPF, in order to avoid incorporating unwrapping errors. Pleiades data (E-W, N-S, and U-D) are downsampled to 0.5-km posting, keeping only measurements made within 1 km of the trace of the coseismic surface rupture, in order to fill the measurement gap in the ALOS-2 data set. The total number of data points after decimation is 1,327 points for the ALOS-2 interferograms, 316 points for the ALOS-2 quasi-E-W and U-D decompositions, and 1,055 points for the Pleiades data. ALOS-2 quasi-E-W and U-D decompositions, which may be subject to larger uncertainties due to assumptions in the decomposition (e.g., N-S displacement is assumed to be negligible), are therefore underweighted in the overall data set in order to avoid a propagation of errors in the inversion. For both ALOS-2 and Pleiades data, we estimate a variance-covariance matrix by computing the empirical semivariogram fitted with an exponential model, excluding the area of significant deformation (e.g., Lohman & Simons, 2005).

In the inversion, fault geometry is fixed, and has to be determined beforehand. We find that at least four faults (Figures 5 and 6) are necessary to explain the observations:

1. The main west dipping MVF, which concentrates most of the slip. The "Monte Vettore" normal fault is ~20 km long with a mean strike of N150°E. Its ruptured part at the surface is ~12 km long. On the Monte Vettore western flank, this fault is characterized by (1) a conspicuous topographic slope break, (2) a nearly vertical free face, locally designated as "Cordone del Vettore," and (3) an unconformity between Corniola (Jurassic) limestone uphill and slope deposits downhill (Pierantoni et al., 2013). To better fit the mapped rupture at the surface while keeping a simple geometry at depth, the fault is divided into two subfaults: (1) a shallow part from 0.05- to 2.5-km depth—the fault does not reach surface in the

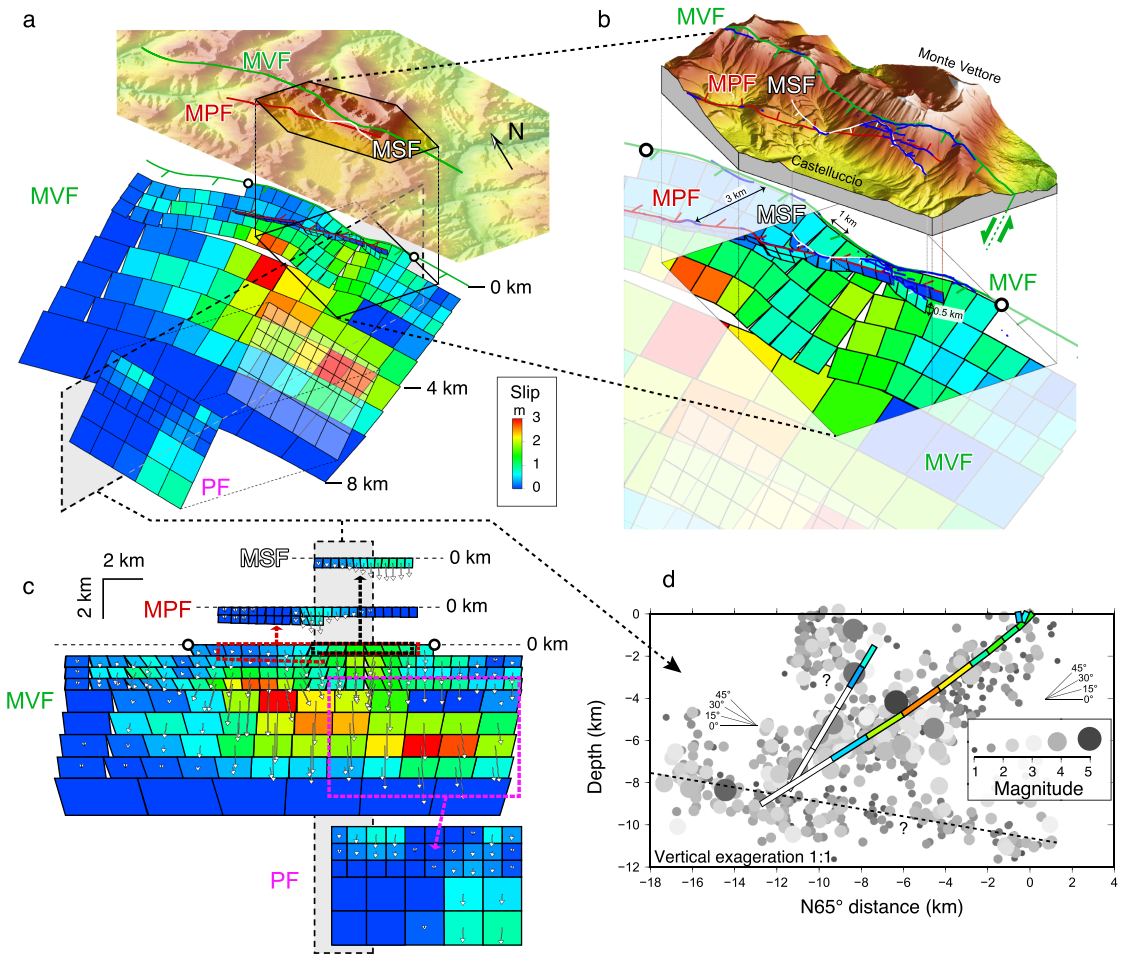

Figure 6. (a) Slip distribution from the joint inversion of the InSAR, GPS and optical data. (b) Close-up view of the Monte Vettore area. Surface ruptures mapped from the Pleiades results (blue lines) are draped on a three-dimensional view of the Pleiades postearthquake DSM. The simplified mapping used to define the surface trace of the modeled faults is shown with barbed colored lines (the ticks point to the downdip direction). (c) Slip distribution on the four fault systems defined for the inversion. Dashed colored lines on the MVF represent the projected locations of the PF, MSF, and MPF. Estimated uncertainties in the slip distribution, estimated following the approach of Tarantola (2005), are shown in Figure S20. As shown in the 3-D perspective view, patches on the MVF do not connect exactly due to double curvature of the fault plane, which cannot be exactly mapped with rectangular elements. However, we checked that this minor approximation does not have any consequence at the surface. (d) Cross section perpendicular to the system showing the relative location of the modeled faults (shown as colored bars, with color representing the modeled coseismic slip) and relocated seismicity reported by Chiaraluce et al. (2017) for the period between 1 October and 29 November 2016 (keeping only earthquakes with magnitudes greater than 1). Cross-section location is indicated in Figures 5f (Profile A-A′), 6a, and 6c.

model to avoid unrealistic elastic overshoot within ~100 m of the fault trace—dipping toward the west at 40°, divided in 1 by 1-km patches and that follows the wavy trace of the rupture, and (2) a deep part from 2.5- to 8-km depth, with a simpler along-strike curvature, dipping toward the west at 35°, divided in 2 by 2-km patches in its upper part and in 4 by 4-km patches along its bottommost row. The dip angle of our fault is consistent with the dip of ~38° toward the SW calculated by averaging moment tensor solutions of the 30 October earthquake from a collection of publicly available sources (Figure S9). In cross section, this fault follows the west dipping plane highlighted by the aftershock distribution and terminates near its intersection with the east dipping decollement level inferred at 8–10 km (Chiaraluce et al., 2017) (Figures 6d and S10). We find that a dip angle steeper than 35–40° fails to explain the horizontal:vertical displacement ratio on the hanging wall, while producing excessive uplift on the footwall. For a better stability of the inversion, slip at the surface is prevented in areas where no surface ruptures were detected in the field or in the Pleiades data. This constraint is implemented by removing the uppermost row of patches beyond the along-strike interval where surface ruptures are present (black filled circles in Figures 5g and 6).

2. A conjugate east dipping fault, named MPF, corresponds to a secondary fault that produced discontinuous surface rupture to the west of the main surface rupture. Field observations and imagery concur to a dip toward the east for this fault. This conjugate fault, of mean strike N60°W, outcrops at a distance as short as 500 m away from the main fault in its southern part, and progressively gets further toward the north, up to 2 km at its termination. Horizontal:vertical ratio along the rupture suggests a variable dip along strike, from steep to the south to shallow to the north. Due to its proximity to the main fault, the MPF is extended from the surface down to 0.5 km with a dip of 85° in its southern part, and down to 1 km with a dip of 40° in its northern part. The fault is divided into 0.5 by 0.5-km patches.
3. A west dipping fault, hereafter called MSF, located in the hanging wall of the MVF, is inferred from detailed analysis of surface ruptures and deformation visible in Pleiades data on the western flank of Monte Vettore (Figures 1 and 2). This fault has a complex, discontinuous trace, and even intersects the east dipping MPF, producing a horst-and-graben feature depending on whether the two faults are dipping away from or toward each other. In spite of an apparently steep dip near the surface, the vertical component of displacement across the fault seems to decay sharply at very short range (<200 m if we look at the portion of the rupture between N42.82° and N42.83°; see Figure 2), whereas the horizontal component of relative displacement across the fault dominates further away. As discussed later in section 4, this fault is interpreted as a very shallow structure (<500 m in extent at depth) that cannot be fully accounted for by the present joint inversion. Nevertheless, in order to simulate the offset visible in the Pleiades imagery along the trace of the MSF, the fault is described by a single row of 0.5 by 0.5-km patches. The fault is given a steep dip (80°) in consistency with direct measurements made in the field (section 2.3). However, after testing several geometries for the MSF, we notice that slip distribution on the MSF recovered by the inversion is not very sensitive to the dip angle. This suggests that details of the deformation in the vicinity of this fault are not fully restituted by our downsampling procedure. This specific point will be further discussed in section 4.
4. Finally, the "Patino" fault (PF), dipping toward the west, is necessary to explain the fringe pattern visible in ALOS-2 data between the Castelluccio and Norcia plains (Figures 5e and S5b). Previous studies have disagreed on the actual dip direction of the fault. In their static inversion, Walters et al. (2018) choose an east dipping fault, as suggested by an alignment of aftershocks, and include an additional N220° trending fault bounding the southern part of the Castelluccio basin (also named "Piano Grande"). Scognamiglio et al. (2018) include a N210° trending fault in their kinematic inversion. Cheloni et al. (2017) showed that available geodetic data do not allow to constrain the detailed geometry of this blind fault. In particular, a conjugate plane dipping toward the east would achieve a similar success in explaining InSAR and GPS observations. We here choose to fix the dip of the PF to 60° toward the west (i.e., synthetic to the MVF), so that the along-dip projection of the fault plane at the surface corresponds to the diffuse ruptures mapped along the western side of the Castelluccio plain (Villani, Civico, et al., 2018). This fault geometry is broadly consistent with a secondary concentration of seismicity in the hanging wall of the main MVF (Figures 6d and S10). We set the lower edge of this fault to 8 km, that is, near the intersection with the MVF. The fault is divided into 0.5- by 0.5-km patches in its upper part, and 1- by 1-km patches near the bottom.

This geometry is simplified compared to the mapping of surface ruptures (i.e., discontinuous ruptures are considered continuous; rupture traces are smoothened; some minor ruptures are ignored). The continuity of a fault in the model does not imply that the faults are continuous in reality: the aim of the chosen geometry is to intersect all surface ruptures mapped at the surface, while retaining a reasonable complexity of the model. Nevertheless, its coarser resolution is consistent with the size of the defined patches.

The inverse problem is solved by means of a nonnegative least squares algorithm (Lawson & Hanson, 1995). For all fault planes, both dip slip and strike slip are inverted. However, in order to avoid unrealistic rake values, the slip direction in map view is forced to remain within ±15° from a mean azimuth of N70°E for all faults. Due to the variable strike angle along the fault trace, the rake angle is adjusted accordingly, so as to satisfy the prescribed range of azimuth for the horizontal component of slip. We checked that allowing for a broader range of possible slip directions (e.g., ±45°) only marginally impacts the final, estimated slip distribution. Slip roughness is controlled by a model covariance matrix filled with an exponential function and scaled by a metaparameter that allows for tuning the smoothness of the slip distribution (e.g., Radiguet et al., 2011). Smoothing only applies to patches belonging to the same fault. The value of the

metaparameter is fixed by an L-curve criterion (Figure S11). In addition to slip, a 2-D ramp is adjusted on each data set to account for unmodeled large-scale signal (e.g., orbital errors or atmospheric artifacts for the InSAR data set, inaccuracies in the compensation of the platform attitude for the Pleiades data set).

3.3. Inversion Results

3.3.1. Slip Distribution at Depth

One of our concerns is to obtain a model that can reconcile at best data of different resolutions, at both far-field and near-field scales, and especially the high-resolution measurements made from Pleiades close to the ruptures. Figure 5 shows the slip distribution obtained after running the inversion procedure, as well as the fit to the ALOS-2 InSAR, Pleiades and GPS data (Figure S8 shows misfits to all imagery data sets). The best model yields a good fit to ALOS-2 and GPS data (>85% variance reduction). Residual GPS displacements are generally less than 5 cm, except for GPS measurements located close to the trace of the MVF where a systematic ~15-cm residual eastward motion is observed on both sides of the fault (Figure 5c). Residuals to the Pleiades data set also yield similar values, with a standard deviation of 14 and 19 cm for the E-W and N-S components, respectively (Figure S8). The standard deviation of residuals for the Pleiades vertical component is higher (24 cm), which is consistent with the higher level of noise visible in cross sections (e.g., Figure 2).

Residual displacements at close distance from the fault are likely due to the relatively low degree of detail of the model resulting from the combination of data downsampling, finite patch size (0.5 km), and smooth slip. On the other hand, surface displacement modeled with the synthetic slip distribution achieves a reasonable fit to the InSAR and GPS data at distances >1.0 km from the trace of the MVF, as shown in Figure S7. We, however, note that the misfit on the ascending ALOS-2 InSAR data (standard deviation of 4 cm) is better than on the descending ALOS-2 InSAR data (standard deviation of 6 cm), which contains maximum residual misfits reaching up to 15 cm. This difference likely stems from the fact that the ascending geometry has a line-of-sight vector nearly perpendicular to the MVF fault plane, hence is less sensitive to coseismic deformation. For both line-of-sight directions, the InSAR misfits are concentrated on intermediate-wavelength features of the deformation field (~15 km), in particular around the south and west sides of the Piano Grande/Castelluccio basin. Residual misfits likely reveal second-order discrepancies between the idealized setup chosen in our inversion and the actual fault geometry at depth. These shortcomings suggest that the geometry of secondary faults not reaching the surface in the hanging wall of the main MVF, especially those located between the Castelluccio and Norcia basins, such as the PF, is poorly constrained. In fact, these secondary structures are modeled with a broad range of configurations in previous studies relying on InSAR and/or GPS data (see Cheloni et al., 2017; Scognamiglio et al., 2018; Walters et al., 2018), which reflects a persistent ambiguity in the determination of the geometry and kinematics of these blind faults. Nevertheless, residuals on the InSAR data are mostly restricted to >2 km from the main west dipping MVF fault trace, hence do not massively affect our conclusions on the fault geometry and distribution of slip at shallow depth on the main MVF. We conclude that, although the model does not capture the full complexity of the rupture at depth, the fault geometry and slip distribution are appropriately described at first order.

In our preferred model, most of the seismic moment is released on the MVF (6.4×10^{18} Nm), with slip reaching a maximum of 3 m at depth (Figures 6d and S10). Small amounts of slip (<1 m) are also recovered on the PF, MSF and MPF, where the seismic moment released accounts for ~6%, ~0.5%, and ~0.5%, respectively, of the moment released on the MVF. The total scalar seismic moment is 6.7×10^{18} Nm, equivalent to a moment magnitude of M_w6.5.

Slip on the MVF is mainly concentrated in the depth range between 2 and 6 km under the free surface of the model. Slip on the MVF reaches up to 3 m and decreases toward the surface to ~1.5 m, as illustrated in Figures 6 and S10. This result is consistent with other analyses available in the literature (e.g., Cheloni et al., 2017; Walters et al., 2018).

This behavior is constrained by the observation of a "concavity" in the vertical deformation field, with the maximum subsidence of the surface of the hanging wall occurring ~3 km away from the surface trace of the MVF (Figure S7b). Such a feature would not be observed if slip were distributed uniformly on the fault plane from a depth of ~10 km up to the surface, as demonstrated by forward tests conducted using simplified slip distributions (Figure S12). We checked that a uniform-slip distribution would result in a varying subsidence of the hanging wall, which would monotonously increase from the far field toward the surface trace of

the fault, reaching a maximum at the fault trace that is inconsistent with observations. On the other hand, the "concavity" observed in the vertical component of deformation ~3 km away from the fault trace can be reproduced if slip decreases from the bottom of the fault toward the surface.

This decrease of slip toward the surface is also consistent with ALOS-2 observations (Figure 5e), which shows a maximum line-of-sight change (corresponding to motion away from the satellite) occurring west of the surface trace of the modeled PF. Although ALOS-2 InSAR measurement also includes the influence of the E-W deformation, forward reprojection of the modeled deformation field indicates that this contribution cannot explain this "concavity," which instead mainly originates from the vertical component (Figure S12).

We note that a similar "concavity" in the hanging wall, occurring 1–2 km from the fault trace, was also observed in the case of the 24 August 2016 *M*6.0 Amatrice earthquake using ascending and descending InSAR data. It has been the subject of a specific analysis by Tung and Masterlark (2018), who used finite-element modeling to test whether this "concavity" could be explained by (1) a decrease of coseismic slip toward the surface, (2) variations of elastic properties of rock as a function of depth, or (3) a curvature of the fault plane. The authors concluded that accounting for realistic properties of rock and variable dip at depth cannot explain this feature, which, in turn, reveals the existence of a tapering of slip toward the free surface, akin to the shallow slip deficit effect documented for several instances of continental strike-slip ruptures (e.g., Fialko et al., 2005; Xu et al., 2016). This tapering effect is commonly observed for most shallow normal-faulting earthquakes, as for the 1997 M6.0 Colfiorito earthquake (Lundgren & Stramondo, 2002), the 2009 M6.1 L'Aquila earthquake (Walters et al., 2009), the 2006 M7.0 Mozambique earthquake (Copley et al., 2012; Raucoules et al., 2010) or the sequence of five earthquakes with magnitudes ranging from *M*5.9 to *M*7.1 that occurred in 2008 on the Tibetan plateau (Elliott et al., 2010).

We conclude that the imagery and GPS data for the 30 October 2016 earthquake are consistent with coseismic slip reaching a maximum of 3 m near ~4-km depth and decreasing to only ~1.5 m at the surface (Figures 6d and S10). We also suggest that this shallow slip deficit effect is common to many normal-faulting earthquakes with magnitudes $M < 7.1$, as revealed by high-quality InSAR data.

3.3.2. Comparison of the Model Prediction With Surface Offsets From Pleiades and From Field Measurements

Figure S13 compares the Pleiades heave measurements at the surface with the slip provided by the model at the surface, each Pleiades measurement being projected according to the azimuth of the corresponding model patch. In the same way, the lateral slip (i.e., strike slip) at the surface is shown in Figure S14 and the throw at the surface is represented in Figure S15. As mentioned previously, for a better stability of the model, the modeled MVF only reaches the surface between distance along the baseline from km 3.6 and km 16. Considering the coarser resolution of the slip patches and the constraint to generate a model consistent at multiple scales, slip observed in the deformation maps from Pleiades and in field data is successfully reproduced at first order (Figure S7).

In Section C (initially defined in Figure 3b), on the MVF, heave deduced from the model and observed in the Pleiades data and in the field (the median values are equal to 20, 27, and 8 cm, respectively; the maximum values are equal to 51, 50, and 46 cm, respectively) are in relatively good agreement (see Figures 4 and S13). The median of the throw measurements from Pleiades, with 40 cm, is about twice the ones deduced from the model (14 cm) and observed in the field (21 cm) (see Figures 3 and S15). The maximum throw values measured in Pleiades and in the field (86 and 100 cm, respectively) are in good agreement, while, in the model, throw culminates at 36 cm only, in this section. On the "Monte delle Prata" antithetic fault, heave deduced from the model, with a median equal to 4 cm, is in relatively good agreement with the field data (13 cm) whereas the Pleiades data show 29 cm. The maximum heave values measured in Pleiades and in the field (60 and 64 cm, respectively) are very similar, while the model reaches 28 cm at most. A slip deficit is observed in the model for throw—the median is equal to 6 cm for 36 and 40 cm for the Pleiades and field data, respectively. Around km 10, the model shows no slip waning on the MVF.

For Section D, to make the Pleiades measurements comparable with the model, cumulative slip along the baseline shown in Figure 3a is computed (Figures S13–S15). Again, the measurements are divided into three geographical zones corresponding to the MVF, MSF, and MPF. For each zone, measurements made on the deformation maps are added up whenever they are distributed on multiple ruptures (see Figure S16 for a

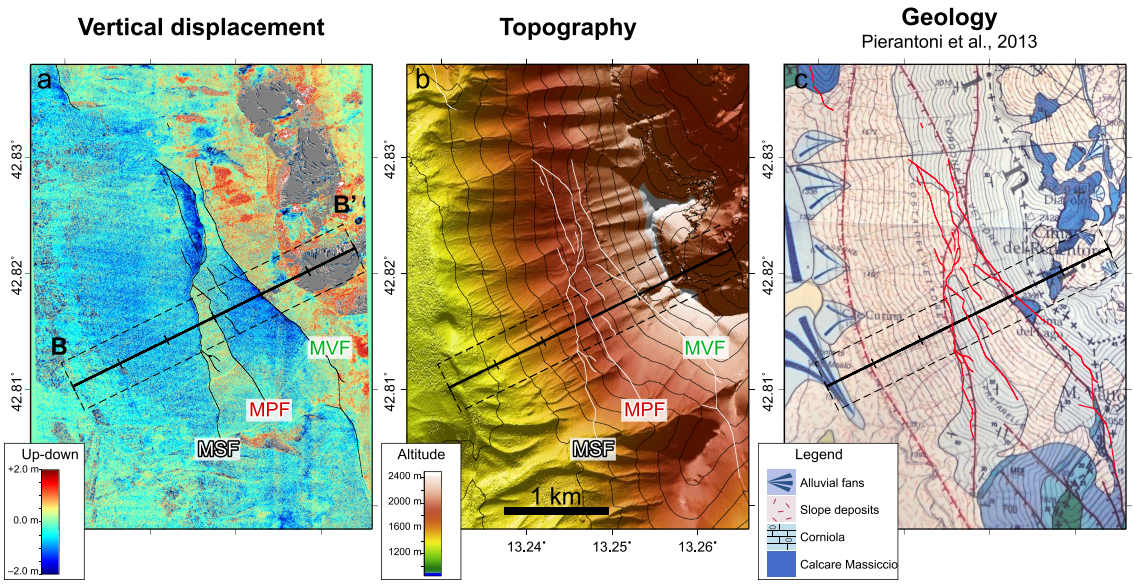

Figure 7. Relationship between coseismic deformation, topography, and surface geology in the area of the surface ruptures of the 30 October 2016 Norcia earthquake (see location in Figure 1b). (a) Vertical component of surface displacement from Pleiades. (b) Postearthquake digital surface model contoured every 100 m. (c) Geological map from Pierantoni et al. (2013). Note that outcrops of Corniola formation (limestone) are mapped along the horst structure between the MSF and MPF. The horst is flanked by slope deposits, suggesting that repeating relative uplift occurred on this structure in the past.

description of the method used). The results appear in Figure S13 for the heave, Figure S14 for the lateral slip, and Figure S15 for the throw. Maximum and median amplitudes are reported in Table 2. For the "Monte Vettore" west dipping fault, the median of the heave deduced from the model, with 76 cm, is 3.6 times the cumulative heave from Pleiades. The Pleiades and field measurements (21 and 18 cm, respectively) are in good agreement. The medians of the throw measurements are similar between the model (53 cm), Pleiades (53 cm), and the field (47 cm). On the "Monte delle Prata" antithetic fault, the three data sets show little slip in the horizontal, strike-perpendicular direction. In the vertical direction, the model shows very little slip, whereas slip observed in Pleiades has a median of 37 cm. Concerning the "Middle Slope" synthetic fault, heave deduced from the model, with a median of 12 cm, is less than 30% of the Pleiades cumulative heave (44 cm). The median of the throw measurements from Pleiades (91 cm) is in relatively good agreement with the one deduced from the model (70 cm).

4. Significance of Deformation at Close Distance From the Surface Ruptures

The Mts. Sibbilini area is affected by a complex network of surface ruptures associated with the 2016 Norcia earthquake, which locally recorded a large amount of slip at the surface (maximum ~2 m). The slip inversion described in the previous section does not aim at reproducing this small-scale variability. As discussed in section 3, throw at the surface however appears to vary smoothly along strike at the kilometric scale (Figure S15). This feature is correctly captured by the inversion, which suggests that broad-scale along-strike variations of slip at depth are well resolved by the inversion.

On the other hand, significant off-fault deformation is also observed across strike, within a few hundred meters of fault ground ruptures. Figure 2c shows that up to 40 cm of horizontal shortening occurs 200 m to the west of the MSF, that is, in the hanging wall of the main west dipping MVF (blue dashed line in Figure 2c). Similarly, Figure 2b (see also Figure 7) shows that the subsidence of the hanging wall increases dramatically near the surface rupture of the MVF, reaching 80 cm over a distance of 500 m.

This off-fault deformation, visible at short distance from surface ruptures, has important implications: If interpreted within the framework of linear elasticity, this small-scale deformation points to a complexity of the fault geometry and/or to a variability of coseismic slip at shallow depth (<500 m). This is in keeping with the dip of the faults measured at the surface (50–80°) and the short distance between the subparallel fault traces of the main faults (100–500 m): Based on these values, a downward prolongation of the fault

planes leads to an intersection of the fault strands at depths no greater than 500 m (see e.g., the cross sections of Figure 4 in Brozzetti et al., 2019). Therefore, it is tempting to interpret these off-fault deformation signals as resulting from geometric complexities associated with fault connection in the shallow subsurface. These complexities cannot be accounted for by the large-scale slip inversion developed in section 3 and they require a specific modeling strategy.

In the following, we concentrate on a 3-km-long profile crossing the western slope of Monte Vettore. This profile is located where surface ruptures are best documented and where the Pleiades data set shows the clearest off-fault deformation signal (Figure 7). In addition, unlike farther north, the profile intersects the fault strands in an area where individual faults are separated by a distance large enough (several hundred meters) to make the off-fault deformation interpretation easier. This cross section roughly corresponds to the Cross Section D-D′ in Figure 4 of Brozzetti et al. (2019). Slip on the MSF and MPF leads to the formation of a ~150-m-wide horst within the hanging wall of the main MVF, which intersects the surface 500 m to the east. The outcropping of the Corniola formation between the MSF and the MPF (Figure 7c) is exempt from the scree covering the slope elsewhere. This observation and the fact that this horst-like feature is already visible in the preearthquake DSM (Figure S17) both indicate that similar deformation patterns already happened in the past. Thus, the rupture complexity across the western slope of Monte Vettore mostly reflects long-lasting fault complexity at shallow depth.

In order to decipher these small-scale deformation signals, we adopt a forward modeling strategy, with the aim of determining the best fault geometry and slip distribution at shallow depth that would reproduce our observations. Obviously, this approach is subject to nonuniqueness and should be interpreted with caution. Individual models are not necessarily representative of the full range of models providing a good fit to the data but rather reflect particular model configurations that satisfy the observations, hence indicating possible scenarios.

We test a range of scenarios using Okada's equations, assuming that deformation occurs in 2-D within a vertical plane (i.e., no motion occurs horizontally along strike, which is equivalent to an assumption of plane strain). At the surface, we include three dislocations representing, from east to west, the MVF, MPF, and MSF, respectively. To facilitate the parameters space exploration, we fix the intersection of these three faults with the surface based on the locations of the steps measured in the displacement profile (Figure 8). For each step, we measure the horizontal and vertical relative displacement across the fault and we compute the corresponding dip angle and slip magnitude, making the assumption that relative displacement is due to pure dip slip. These geometric parameters are listed in Table S4. Since the MVF and MPF form a ~500-m-wide graben, they can be inferred to intersect at shallow depth (<1 km). Assuming that the two faults connect at depth into a third fault extending downward, the dip angle and slip magnitude on this third fault can be calculated based on the assumption that slip vectors form a closed triangle, akin to kinematic reconstructions on triple junctions (Caskey, 1995). This assumption allows for interpreting residual deformation in terms of departure from a rigid behavior. Taking into account the dip of these two faults (69° and 67°, respectively), as well as the magnitude of the two slip vectors (121 and 48 cm, respectively), we find a dip of 47° and a slip magnitude of 93 cm for the third fault, hereafter named "Dislocation D" (see inset in Figure 8, Scenario 1). This dislocation is then assumed to connect to a deeper dislocation that accounts for the large-scale deformation induced by slip on the deeper parts of the MVF. This deep dislocation, hereafter named "Dislocation E," is modeled as a 35° dipping fault, with a dip slip of 1.5 m and an along-dip width of 5 km. These values are taken from the average features of the slip model derived from the inversion in coincidence of the fault section profile. We checked that short-spatial-wavelength deformation patterns along the profile are largely insensitive to the parameters of this dislocation. By trial and error, we fix the along-dip width of the Dislocation D (connecting updip with Monte Vettore and Monte delle Prata dislocations and downdip with Dislocation E) to 0.5 km. On the other hand, the MSF, with a dip of 53° toward the west according to surface measurements from our Pleiades deformation maps, is difficult to root into any clearly identified deeper structure based on our observations only. Finally, for the Middle Slope dislocation, we are left to explore only one parameter, namely, its along-dip width.

As our objective is to accurately model surface deformation within a zone of $\pm$1 km around the surface ruptures, it is necessary to take into account the local topography in the calculations (e.g., Tinti & Armigliato, 2002). Indeed, the western flank of Monte Vettore is characterized by a pronounced slope toward the west,

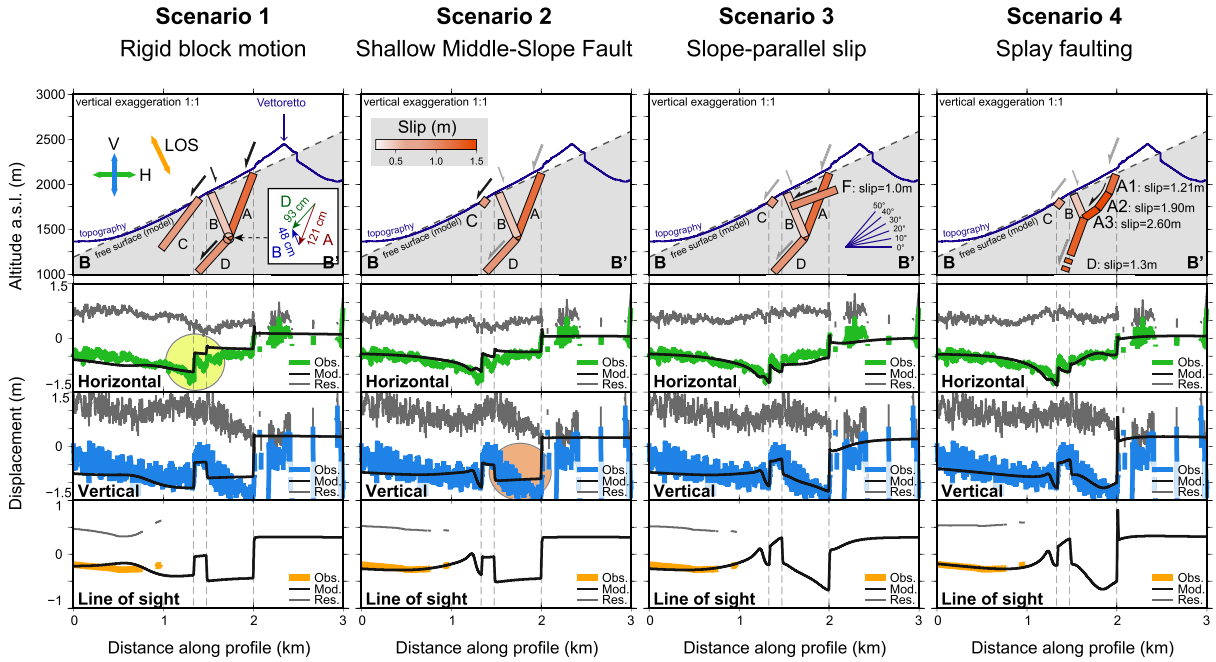

Figure 8. Near-fault simulations of surface displacement using four scenarios of fault geometry and slip at depth. The location of Profile B-B′ is shown in Figure 7. The upper row depicts the geometry of faults in relation with local topography. The bottom rows show observed (colored), modeled (black), and residual (gray) surface displacements. In the simulations, the free surface is assumed to dip at 25° toward the west, and the predicted displacement is rotated to retrieve the E-W and updown components (Figure S18). Note that the line-of-sight component is nearly orthogonal to the surface. Scenario 1: geometry and slip on faults mapped at the surface is extrapolated downdip. MVF (A) and MPF (B) intersect and merge into a third dislocation (D) whose dip angle and slip is determined by assuming kinematic compatibility between Dislocations A, B, and D (see inset in the top left panel, with the values from Table S4). MSF (C) is ascribed a downdip width of 0.7 km. Scenario 2: same as Scenario 1 but with a shorter MSF. Residuals on the horizontal components (yellow ellipse) are reduced. Scenario 3: same as Scenario 2, but with an additional dislocation dipping parallel to the surface topography. Residuals on the vertical component (red ellipse) are reduced. Scenario 4: alternative scenario where residual downslope displacement in the hanging wall of the MVF is explained by a progressive flattening of the MVF downdip, associated with a doubling of slip magnitude down to ~300–500 m under the surface.

reaching 25° on average and up to 45° toward the summit. Due to this steep topography, the faults cut the free surface at different altitudes, and they intersect each other at a significantly different depth and location compared to a situation where the surface would be assumed as horizontal. This eventually affects the pattern of deformation at surface and violates the boundary conditions of a horizontal free surface in Okada's equations. Although a more advanced modeling strategy would be required to accurately account for topography, it is possible to account in first approximation for the effect of a uniformly sloping free surface by rotating Okada's equations. In practice, we rotate all fault dips 25° clockwise so that the relative angle between the free surface and the fault plane is simulated, instead of the dip angle, which represents the angle with respect to a horizontal reference surface (Figure S18a). In the simulation, east dipping faults (respectively west dipping faults) are therefore modeled with a steeper (respectively shallower) dip angle relative to the model free surface. In a final step, after the forward simulation has been computed, we rotate the coordinate system back by 25° clockwise in order to convert surface-parallel and surface-perpendicular displacements into horizontal and vertical displacements (Figure S18b).

Finally, we present two extreme scenarios for the downdip width of the MSF (Figure 8). The first scenario (1) assumes a width of 0.7 km. In this scenario, the first-order long-spatial-wavelength features of the deformation field appear to be correctly reproduced, as well as the “steps” induced by the three faults intersecting the surface. This similarity is explained by the fact that the model takes into account the slip vectors of the three faults that can be directly measured from the 3-D Pleiades measurements. Due to the slip vector triangle closure assumption, the modeled deformation field is, in first approximation, consistent with rigid block motion, except in the vicinity of the surface projection of the downdip edge of the MSF. As a result, residual deformation (i.e., observed minus modeled) highlight departures from the rigid behavior.

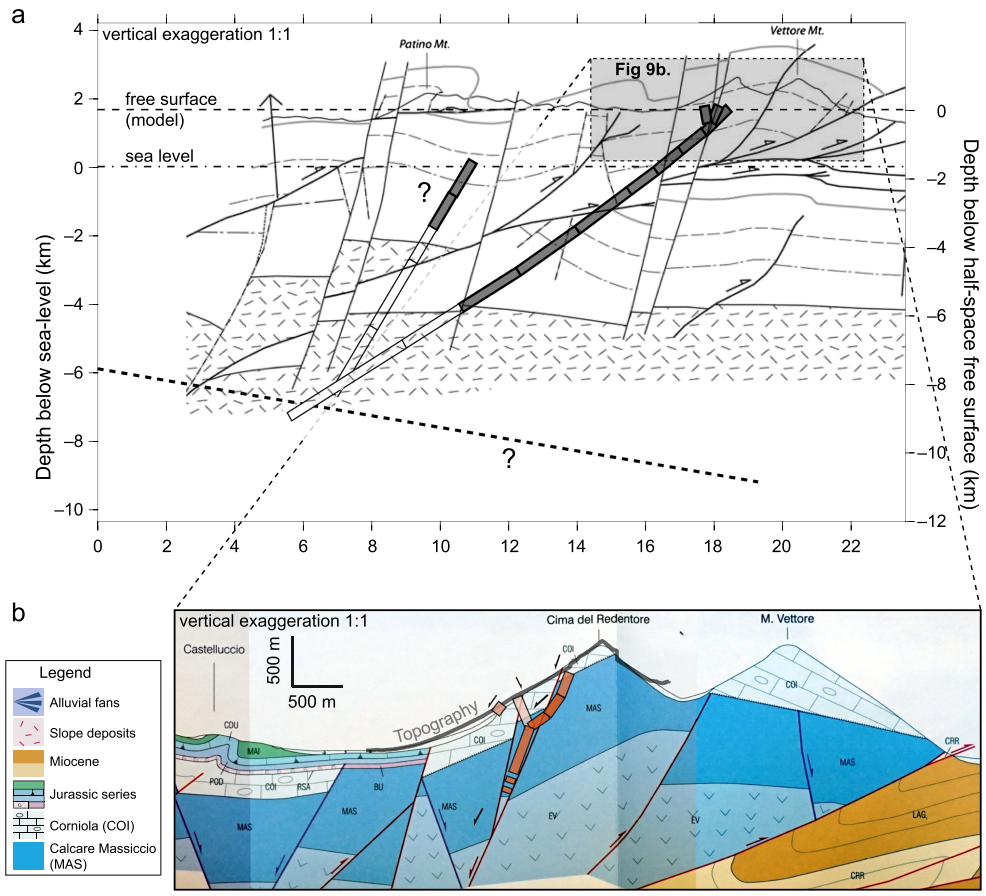

Figure 9. Summary of modeled fault geometry of the causative fault of the 30 October 2016 Norcia earthquake and relationship with structural architecture of the Apennine orogen and quaternary normal fault system. (a) From static slip inversion of large-scale deformation (section 3 and Figures 6d and S10): Large-scale geometry of the coseismic fault suggests a 35–40° dipping plane, which may have partly reactivated east vergent thrusts. Geological cross section from Mazzoli et al. (2005). (b) From forward modeling of near-fault deformation (section 4; Figure 8): detailed geometry in the shallow subsurface (<1-km depth) indicates that the 30 October 2016 reactivated previously mapped normal faults dipping at ~50–70°. Slip on fault planes dipping subparallel to the local slope of 25° is also inferred from observations of surface deformation, suggesting the existence of an additional gravity-driven deformation process interfering with the deep-seated tectonic deformation signal. Note the similarity between inferred dip of the shallow-dipping dislocation and the lithological contact between the MAS formation forming the backbone of the Monte Vettore anticline and the COI formation overlying the MAS. Geological cross section from Pierantoni et al. (2013).

We, however, notice that substantial near-fault short-scale deformation patterns remain unexplained by this first-order model. In particular, both in the footwall and the hanging wall of the MSF, a sharp E-W deformation gradient is not reproduced (yellow ellipse in Figure 8, Scenario 1). This gradient may be explained by a source of strain (i.e., the bottom of the MSF dislocation) situated at shallower depth than in the model of Scenario 1. In a second scenario (2), the width of the MSF is therefore shortened to 0.15 km only, which successfully reproduces the location and magnitude of this residual deformation pattern. A sharp subsidence signal is also produced in the hanging wall of the MSF, within 150 m of the fault trace, which is consistent with the observations from Pleiades (see also Figure 2). This finding indicates that the MSF roots at very shallow depth (<200 m), in spite of the prominent offset measured across its trace at the surface (~1-m dip slip, see Figure S15). This is in keeping with the difficulty to infer a potential connection between this west dipping fault and the two other faults mapped in the area.

It is worth mentioning that, along the MSF, dip values deduced from the field measurements (~70–90°; Figure S19a) are significantly steeper than the ones deduced from Pleiades (53° at the location of the profile considered here; Figure S19b). A satisfying fit to the data, though not as good as in Scenarios 3 and 4, is

obtained by modeling Dislocation C with a dip of ~80°. In this case, the horizontal signal observed in the data requires the addition of an opening component on Dislocation C, which generates ~45 cm of opening and ~80 cm of dip slip. In any case, to produce the localized subsidence (<200 m) and contraction (<500 m) in the hanging wall, Dislocation C has to remain very short and shallow.

In spite of the improvement brought by Scenario 2, a significant residual pattern still remains on the vertical component. Residual uplift occurs near the trace of the MPF, whereas residual subsidence occurs near the trace of the MVF, due to an unmodeled gradient of vertical deformation within 400 m to the west of the trace of the MVF (orange ellipse in Figure 8, Scenario 2). This residual cannot be explained by a dislocation intersecting the surface, since no break is observed in the signal, which appears to be smooth and continuous. Neither would a steeply dipping normal fault (whether dipping toward the east or the west) explains the signal, because it would only produce one "concavity" but would not explain the uplift signal. After conducting several tests, we came to the conclusion that this residual pattern can only be explained by dip slip occurring on a dislocation dipping approximately parallel to the free surface. In a third scenario (3), keeping the same parameters as in Scenario 2, we introduce an additional dislocation, hereafter named "F," dipping 20° toward the east, that is, at 5° from the average local topography, and slipping by 1 m. The depth of this fault is not well constrained but has to be less than 250 m to reproduce the observed gradient of the residual deformation. Including this dislocation allows for explaining the progressive subsidence of the hanging wall of the Monte Vettore as one moves toward the trace of the fault (see also Figure 2).

It is understood that the above models are not unique, in the sense that alternative configurations can yield a similar fit to the data. Furthermore, rigorously accounting for the effects of elasticity, heterogeneity of material properties, damage and gravity would require a more advanced modeling approach (e.g., finite-element modeling), which is beyond the scope of our study. Scenario 4 nevertheless shows another reasonable way to explain our observations, where the MVF flattens at depth. Dip of this fault decreases with increasing depth to become parallel to the topography at 300-m depth, where dip slip reaches 2.6 m. Dislocation D, with a dip slip of 1.3 m, is modeled with a steeper dip (70°) than in the other scenarios and an along-dip width of 1 km. This scenario is equivalent to Scenario 3 in terms of misfits.

Further improvements can be achieved by increasing the degrees of freedom in the model, for instance, by including more dislocations and/or by complicating slip distribution on the faults. However, more complex models lead to an intractable number of unknowns. Nevertheless, after exploring a large number of alternative models, we conclude that, after accounting for the deformation caused by the faults rupturing the surface, a systematic residual motion directed downslope is detected, and that this residual can be explained by normal fault slip on a dislocation lying parallel to the topography of the Monte Vettore western flank, either as a shallow, separate slip surface (Scenario 3), or as part of a shallow, listric structure of the major fault (Scenario 4).

5. Discussion and Conclusions

The three recent earthquake sequences of Central Italy (1997, 2009, and 2016–2017) share a number of similar features, which reflect a more general behavior of normal faults in this region. First, earthquakes tend to occur in swarms, or sequences, lasting for several days to months. These swarms are punctuated by large events that individually rupture one or several segments of the normal fault system. The largest shocks are often, though not systematically, associated with surface ruptures, which can induce locally remarkable offsets (up to 2 m in 2016, see section 2.2). Slip inversions for the 2016 Norcia earthquake as well as previous normal-faulting earthquakes elsewhere, where modern geodetic data and detailed mapping of surface ruptures are available, indicate that slip at depth likely exceeded the value observed at the surface. This feature is reminiscent of the so-called "shallow slip deficit" effect reported for moderate-size continental strike-slip earthquakes (e.g., Fialko et al., 2005; Xu et al., 2016) and may bear a general significance about the mechanical properties of faults in the subsurface.

Our slip inversion confirms that the bulk of the geologic strain budget is released by coseismic slip occurring at depth greater than 2 km. Slip decreases toward the surface while, at the same time, being partitioned on several ruptures, forming a finite-width zone of distributed strain. As a consequence, any individual, local measurement of on-fault offset would only provide a minimum estimate of slip occurring at greater depth.

Based on this assumption, locally recorded paleoseismic coseismic offsets would enable the definition of a lower bound of paleoearthquake magnitude.

However, the most recent 2016–2017 sequence illustrates that additional factors conspire to complicate the link between slip at depth and slip at the surface. First, the sequence demonstrated that, spectacularly, a single coseismic scarp could be activated twice during the same sequence (Perouse et al., 2018; Walters et al., 2018). Repeated activation of a single fault scarp in a short time interval (a few days to months) is difficult to recognize from paleoseismological field observations, which jeopardizes the "minimum slip assumption." Hence, in case of ambiguity it emphasizes the need to multiply paleoseismological investigations for the same fault along strike to minimize chances to mix up successive events into a same paleoearthquake.

Furthermore, and perhaps more importantly, even when one considers only the 30 October 2016 M_w6.5 earthquake, detailed analysis of the deformation field suggests that coseismic deformation at shallow depth is characterized by a previously unreported level of complexity. Indeed, based on the inversion of GPS, InSAR and optical correlation data, we show that slip occurring at shallow depth on the MVF reaches a maximum of 1.5 m, which corresponds to approximately 50 cm of horizontal dilation between the hanging wall and the footwall of the Monte Vettore fault system. On the other hand, relative horizontal displacement (heave) generated on the MVF, MPF, and MSF, within ~1 km across strike along the Monte Vettore western slope, totals ~1 to 1.5 m. The cause of this discrepancy is identified in the form of a sharp fault-perpendicular contraction affecting the hanging wall of the MVF, within 200 m of the MSF (Figures 2 and 8). This feature occurs over a too short spatial wavelength for our large-scale slip inversion to capture it. The small size of this deformation pattern points to a shallow origin (<500-m depth or less). Putting the shallow slip deficit problem the other way round, this shallow concentration of deformation may indicate a shallow excess of slip.

We attempted to reproduce this small-scale deformation using a forward modeling approach, using dislocation theory and simple kinematic reasoning. Although attempts to reproduce these deformations stumble on the inherent nonuniqueness of the problem, permanent features are identified in all models providing a good fit to the data (section 4). Specifically, Scenarios 3 and 4 (Figure 8), which are equally good in term of data fitting, both suggest that the deep MVF connects to the surface in a complex manner. Before reaching the surface, the main fault has to intersect a secondary fault plane (Dislocation F in Scenario 3) or flatten for some distance (Dislocations A2 and A3 in Scenario 4), to accommodate some slip on a plane dipping nearly parallel to the local topography, that is, gently dipping toward the west. The spatial wavelength of near-fault surface deformation suggests that this shallow-dipping fault plane may be located at depths as shallow as 100–300 m under the free surface.

This shallow-dipping plane may be interpreted in two ways: On one hand, it may reflect interbedding slip, as the limestone stratification in the hanging wall of the MVF dips gently toward the WSW (Scenario 3 in Figure 8; Figure 9) (e.g., Brozzetti et al., 2019; Brozzetti & Lavecchia, 1994; Mazzoli et al., 2005; Pierantoni et al., 2013; Scognamiglio et al., 2018). In this specific area, quaternary normal-faulting appears to dismantle a preexisting structural surface that marks the western flank of an east vergent, asymmetrically folded thrust anticline. On the other hand, the local topography on the western flank of Monte Vettore could favor some gravity-driven sliding toward the west, which would be partly accommodated by a shallow-dipping decollement (Scenario 4 in Figure 8). This mechanism may explain the excess of slip visible on Dislocations A2 and A3 of Scenario 4, which is required to fit the data. It is possible that this decollement might localize along some interbedding interface in limestone, similarly to the first possibility. Thus, based on the current data available alone, it is not possible to discriminate further between the two possibilities. Mechanical consideration, however, favors the Scenario 4, as any slip on Dislocation F would increase the normal stress on the shallow part of MPF, making motion on the MPF more difficult. We note that, according to Aryal et al. (2015), a model consisting of dislocations lying parallel to the topography may in good approximation reproduce the displacement field induced by a shallow-seated landslide surface, that is, up to depth as shallow as a few meters. How the geometry of such shallow dislocation evolves deeper down is here out of our reach. Indeed, no slip was accommodated at depth on that plane that could be used to determine such geometry with accuracy during the slip inversion process.

The assumption of a shallow-dipping fault section sitting at shallow depth (<300 m), as inferred from our forward models, is actually reinforced by an independent analysis of COSMO-SkyMed interferograms, which show local patterns of deformation attributed to landsliding, in a similar location, on the Monte

Vettore western flank, triggered by the 24 August 2016 Amatrice event (Huang et al., 2017). This landsliding could have been reactivated by shaking induced by the stronger and closer M_w6.5 30 October 2016 earthquake, thereby adding some gravity-driven motion to the predominant tectonic slip component. The recent geomechanical model of Di Naccio et al. (2019) also heads in this direction, showing that the steep western slope of Monte Vettore is prone to destabilization, in particular due to the presence of tectonic faults marking the contact between lithologies with contrasting mechanical behavior.

The MSF, on the other hand, does not appear to connect with any deep-seated fault at depth (section 4). A possible interpretation would be that this fault also accommodates gravity-driven landsliding along the prominent Monte Vettore slope. We note that this inferred fault marks the contact between the uplifted consolidated Corniola formation and looser slope deposits farther downhill (Figures 7 and 9). The southern part of the MSF may therefore be interpreted as a tectonic fault with a gravitational component of motion. In this perspective, although rupture complexity and very short distances between fault strands prevent any quantitative modeling, the geometry of the MSF northward of our profile reinforces this interpretation (Figure 7). About 1 km north of Profile B-B′, the MSF intersects the MPF and develops an arcuate shape concave toward the east. A significant downslope motion (>1 m), limited to a zone of about 200 m west from the scarp, is visible along this section of the scarp, which is also consistent with some localized shallow landsliding.

The detailed structural architecture of this inferred landslide and its connection with tectonic faults remains to be determined. However, owing to the geometrical relations between the MPF and the MSF and the fact that the MPF is likely deeply rooted compared to the MSF, we could hypothesize a scenario whereby the MVF and the MPF are first activated during the earthquake proper, while the MSF would move only in a second stage along a shallow sliding surface, to crosscut the MPF primary surface ruptures and localize against the western edge of the more consolidated Corniola formation. Our data do not allow for determining whether this secondary faulting took place almost instantly after the main rupture or during the following hours. In any case it was likely aseismic and could not be tracked in seismological data.

Regarding dip along the MSF, we acknowledge that values deduced from field measurements and from our deformation maps differ significantly. An alternative scenario to Scenarios 3 and 4, where Dislocation C has a steeper dip (~80°), requires an opening component to achieve a satisfying fit to the data. We have no evidence in available field observations to favor the existence of such an opening component on the MSF. Nevertheless, as in Scenarios 3 and 4, forward modeling with a mixed opening and dip-slip dislocation requires a similarly shallow dislocation (<150 m). In any case, if substantial coseismic opening actually happened on the MSF, our modeling suggests that it was sufficiently strong to induce a substantial E-W contraction of the hanging wall of the MSF (<200 m; Figure 2c) and subsidence at short distance from the fault (<50 m; Figure 2d). Due to the location of the MSF trace along a steep slope, a process involving gravitational stresses inducing fault opening and driving motion downslope (i.e., toward the west and downward) may also explain this localized, asymmetrical signal. The triggering mechanism for this landsliding process remains to be understood, although repeated shaking during the 2016 sequence could have favored slope failure.

The above analysis is nonunique, and the presence of a gravity-driven component in the deformation cannot be fully demonstrated on the sole basis of the data available here, mainly because the deformation signal is dominated by the tectonic component. Nonetheless, our data suggest that significant off-fault deformation occurs close to the faults associated with spectacular surface offsets on fault. This feature may arise from changes in fault dip and/or splay faulting as slip propagated toward the surface. Alternatively, sharp variations in slip magnitude may also account for this local deformation. Finally, inelastic behavior of rocks may also explain the failure of our elastic models to fully reproduce the strain observed near the faults, especially in the hanging wall of the MVF where lithological contrasts have been suggested to occur at shallow depth. The respective influence of additional processes, such as inelastic deformation (Cappa et al., 2014), rheological layering (Cattin et al., 1999), changes in the dip angle and/or strike angle of the fault plane (Iezzi et al., 2018; Tung & Masterlark, 2018), splay faulting (Bruhn & Schultz, 1996), or response to dynamic stress changes (Belardinelli et al., 1999), remains to be explored in detail.

Whichever mechanism is actually at play, the observation of substantial off-fault deformation within a few hundred meters of surface ruptures suggests that complex processes prevail at shallow depth. Although the

30 October 2016 earthquake corresponds to the activation of a tectonic fault, whose rupture dominates the deformation signal, additional, secondary processes may concur to increase or inhibit the surface expression of slip occurring at greater depth. During the 30 October 2016 Norcia earthquake, the most impressive surface ruptures were observed in an area characterized by a steep topographic slope (30–40°), inherited from a structural surface. In this specific location, gravity-driven stresses may have acted hand in hand with tectonic stresses so as to enhance surface slip. This interference may have been facilitated by the presence of lithological bedding dipping subparallel to the topographic slope, which may have acted as weakness planes playing the role of a basal decollement (e.g., Di Naccio et al., 2019). Awareness of the existence of these complex processes, which take place at shallow depth (<500 m), means that caution should be taken when interpreting surface offsets in terms of average slip at depth, especially for past earthquakes, where sporadic estimates of surface offsets are often the only available information.

Acknowledgments
The Pleiades images were provided by the CEOS Seismic Hazards Pilot from ESA (http://ceos.org/ourwork/workinggroups/disasters/earthquakes/) and the ISIS program from CNES (https://dinamis.teledetection.fr and https://cnes.fr) and could be accessed through these programs. ALOS-2 data were provided under a cooperative research contract between GSI and JAXA (https://www.gsi.go.jp/cais/topic161108-index-e.html). The ownership of ALOS-2 data belongs to JAXA. Other data are freely available following herein references. Numerical computations were partly performed on the S-CAPAD platform, IPGP, France. We thank Stéphane Baize (IRSN) and Eugénie Pérouse (CEREGE) for the additional information about the field data from Villani, Civico, et al. (2018). We also thank Lucilla Benedetti (CEREGE) and Robin Lacassin (IPGP) for the constructive exchanges during the discussion. R. G. thanks Romain Jolivet (ENS Paris) for sharing the CSI toolbox. The authors would like to acknowledge Richard Walters (Durham University), Marcello Viti (University of Siena), and one anonymous reviewer for their comments that helped improve the manuscript. This study contributes to the IdEx Université de Paris ANR-18-IDEX-0001. This is IPGP contribution 4113.

References

Aryal, A., Brooks, B. A., & Reid, M. E. (2015). Landslide subsurface slip geometry inferred from 3-D surface displacement fields. *Geophysical Research Letters*, *42*, 1411–1417. https://doi.org/10.1002/2014GL062688

Avallone, A., Selvaggi, G., D'Anastasio, E., D'Agostino, N., Pietrantonio, G., Riguzzi, F., et al. (2010). The RING network: Improvement of a GPS velocity field in the central Mediterranean. *Annals of Geophysics*, *53*(2), 39–54. https://doi.org/10.4401/ag-4549

Ayoub, F., Leprince, S., Binet, R., Lewis, K. W., Aharonson, O., & Avouac, J. P. (2008). Influence of camera distortions on satellite image registration and change detection applications. In *Geoscience and Remote Sensing Symposium, 2008. IGARSS 2008. IEEE International* (Vol. 2, pp. II-1072). Boston, MA: IEEE.

Belardinelli, M. E., Cocco, M., Coutant, O., & Cotton, F. (1999). Redistribution of dynamic stress during coseismic ruptures: Evidence for fault interaction and earthquake triggering. *Journal of Geophysical Research*, *104*(B7), 14,925–14,945.

Berthier, E., Vadon, H., Baratoux, D., Arnaud, Y., Vincent, C., Feigl, K. L., et al. (2005). Surface motion of mountain glaciers derived from satellite optical imagery. *Remote Sensing of Environment*, *95*(1), 14–28. https://doi.org/10.1016/j.rse.2004.11.005

Binet, R., & Bollinger, L. (2005). Horizontal coseismic deformation of the 2003 Bam (Iran) earthquake measured from SPOT-5 THR satellite imagery. *Geophysical Research Letters*, *32*, L02307. https://doi.org/10.1029/2004GL021897

Blumetti, A. M., Dramis, F., & Michetti, A. M. (1993). Fault-generated mountain fronts in the central Apennines (Central Italy): Geomorphological features and seismotectonic implications. *Earth Surface Processes and Landforms*, *18*(3), 203–223. https://doi.org/10.1002/esp.3290180304

Booth, A. M., Lamb, M. P., Avouac, J. P., & Delacourt, C. (2013). Landslide velocity, thickness, and rheology from remote sensing: La Clapière landslide, France. *Geophysical Research Letters*, *40*, 4299–4304. https://doi.org/10.1002/grl.50828

Boschi, E., Guidoboni, E., Ferrari, G., Mariotti, D., Valensise, G., & Gasperini, P. (2000). Catalogue of strong Italian earthquakes from 461 BC to 1997 (appendix to volume 43 N° 4, 2000). *Annals of Geophysics*, *43*(4), 609–868. https://doi.org/10.4401/ag-3668

Brozzetti, F., Boncio, P., Cirillo, D., Ferrarini, F., de Nardis, R., Testa, A., et al. (2019). High-resolution field mapping and analysis of the August–October 2016 coseismic surface faulting (central Italy earthquakes): Slip distribution, parameterization, and comparison with global earthquakes. *Tectonics*, *38*(2), 417–439. https://doi.org/10.1029/2018TC005305

Brozzetti, F., & Lavecchia, G. (1994). Seismicity and related extensional stress field: The case of the Norcia Seismic Zone (Central Italy). In *Annales tectonicae* (Vol. 8, pp. 36–57), Italy: Consiglio Nazionale delle Ricerche.

Bruhn, R. L., & Schultz, R. A. (1996). Geometry and slip distribution in normal fault systems: Implications for mechanics and fault-related hazards. *Journal of Geophysical Research*, *101*(B2), 3401–3412. https://doi.org/10.1029/95JB03253

Cappa, F., Perrin, C., Manighetti, I., & Delor, E. (2014). Off-fault long-term damage: A condition to account for generic, triangular earthquake slip profiles. *Geochemistry, Geophysics, Geosystems*, *15*, 1476–1493. https://doi.org/10.1002/2013GC005182

Caskey, S. J. (1995). Geometric relations of dip slip to a faulted ground surface: New nomograms for estimating components of fault displacement. *Journal of Structural Geology*, *17*(8), 1197–1202. https://doi.org/10.1016/0191-8141(95)00023-7

Caskey, S. J., Wesnousky, S. G., Zhang, P., & Slemmons, D. B. (1996). Surface faulting of the 1954 Fairview Peak (MS 7.2) and Dixie Valley (MS 6.8) earthquakes, central Nevada. *Bulletin of the Seismological Society of America*, *86*(3), 761–787.

Cattin, R., Briole, P., Lyon-Caen, H., Bernard, P., & Pinettes, P. (1999). Effects of superficial layers on coseismic displacements for a dip-slip fault and geophysical implications. *Geophysical Journal International*, *137*(1), 149–158. https://doi.org/10.1046/j.1365-246x.1999.00779.x

Cello, G., Mazzoli, S., & Tondi, E. (1998). The crustal fault structure responsible for the 1703 earthquake sequence of central Italy. *Journal of Geodynamics*, *26*(2-4), 443–460. https://doi.org/10.1016/S0264-3707(97)00051-3

Cheloni, D., De Novellis, V., Albano, M., Antonioli, A., Anzidei, M., Atzori, S., et al. (2017). Geodetic model of the 2016 Central Italy earthquake sequence inferred from InSAR and GPS data. *Geophysical Research Letters*, *44*, 6778–6787. https://doi.org/10.1002/2017GL073580

Chiaraluce, L., Di Stefano, R., Tinti, E., Scognamiglio, L., Michele, M., Casarotti, E., et al. (2017). The 2016 central Italy seismic sequence: A first look at the mainshocks, aftershocks, and source models. *Seismological Research Letters*, *88*(3), 757–771. https://doi.org/10.1785/0220160221

Cinti, F. R., Cucci, L., Marra, F., & Montone, P. (2000). The 1997 Umbria-Marche earthquakes (Italy): Relation between the surface tectonic breaks and the area of deformation. *Journal of Seismology*, *4*(4), 333–343. https://doi.org/10.1023/A:1026575219394

Civico, R., Pucci, S., Villani, F., Pizzimenti, L., De Martini, P. M., Nappi, R., & Open EMERGEO Working Group (2018). Surface ruptures following the 30 October 2016 M_w 6.5 Norcia earthquake, central Italy. *Journal of Maps*, *14*(2), 151–160. https://doi.org/10.1080/17445647.2018.1441756

Copley, A., Hollingsworth, J., & Bergman, E. (2012). Constraints on fault and lithosphere rheology from the coseismic slip and postseismic afterslip of the 2006 M_w7. 0 Mozambique earthquake. *Journal of Geophysical Research*, *117*, B03404. https://doi.org/10.1029/2011JB008580

D'Agostino, N. (2014). Complete seismic release of tectonic strain and earthquake recurrence in the Apennines (Italy). *Geophysical Research Letters*, *41*, 1155–1162. https://doi.org/10.1002/2014GL059230

De Guidi, G., Vecchio, A., Brighenti, F., Caputo, R., Carnemolla, F., Di Pietro, A., et al. (2017). Brief communication: Co-seismic displacement on 26 and 30 October 2016 (M_w = 5.9 and 6.5)—Earthquakes in central Italy from the analysis of a local GNSS network. *Natural Hazards and Earth System Sciences*, *17*(11), 1885–1892. https://doi.org/10.5194/nhess-17-1885-2017

Devoti, R. (2012). Combination of coseismic displacement fields: A geodetic perspective. *Annals of Geophysics*, *55*, 4. https://doi.org/10.4401/ag-6119

Di Naccio, D., Kastelic, V., Carafa, M. M. C., Esposito, C., Milillo, P., & Di Lorenzo, C. (2019). Gravity versus Tectonics: The case of 2016 Amatrice and Norcia (central Italy) earthquakes surface coseismic fractures. *Journal of Geophysical Research: Earth Surface*, *124*, 994–1017. https://doi.org/10.1029/2018JF004762

Dominguez, S., Avouac, J. P., & Michel, R. (2003). Horizontal coseismic deformation of the 1999 Chi-Chi earthquake measured from SPOT satellite images: Implications for the seismic cycle along the western foothills of central Taiwan. *Journal of Geophysical Research*, *108*(B2), 2083. https://doi.org/10.1029/2001JB000951

Elliott, J. R., Walters, R. J., England, P. C., Jackson, J. A., Li, Z., & Parsons, B. (2010). Extension on the Tibetan Plateau: Recent normal faulting measured by InSAR and body wave seismology. *Geophysical Journal International*, *183*(2), 503–535. https://doi.org/10.1111/j.1365-246X.2010.04754.x

EMERGEO Working Group (2010). Evidence for surface rupture associated with the M_w 6.3 L'Aquila earthquake sequence of April 2009 (central Italy). *Terra Nova*, *22*(1), 43–51. https://doi.org/10.1111/j.1365-3121.2009.00915.x

Fialko, Y., Sandwell, D., Simons, M., & Rosen, P. (2005). Three-dimensional deformation caused by the Bam, Iran, earthquake and the origin of shallow slip deficit. *Nature*, *435*(7040), 295–299. https://doi.org/10.1038/nature03425

Fujiwara, S., Nishimura, T., Murakami, M., Nakagawa, H., Tobita, M., & Rosen, P. A. (2000). 2.5-D surface deformation of M6.1 earthquake near Mt Iwate detected by SAR interferometry. *Geophysical Research Letters*, *27*(14), 2049–2052. https://doi.org/10.1029/1999GL011291

Galadini, F., & Galli, P. (2000). Active tectonics in the central Apennines (Italy)—Input data for seismic hazard assessment. *Natural Hazards*, *22*(3), 225–268. https://doi.org/10.1023/A:1008149531980

Galli, P., Castenetto, S., & Peronace, E. (2017). The macroseismic intensity distribution of the 30 October 2016 earthquake in central Italy (M_w 6.6): Seismotectonic implications. *Tectonics*, *36*, 2179–2191. https://doi.org/10.1002/2017TC004583

Galli, P., Galadini, F., & Calzoni, F. (2005). Surface faulting in Norcia (central Italy): A "paleoseismological perspective". *Tectonophysics*, *403*(1-4), 117–130. https://doi.org/10.1016/j.tecto.2005.04.003

Grandin, R., Socquet, A., Binet, R., Klinger, Y., Jacques, E., de Chabalier, J. B., et al. (2009). September 2005 Manda Hararo-Dabbahu rifting event, Afar (Ethiopia): constraints provided by geodetic data. *Journal of Geophysical Research*, *114*, B08404. https://doi.org/10.1029/2008JB005843

Guerrieri, L., Baer, G., Hamiel, Y., Amit, R., Blumetti, A. M., Comerci, V., et al. (2010). InSAR data as a field guide for mapping minor earthquake surface ruptures: Ground displacements along the Paganica Fault during the 6 April 2009 L'Aquila earthquake. *Journal of Geophysical Research*, *115*, B12331. https://doi.org/10.1029/2010JB007579

Guidoboni, E., Ferrari, G., Mariotti, D., Comastri, A., Tarabusi, G., & Valensise, G. (2007). Catalogue of Strong Earthquakes in Italy (461 BC-1997) and Mediterranean Area (760 BC-1500). *INGV-SGA*. Available from http://storing.ingv.it/cfti4med/.

Heid, T., & Kääb, A. (2012). Evaluation of existing image matching methods for deriving glacier surface displacements globally from optical satellite imagery. *Remote Sensing of Environment*, *118*, 339–355. https://doi.org/10.1016/j.rse.2011.11.024

Hollingsworth, J., Leprince, S., Ayoub, F., & Avouac, J. P. (2013). New constraints on dike injection and fault slip during the 1975–1984 Krafla rift crisis, NE Iceland. *Journal of Geophysical Research: Solid Earth*, *118*, 3707–3727. https://doi.org/10.1002/jgrb.50223

Huang, M. H., Fielding, E. J., Liang, C., Milillo, P., Bekaert, D., Dreger, D., & Salzer, J. (2017). Coseismic deformation and triggered landslides of the 2016 M_w 6.2 Amatrice earthquake in Italy. *Geophysical Research Letters*, *44*, 1266–1274. https://doi.org/10.1002/2016GL071687

Iezzi, F., Mildon, Z., Walker, J. F., Roberts, G., Goodall, H., Wilkinson, M., & Robertson, J. (2018). Coseismic throw variation across along-strike bends on active normal faults: Implications for displacement versus length scaling of earthquake ruptures. *Journal of Geophysical Research: Solid Earth*, *123*, 9817–9841. https://doi.org/10.1029/2018JB016732

Jacques, E., Kidane, T., Tapponnier, P., Manighetti, I., Gaudemer, Y., Meyer, B., et al. (2011). Normal faulting during the August 1989 earthquakes in central Afar: Sequential triggering and propagation of rupture along the Dôbi Graben. *Bulletin of the Seismological Society of America*, *101*(3), 994–1023. https://doi.org/10.1785/0120080317

Klinger, Y., Michel, R., & King, G. C. P. (2006). Evidence for an earthquake barrier model from $M_w \sim 7.8$ Kokoxili (Tibet) earthquake slip-distribution. *Earth and Planetary Science Letters*, *242*(3-4), 354–364. https://doi.org/10.1016/j.epsl.2005.12.003

Klinger, Y., Okubo, K., Vallage, A., Champenois, J., Delorme, A., Rougier, E., et al. (2018). Earthquake damage patterns resolve complex rupture processes. *Geophysical Research Letters*, *45*, 10,279–10,287. https://doi.org/10.1029/2018GL078842

Lawson, C. L., & Hanson, R. J. (1995). *Solving least squares problems* (Vol. 15). Philadelphia, PA: Siam.

Leprince, S., Barbot, S., Ayoub, F., & Avouac, J. P. (2007). Automatic and precise orthorectification, coregistration, and subpixel correlation of satellite images, application to ground deformation measurements. *IEEE Transactions on Geoscience and Remote Sensing*, *45*(6), 1529–1558. https://doi.org/10.1109/TGRS.2006.888937

Lohman, R. B., & Simons, M. (2005). Some thoughts on the use of InSAR data to constrain models of surface deformation: Noise structure and data downsampling. *Geochemistry, Geophysics, Geosystems*, *6*, Q01007. https://doi.org/10.1029/2004GC000841

Lundgren, P., & Stramondo, S. (2002). Slip distribution of the 1997 Umbria-Marche earthquake sequence: Joint inversion of GPS and synthetic aperture radar interferometry data. *Journal of Geophysical Research*, *107*(B11), 2316. https://doi.org/10.1029/2000JB000103

Mackenzie, D., & Elliott, A. (2017). Untangling tectonic slip from the potentially misleading effects of landform geometry. *Geosphere*, *13*(4), 1310–1328. https://doi.org/10.1130/GES01386.1

Mazzoli, S., Pierantoni, P. P., Borraccini, F., Paltrinieri, W., & Deiana, G. (2005). Geometry, segmentation pattern and displacement variations along a major Apennine thrust zone, central Italy. *Journal of Structural Geology*, *27*(11), 1940–1953. https://doi.org/10.1016/j.jsg.2005.06.002

Meyer, B., Armijo, R., Massonnet, D., De Chabalier, J. B., Delacourt, C., Ruegg, J. C., et al. (1996). The 1995 Grevena (Northern Greece) earthquake: Fault model constrained with tectonic observations and SAR interferometry. *Geophysical Research Letters*, *23*(19), 2677–2680. https://doi.org/10.1029/96GL02389

Michel, R., Avouac, J. P., & Taboury, J. (1999a). Measuring ground displacements from SAR amplitude images: Application to the Landers earthquake. *Geophysical Research Letters*, *26*(7), 875–878. https://doi.org/10.1029/1999GL900138

Michel, R., Avouac, J. P., & Taboury, J. (1999b). Measuring near field coseismic displacements from SAR images: Application to the Landers earthquake. *Geophysical Research Letters*, *26*(19), 3017–3020. https://doi.org/10.1029/1999GL900524

Okada, Y. (1985). Surface deformation due to shear and tensile faults in a half-space. *Bulletin of the Seismological Society of America*, *75*(4), 1135–1154.

Palumbo, L., Benedetti, L., Bourles, D., Cinque, A., & Finkel, R. (2004). Slip history of the Magnola fault (Apennines, Central Italy) from 36Cl surface exposure dating: Evidence for strong earthquakes over the Holocene. *Earth and Planetary Science Letters*, *225*(1-2), 163–176. https://doi.org/10.1016/j.epsl.2004.06.012

Pantosti, D., D'Addezio, G., & Cinti, F. R. (1996). Paleoseismicity of the Ovindoli-Pezza fault, central Apennines, Italy: A history including a large, previously unrecorded earthquake in the Middle Ages (860–1300 AD). *Journal of Geophysical Research*, *101*(B3), 5937–5959. https://doi.org/10.1029/95JB03213

Perouse, E., Benedetti, L., Fleury, J., Rizza, M., Puliti, I., Billant, J., et al. (2018). Coseismic slip vectors of 24 August and 30 October 2016 earthquakes in Central Italy: Oblique slip and regional kinematic implications. *Tectonics*, *37*(10), 3760–3781. https://doi.org/10.1029/2018TC005083

Piccardi, L., Gaudemer, Y., Tapponnier, P., & Boccaletti, M. (1999). Active oblique extension in the central Apennines (Italy): Evidence from the Fucino region. *Geophysical Journal International*, *139*(2), 499–530. https://doi.org/10.1046/j.1365-246x.1999.00955.x

Pierantoni, P., Deiana, G., & Galdenzi, S. (2013). Stratigraphic and structural features of the Sibillini mountains (Umbria-Marche Apennines, Italy). *Italian Journal of Geosciences*, *132*(3), 497–520. https://doi.org/10.3301/IJG.2013.08

Pierrot-Deseilligny, M., & Paparoditis, N. (2006). A multiresolution and optimization-based image matching approach: An application to surface reconstruction from SPOT5-HRS stereo imagery. *Archives of Photogrammetry, Remote Sensing and Spatial Information Sciences*, 36(1/W41), Ankara, Turkey.

Pizzi, A., Di Domenica, A., Gallovič, F., Luzi, L., & Puglia, R. (2017). Fault segmentation as constraint to the occurrence of the main shocks of the 2016 Central Italy seismic sequence. *Tectonics*, *36*, 2370–2387. https://doi.org/10.1002/2017TC004652

Pucci, S., De Martini, P. M., Civico, R., Villani, F., Nappi, R., Ricci, T., et al. (2017). Coseismic ruptures of the 24 August 2016, M_w 6.0 Amatrice earthquake (central Italy). *Geophysical Research Letters*, *44*, 2138–2147. https://doi.org/10.1002/2016GL071859

Radiguet, M., Cotton, F., Vergnolle, M., Campillo, M., Valette, B., Kostoglodov, V., & Cotte, N. (2011). Spatial and temporal evolution of a long term slow slip event: The 2006 Guerrero Slow Slip Event. *Geophysical Journal International*, *184*(2), 816–828. https://doi.org/10.1111/j.1365-246X.2010.04866.x

Raucoules, D., Ristori, B., de Michele, M., & Briole, P. (2010). Surface displacement of the M_w 7 Machaze earthquake (Mozambique): Complementary use of multiband InSAR and radar amplitude image correlation with elastic modelling. *Remote Sensing of Environment*, *114*(10), 2211–2218. https://doi.org/10.1016/j.rse.2010.04.023

Rockwell, T. K., Lindvall, S., Dawson, T., Langridge, R., Lettis, W., & Klinger, Y. (2002). Lateral offsets on surveyed cultural features resulting from the 1999 Izmit and Duzce earthquakes, Turkey. *Bulletin of the Seismological Society of America*, *92*(1), 79–94. https://doi.org/10.1785/0120000809

Rosu, A. M., Pierrot-Deseilligny, M., Delorme, A., Binet, R., & Klinger, Y. (2015). Measurement of ground displacement from optical satellite image correlation using the free open-source software MicMac. *ISPRS Journal of Photogrammetry and Remote Sensing*, *100*, 48–59. https://doi.org/10.1016/j.isprsjprs.2014.03.002

Rupnik, E., Daakir, M., & Deseilligny, M. P. (2017). MicMac—A free, open-source solution for photogrammetry. *Open Geospatial Data, Software and Standards*, *2*(1), 14. https://doi.org/10.1186/s40965-017-0027-2

Rupnik, E., Deseilligny, M. P., Delorme, A., & Klinger, Y. (2016). Refined satellite image orientation in the free open-source photogrammetric tools APERO/MICMAC. *ISPRS Annals of the Photogrammetry, Remote Sensing and Spatial Information Sciences*, *III-1*, 83–90. https://doi.org/10.5194/isprs-annals-III-1-83-2016

Saint Fleur, N., Feuillet, N., Grandin, R., Jacques, E., Weil-Accardo, J., & Klinger, Y. (2015). Seismotectonics of southern Haiti: A new faulting model for the 12 January 2010 M7.0 earthquake. *Geophysical Research Letters*, *42*, 10–273. https://doi.org/10.1002/2015GL065505

Schlagenhauf, A. (2009). Identification des forts séismes passés sur les failles normales actives de la région Lazio-Abruzzo (Italie Centrale) par 'datations cosmogéniques' (36Cl) de leurs escarpements (Doctoral dissertation, Université Joseph-Fourier-Grenoble I).

Schlagenhauf, A., Manighetti, I., Benedetti, L., Gaudemer, Y., Finkel, R., Malavieille, J., & Pou, K. (2011). Earthquake supercycles in Central Italy, inferred from 36Cl exposure dating. *Earth and Planetary Science Letters*, *307*(3-4), 487–500. https://doi.org/10.1016/j.epsl.2011.05.022

Scognamiglio, L., Tinti, E., Casarotti, E., Pucci, S., Villani, F., Cocco, M., et al. (2018). Complex fault geometry and rupture dynamics of the M_w 6.5, 30 October 2016, Central Italy earthquake. *Journal of Geophysical Research: Solid Earth*, *123*, 2943–2964. https://doi.org/10.1002/2018JB015603

Smeraglia, L., Billi, A., Carminati, E., Cavallo, A., & Doglioni, C. (2017). Field-to nano-scale evidence for weakening mechanisms along the fault of the 2016 Amatrice and Norcia earthquakes, Italy. *Tectonophysics*, *712*, 156–169.

Socquet, A., Hollingsworth, J., Pathier, E., & Bouchon, M. (2019). Evidence of supershear during the 2018 magnitude 7.5 Palu earthquake from space geodesy. *Nature Geoscience*, *12*(3), 192–199. https://doi.org/10.1038/s41561-018-0296-0

Stumpf, A., Malet, J. P., Allemand, P., & Ulrich, P. (2014). Surface reconstruction and landslide displacement measurements with Pléiades satellite images. *ISPRS Journal of Photogrammetry and Remote Sensing*, *95*, 1–12. https://doi.org/10.1016/j.isprsjprs.2014.05.008

Tarantola, A. (2005). *Inverse problem theory and methods for model parameter estimation* (Vol. 89). Paris, France: Siam.

Tinti, S., & Armigliato, A. (2002). A 2-D hybrid technique to model the effect of topography on coseismic displacements. Application to the Umbria-Marche (central Italy) 1997 earthquake sequence. *Geophysical Journal International*, *150*(2), 542–557. https://doi.org/10.1046/j.1365-246X.2002.01721.x

Tung, S., & Masterlark, T. (2018). Resolving source geometry of the 24 August 2016 Amatrice, central Italy, earthquake from InSAR data and 3D finite-element modeling. *Bulletin of the Seismological Society of America*, *108*(2), 553–572. https://doi.org/10.1785/0120170139

Vallage, A., Klinger, Y., Grandin, R., Bhat, H. S., & Pierrot-Deseilligny, M. (2015). Inelastic surface deformation during the 2013 M_w 7.7 Balochistan, Pakistan, earthquake. *Geology*, *43*(12), 1079–1082.

Vallage, A., Klinger, Y., Lacassin, R., Delorme, A., & Pierrot-Deseilligny, M. (2016). Geological structures control on earthquake ruptures: The M_w7.7, 2013, Balochistan earthquake, Pakistan. *Geophysical Research Letters*, *43*, 10,155–10,163. https://doi.org/10.1002/2016GL070418

Van Puymbroeck, N., Michel, R., Binet, R., Avouac, J. P., & Taboury, J. (2000). Measuring earthquakes from optical satellite images. *Applied Optics*, *39*(20), 3486–3494. https://doi.org/10.1364/ao.39.003486

Villani, F., Civico, R., Pucci, S., Pizzimenti, L., Nappi, R., De Martini, P. M., & the Open EMERGEO Working Group (2018). A database of the coseismic effects following the 30 October 2016 Norcia earthquake in Central Italy. *Scientific Data*, *5*, 180049. https://doi.org/10.1038/sdata.2018.49

Villani, F., Pucci, S., Civico, R., De Martini, P. M., Cinti, F. R., & Pantosti, D. (2018). Surface faulting of the 30 October 2016 M_w 6.5 central Italy earthquake: Detailed analysis of a complex coseismic rupture. *Tectonics*, *37*(10), 3378–3410. https://doi.org/10.1029/2018TC005175

Walters, R. J., Elliott, J. R., D'agostino, N., England, P. C., Hunstad, I., Jackson, J. A., et al. (2009). The 2009 L'Aquila earthquake (central Italy): A source mechanism and implications for seismic hazard. *Geophysical Research Letters*, *36*, L17312. https://doi.org/10.1029/2009GL039337

Walters, R. J., Gregory, L. C., Wedmore, L. N. J., Craig, T. J., McCaffrey, K., Wilkinson, M., et al. (2018). Dual control of fault intersections on stop-start rupture in the 2016 Central Italy seismic sequence. *Earth and Planetary Science Letters*, *500*, 1–14. https://doi.org/10.1016/j.epsl.2018.07.043

Wedmore, L. N. J., Gregory, L. C., McCaffrey, K. J. W., Goodall, H., & Walters, R. J. (2019). Partitioned off-fault deformation in the 2016 Norcia earthquake captured by differential terrestrial laser scanning. *Geophysical Research Letters*, *46*, 3199–3205. https://doi.org/10.1029/2018GL080858

Wells, D. L., & Coppersmith, K. J. (1994). New empirical relationships among magnitude, rupture length, rupture width, rupture area, and surface displacement. *Bulletin of the Seismological Society of America*, *84*(4), 974–1002.

Xu, G., Xu, C., Wen, Y., & Jiang, G. (2017). Source Parameters of the 2016–2017 Central Italy Earthquake Sequence from the Sentinel-1, ALOS-2 and GPS Data. *Remote Sensing*, *9*(11), 1182. https://doi.org/10.3390/rs9111182

Xu, X., Tong, X., Sandwell, D. T., Milliner, C. W., Dolan, J. F., Hollingsworth, J., et al. (2016). Refining the shallow slip deficit. *Geophysical Journal International*, *204*(3), 1867–1886. https://doi.org/10.1093/gji/ggv563

Tectonics

Supporting Information for

Complex deformation at shallow depth during the 30 October 2016 Mw6.5 Norcia earthquake: interference between tectonic and gravity processes

A. Delorme[1], R. Grandin[1], Y. Klinger[1], M. Pierrot-Deseilligny[2], N. Feuillet[1], E. Jacques[1], E. Rupnik[2], Y. Morishita[3]

[1]Université de Paris, Institut de physique du globe de Paris, CNRS, F-75005 Paris, France, [2]LaSTIG, IGN, ENSG, Univ. Paris-Est F-94160, Saint-Mandé, France, [3]Geospatial Information Authority of Japan, Kitasato-1, Tsukuba, Ibaraki 305-0811, Japan

Contents of this file

Additional Supporting Information (Files uploaded separately)

Text S1. Integration of the field observations from Villani, Civico et al. (2018)

We compare the throw and opening values collected in the field by Villani, Civico et al. (2018) with the throw and heave measurements made in the surface deformation maps derived from the Pleiades data (Figure S21). For each field measurement that includes throw, opening and dip angle, the dip of the dip-slip vector (Δ) deduced from the throw (T_{Fld}) and opening (O_{Fld}) values is computed:

$$\Delta = \tan\left(\frac{T_{Fld}}{O_{Fld}}\right)$$

Δ is compared to the dip angle (D_{Fld}) and measurement points for which the difference Δ-D_{Fld} exceeds 10° are filtered out.

Among the field observations recorded, some have a dip angle value and no opening and/or throw values, but offset (Off_{Fld}) and plunge (P_{Fld}) values. For such records, heave and/or throw can be approximately deduced. The offset vector is a three-dimensional vector that can include lateral slip. For measurements where a rake value (R_{Fld}) is provided, the component of the offset vector that belongs to the plane defined by the throw and heave vectors ($Off^{\perp}_{Fld}$) is computed:

$$Off^{\perp}_{Fld} = Off_{Fld} * \sin\left(R_{Fld}\right)$$

For measurements where there is no rake value, we make the assumption that $Off^{\perp}_{Fld}$ equals Off_{Fld}. Finally the opening and throw are computed:

$$O_{Fld} = Off^{\perp}_{Fld} * \cos\left(P_{Fld}\right)$$

$$T_{Fld} = Off^{\perp}_{Fld} * \sin\left(P_{Fld}\right)$$

Quantity and proportion of the field observations of the different categories (i.e. where (1) the opening and throw values are provided, (2) the opening and/or throw values are missing, but the offset, plunge and rake values are provided, (3) the opening and/or throw values are missing, the offset and plunge values are provided, but the rake is missing) are reported, for each fault system, in Table S5.

Only field observations belonging to one of the three categories defined are considered for comparison with the measurements from the Pleiades data.

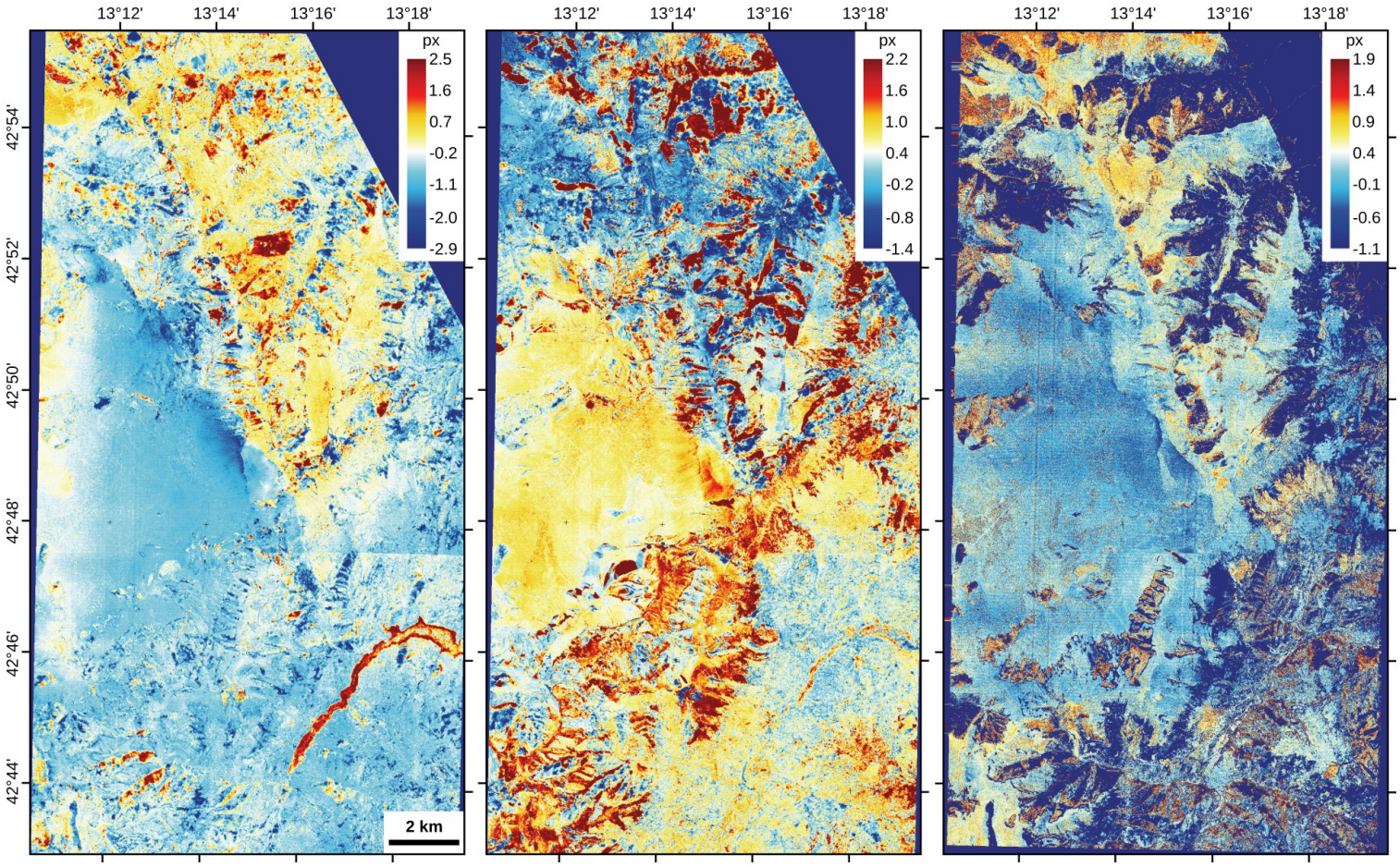

Figure S1. Maps of the coseismic deformation during the Norcia earthquake, computed from the satellite optical images, for the E-W (on the left; positive toward the E), N-S (in the center; positive toward the S) and vertical (on the right; positive upwards) directions. Displacement values on these maps are relative. To deal with computational limitations, processing is divided into two geographical zones, N and S. The artifact visible in the E-W direction mainly, close to N42°48', is due to an uncorrected ramp between those two zones. As all measurements are made in the N zone, this ramp, of relatively low amplitude (e.g. ~1 px in the E-W deformation map), should not affect measurements made within distances of ~200 m.

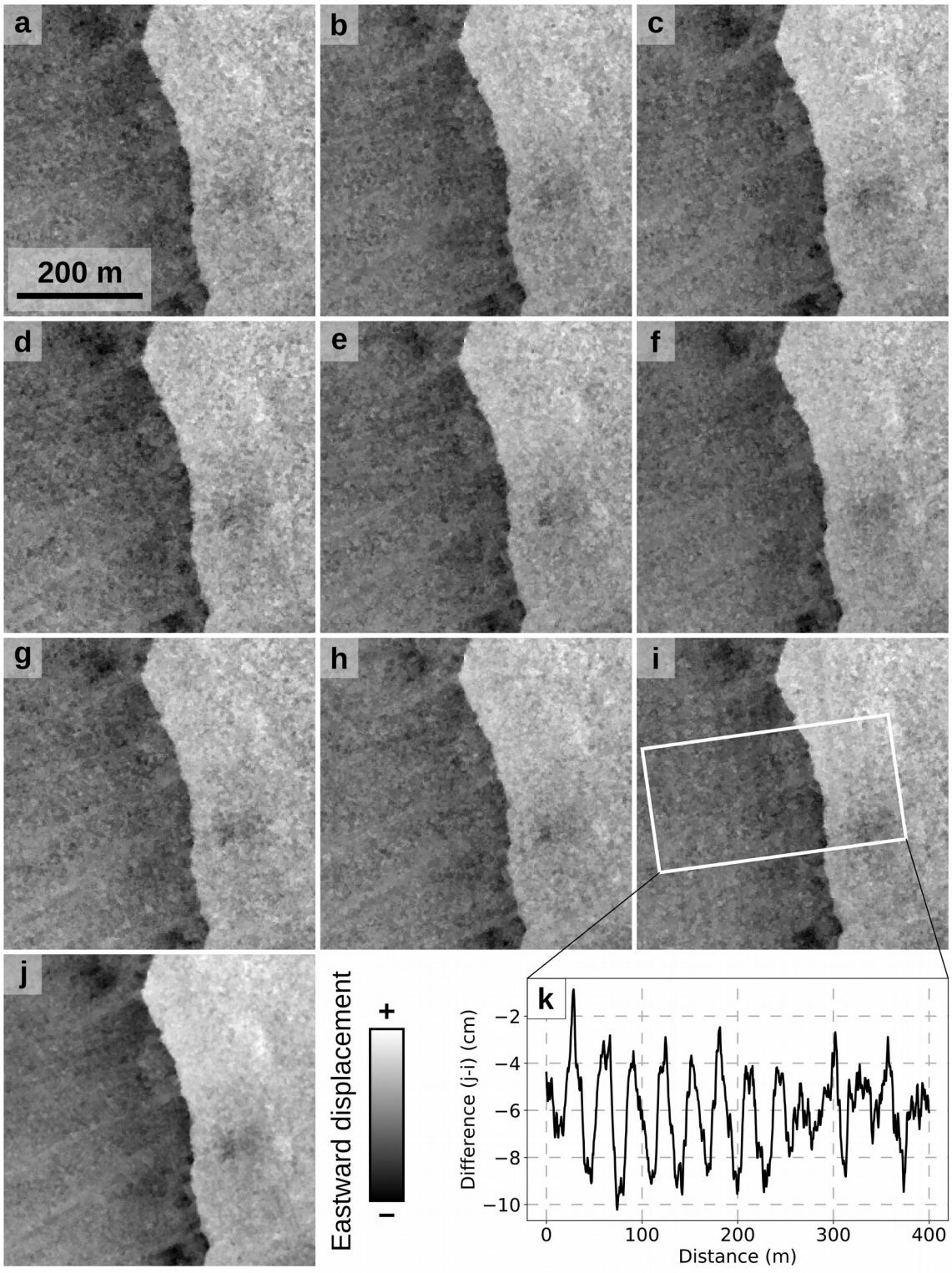

Figure S2. (a)-(i) Close-up view of rupture #04, in the Monte Vettore area, of the nine E-W horizontal surface deformation maps – one for each pair of pre- and post-earthquake orthoimages – processed from the Pleiades data. Spatial aliasing is clearly visible in some of the maps (e.g. map (i)), which affects the

tectonic signal. (j) Map of average deformation obtained by weighted average of the nine maps, with the correlation score produced during the correlation steps used as the weight. Noise, including aliasing, is reduced while tectonic signal is well preserved. Note that topographic artifacts, visible in the direction almost perpendicular to the rupture, which correspond to the drainage network, are also well preserved. (k) Difference between stacked profiles performed in map (i) and in map (j), in the direction perpendicular to the aliasing visible in (i). The amplitude of the aliasing is of ~6-8 cm, which is not negligible in comparison with the ~55 cm of strike-perpendicular tectonic signal measured across the fault.

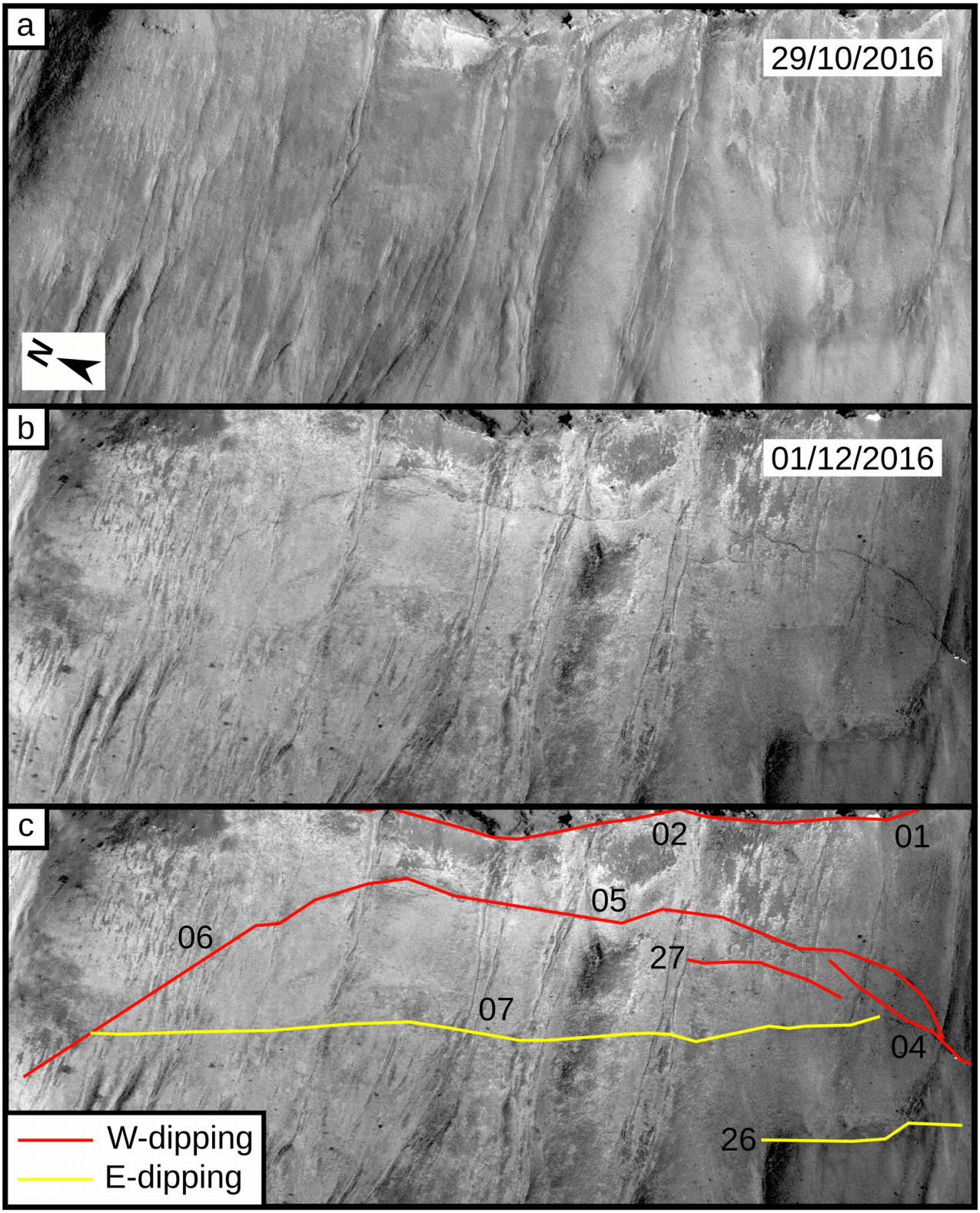

Figure S3. Close-up view on the Monte Vettore western flank showing (a) the pre-earthquake Pleiades orthoimage, (b) the post-earthquake Pleiades orthoimage, on which the coseismic ruptures are visible. (c) The mapping of the coseismic ruptures (W-dipping in red, E-dipping in yellow) is superimposed over the post-earthquake image. The ruptures are numbered in the same way as in Figure 3.

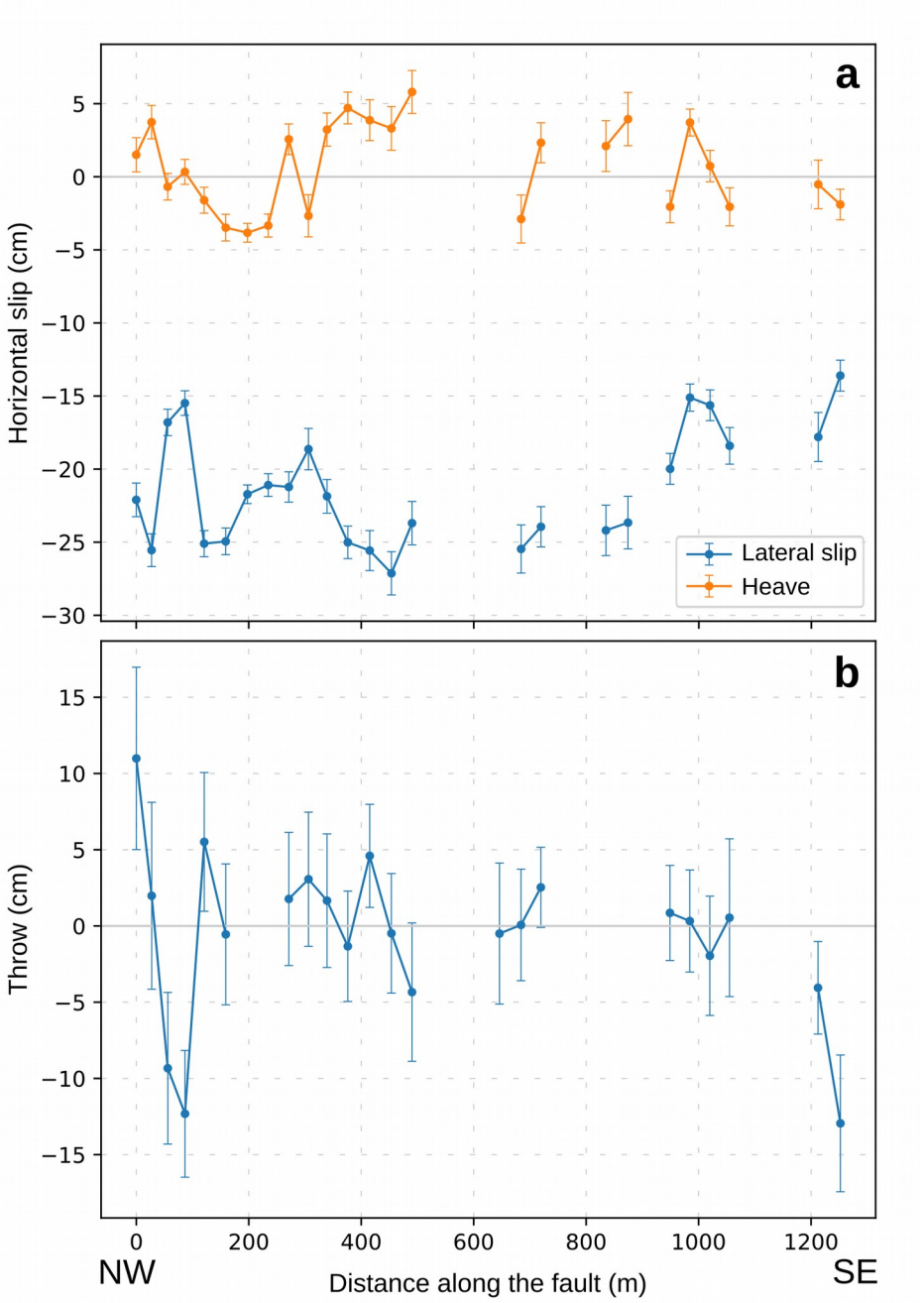

Figure S4. (a) Lateral slip, heave and (b) throw measured along a 1.3-km-long rupture of azimuth N140°E, located on Monte Castello, SW of Piano Grande (Figure 1b). The E-W and N-S measurements are projected in the strike-perpendicular and along-strike directions, relatively to the rupture mean azimuth, which is obtained through linear regression of the measurements locations ($r^2 = 0.999$). Displacement along this fault is characterized by right-lateral strike-slip.

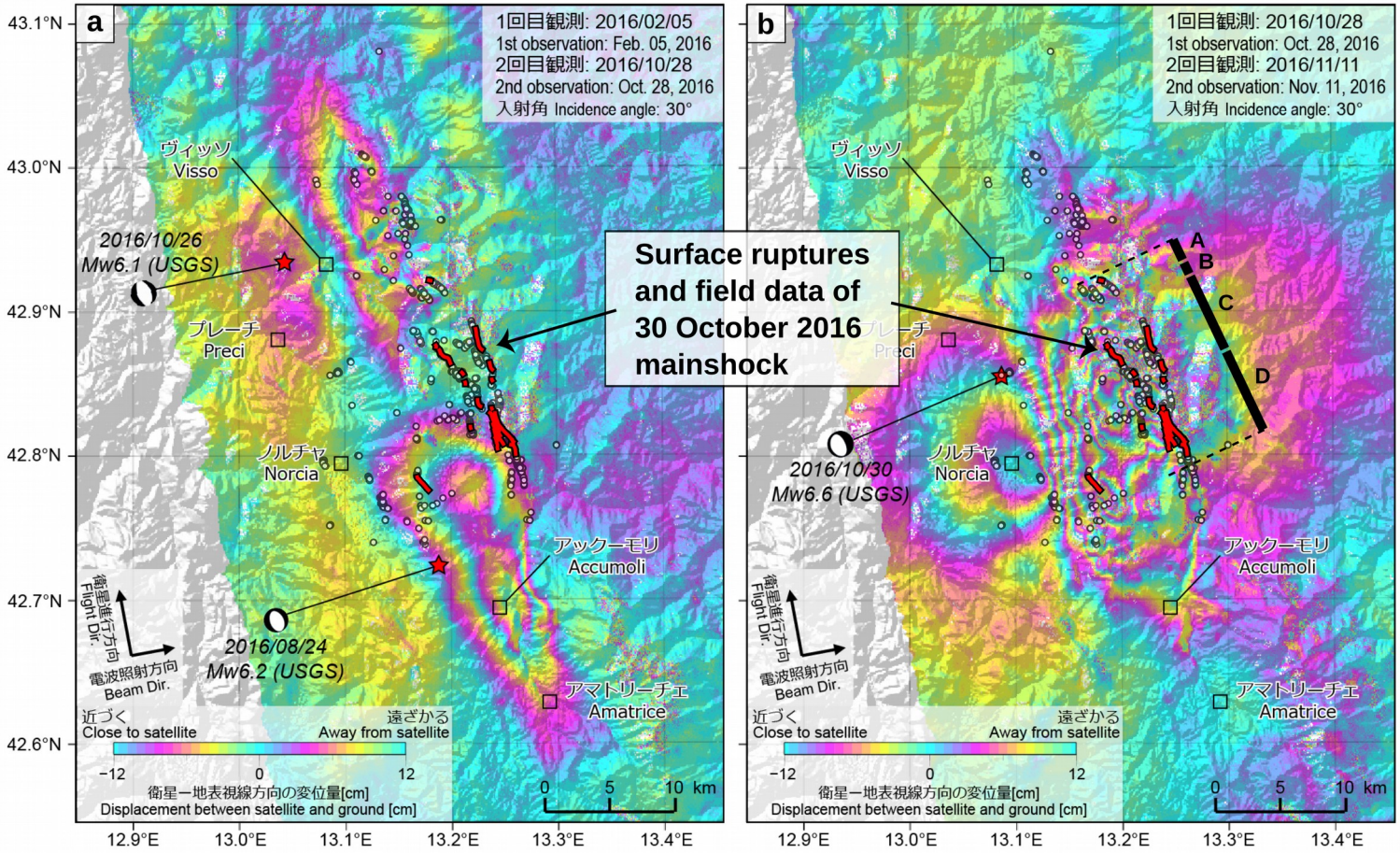

Figure S5. Interferograms from the analysis by GSI of ALOS-2 raw data from JAXA (http://www.gsi.go.jp/cais/topic161108-index-e.html). (a) Interferogram between the 05 February and the 28 October 2016, showing the areas deformed during both the 24 August Amatrice and the 26 October Visso earthquakes. (b) Interferogram between the 28 October and the 11 November 2016 that captured the 30 October Norcia event. The area deformed during this third event is located between the two areas affected by the previous earthquakes and was not affected by those earthquakes. Coseismic surface ruptures mapped from the orthoimages, DSMs and deformation maps derived from the Pleiades images, which captured the 30 October event, are superimposed (in red) on both interferograms. Locations of the field measurements from Villani, Civico et al. (2018), collected between the 31 October 2016 and the 16 July 2017, are also indicated (white circles). Sections A, B, C and D along the baseline defined in Figure 3 are reported.

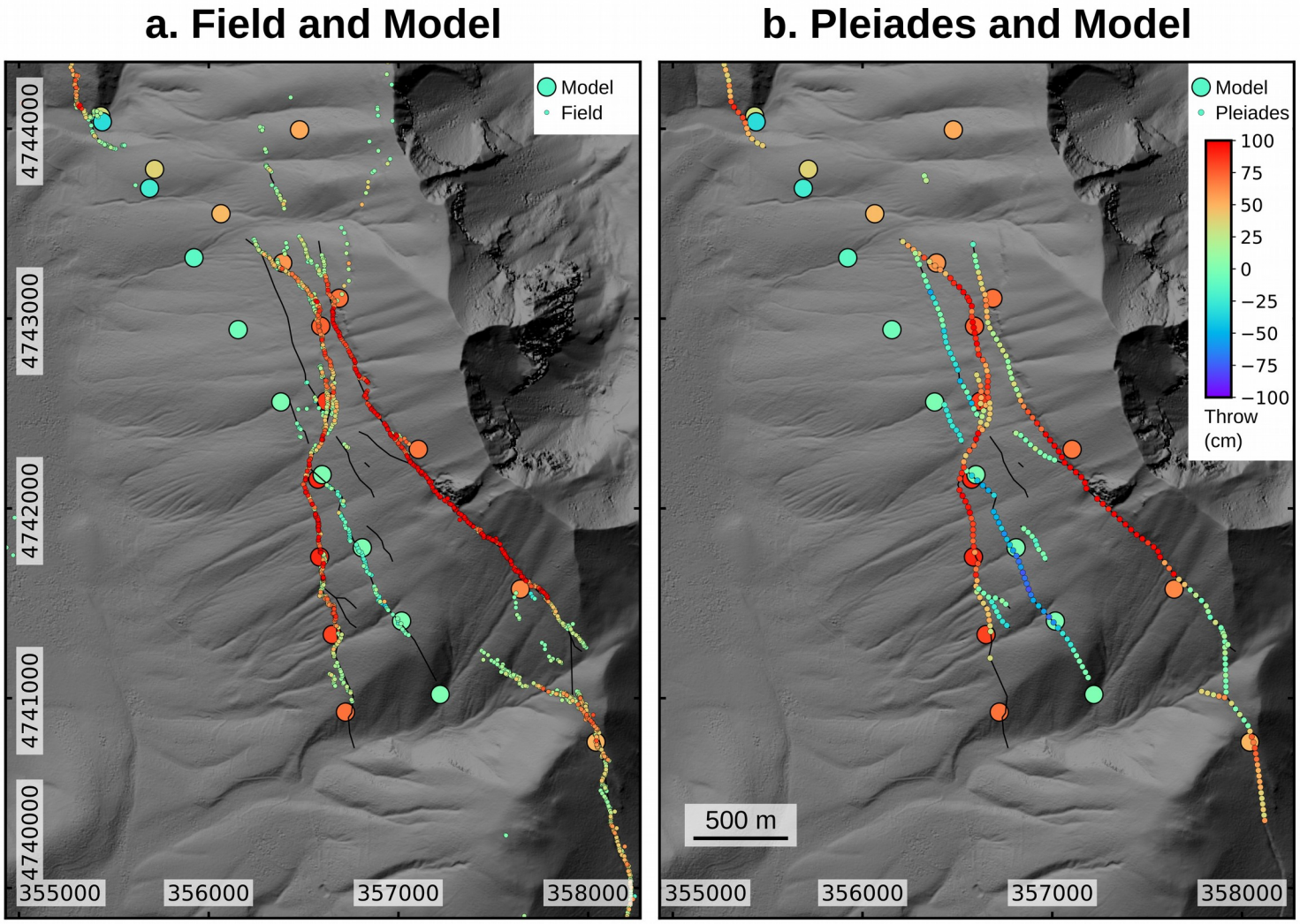

Figure S6. Close-up view of the Monte Vettore area (see location in Figure 1b). Comparison between throw at the surface deduced from the model – the big points represent the surface patches – and measured (a) in the field by Villani, Civico et al. (2018) and (b) in the Pleiades vertical deformation map. For normal faults, a positive (respectively negative) throw implies a dip toward the W (respectively E). In the background, shaded relief image of a 4 m resolution version of the post-event DSM processed from Pleiades. Pixels with poor correlation scores appear in black.

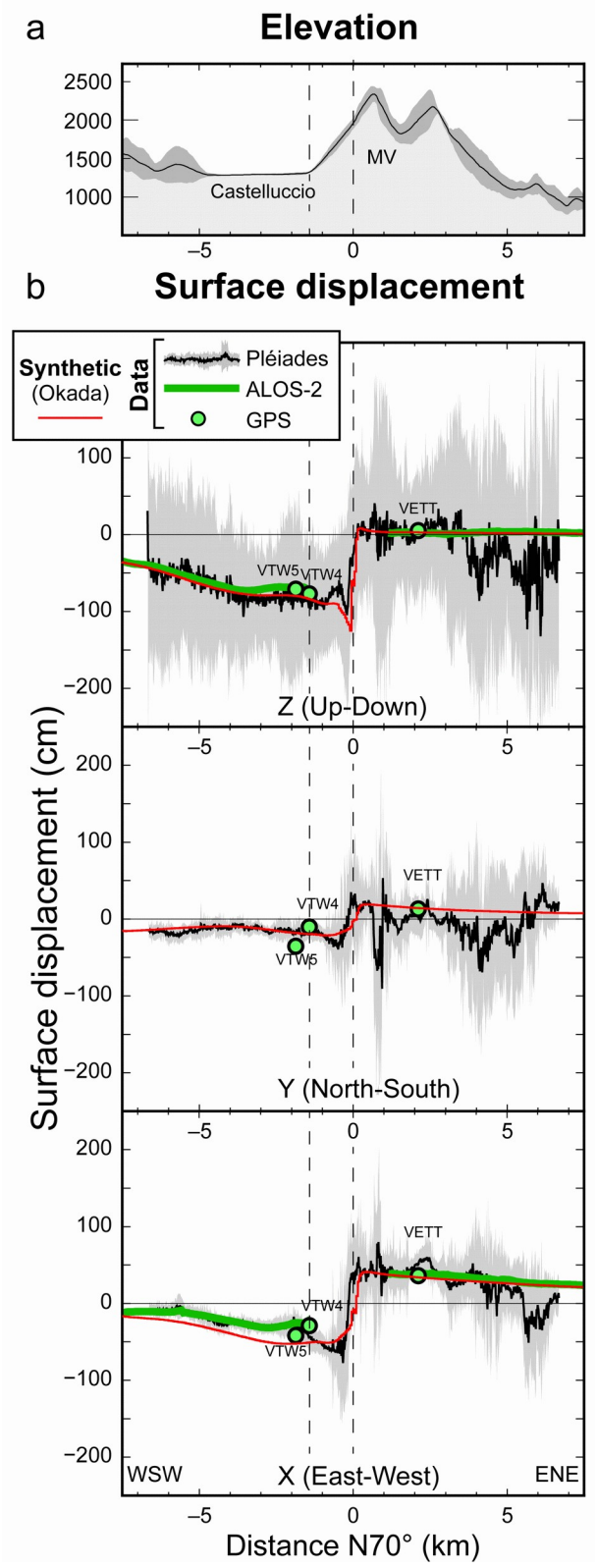

Figure S7. Surface displacement in the three dimensions (two dimensions for ALOS-2), extracted on a profile drawn across several ruptures (profile A-A' in Figure 5f). For the Pleiades results, stacked profiles are computed, centered on the main profile and with a width of 1.5 km, to improve the signal to noise ratio.

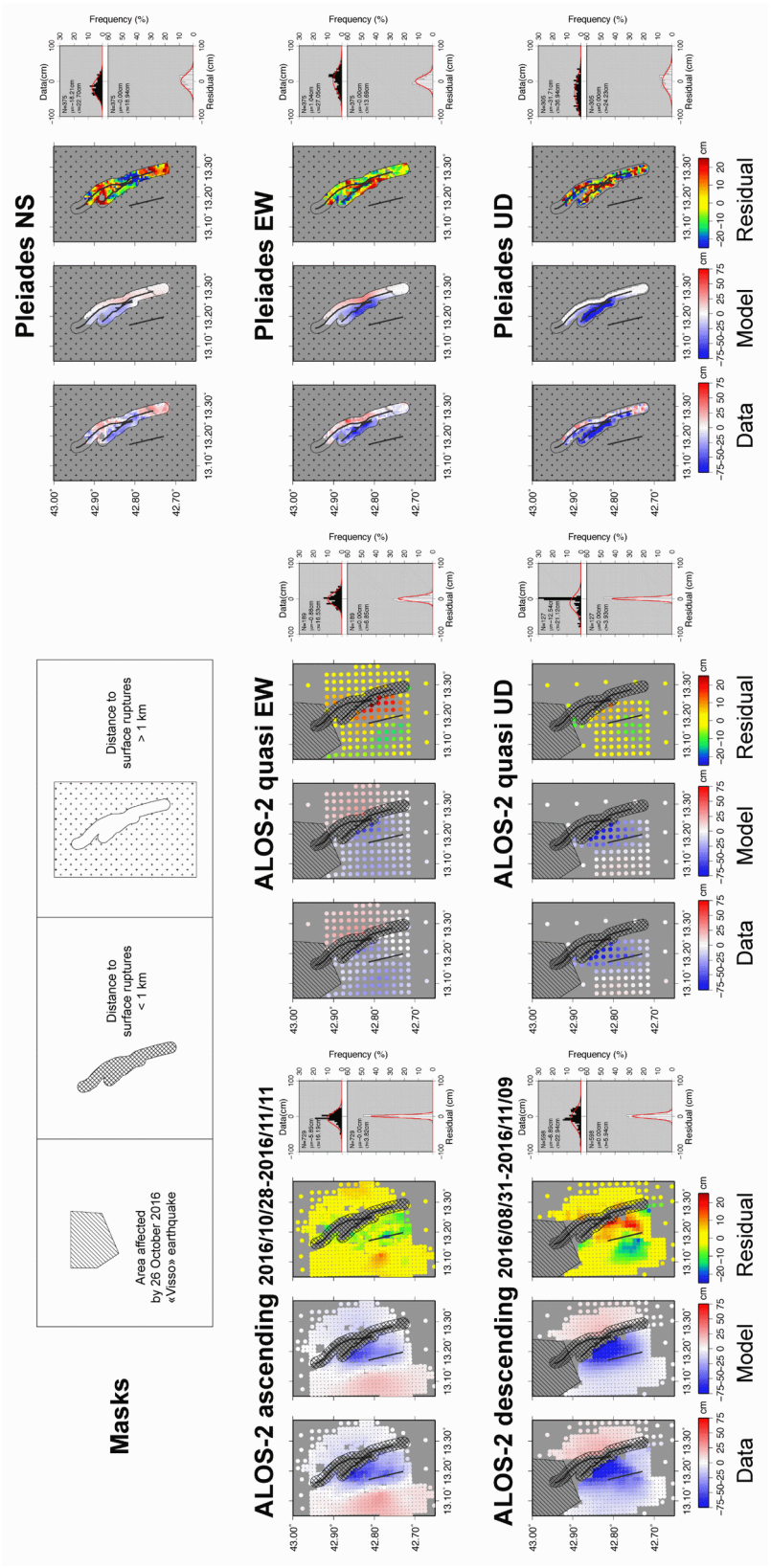

Figure S8. Comparison of observed surface deformation from ALOS-2 and Pleiades versus synthetic deformation predicted by the slip model. The colored points show the distribution of data points after masking and

decimation. The same color palette is used in all panels. Black and grey histograms represent the distribution of data and residuals, respectively, for each dataset.

2016-10-30 M6.5 Norcia earthquake
Moment Tensors

	Source	*Type*	*Moment*	*Mag*	*Depth*	*Strike_1*	*Dip_1*	*Rake_1*	*Strike_2*	*Dip_2*	*Rake_2*
a	USGS	W-phase	1,07E+019	6,63	15,5	162	27	-84	335	63	-93
b	USGS	Centroid	1,19E+019	6,66	15,9	139	41	-126	3	58	-63
c	USGS	Body-wave	6,71E+018	6,49	6,0	162	43	-68	313	51	-110
d	USGS	Regional	8,77E+018	6,57	5,0	161	29	-90	341	61	-90
e	IPGP	Scardec	7,29E+018	6,52	8,0	165	36	-80	332	54	-98
f	GFZ	MT	6,80E+018	6,50	10,0	152	44	-94	338	46	-84
g	INGV	Quick MT	9,00E+018	6,58	10,0	155	37	-98	345	53	-84
h	INGV	Moment Tensor	??	??	10,0	148	41	-104	346	51	-78
I	INGV	TDMT	7,07E+018	6,51	5,0	151	47	-89	330	43	-91
j	Harvard	GCMT	9,58E+018	6,59	12,0	154	37	-96	342	53	-85
k					AVERAGE	154,9	38,2	-92,9	302,5	53,3	-87,6

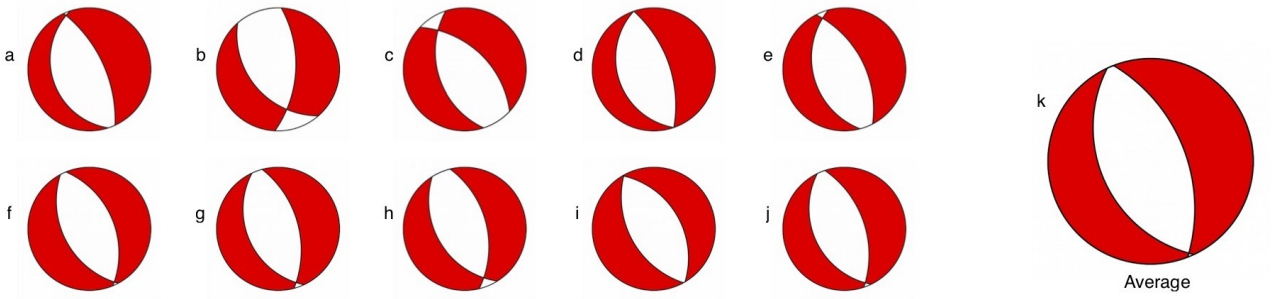

Figure S9. Compilation of the publicly available moment tensor solutions of the 30 October 2016 Mw6.5 Norcia earthquake.

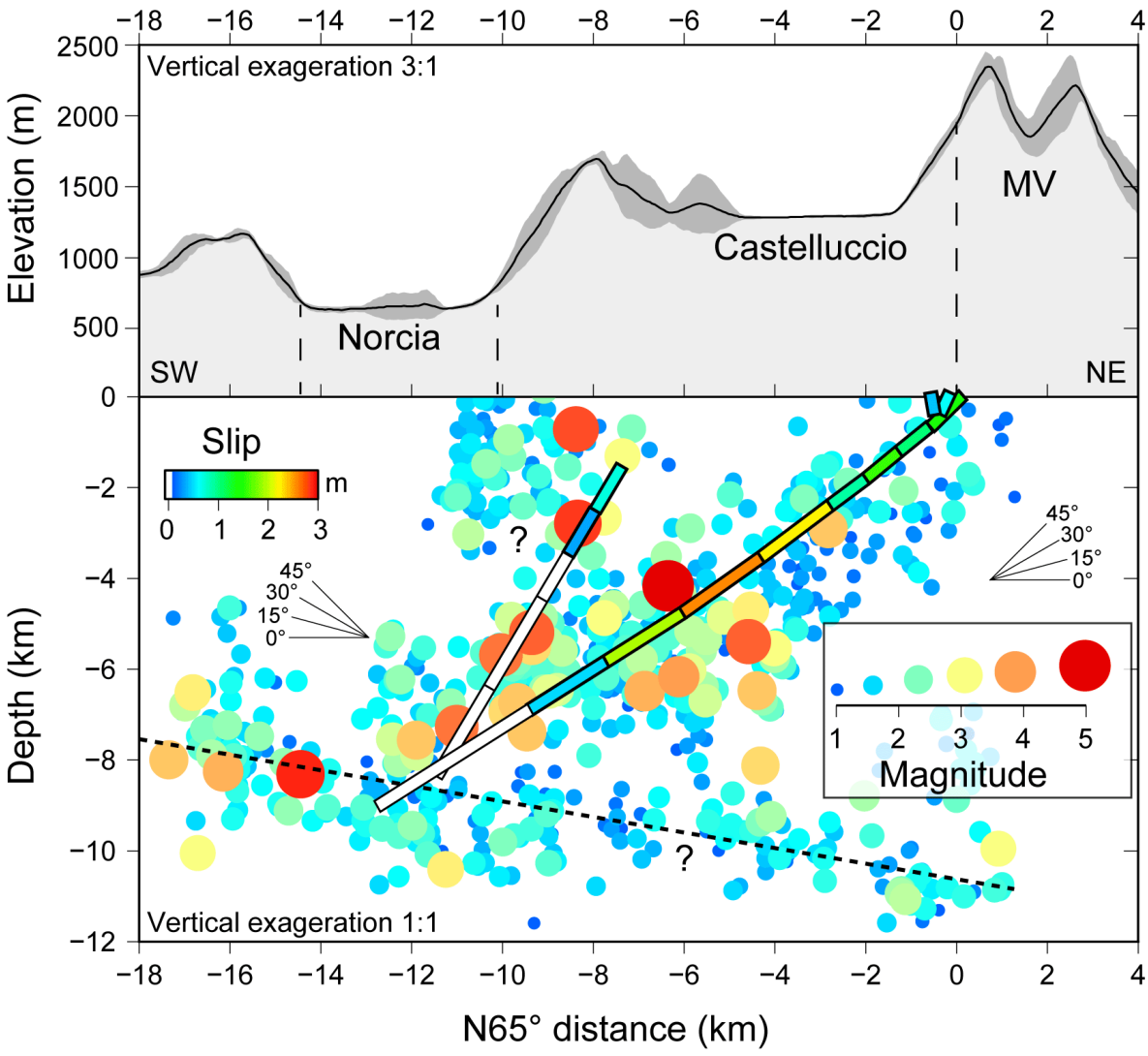

Figure S10. Cross-section perpendicular to the system showing the relative location of the modeled faults (shown as colored bars, with color representing the modeled coseismic slip) and relocated seismicity reported by Chiaraluce et al. (2017) for the period between 01 October and 29 November 2016 (keeping only earthquakes with magnitudes greater than 1). Upper panel shows topography along the cross-section. Cross-section location is indicated in Figure 5f (profile A-A').

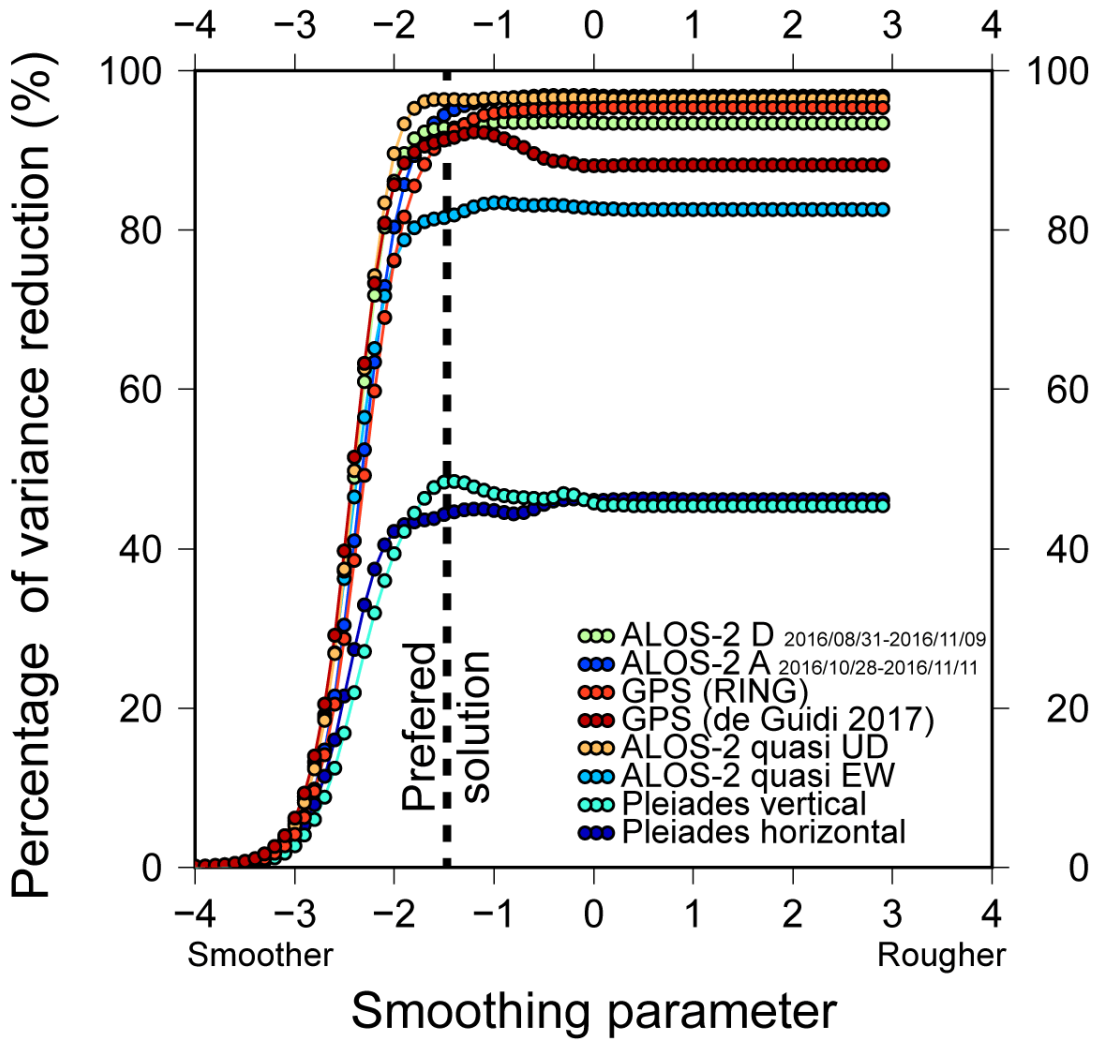

Figure S11. Exploration of model roughness *versus* fit-to-the-data. Each dataset is represented with a different color. The preferred solution is indicated by the vertical dashed line.

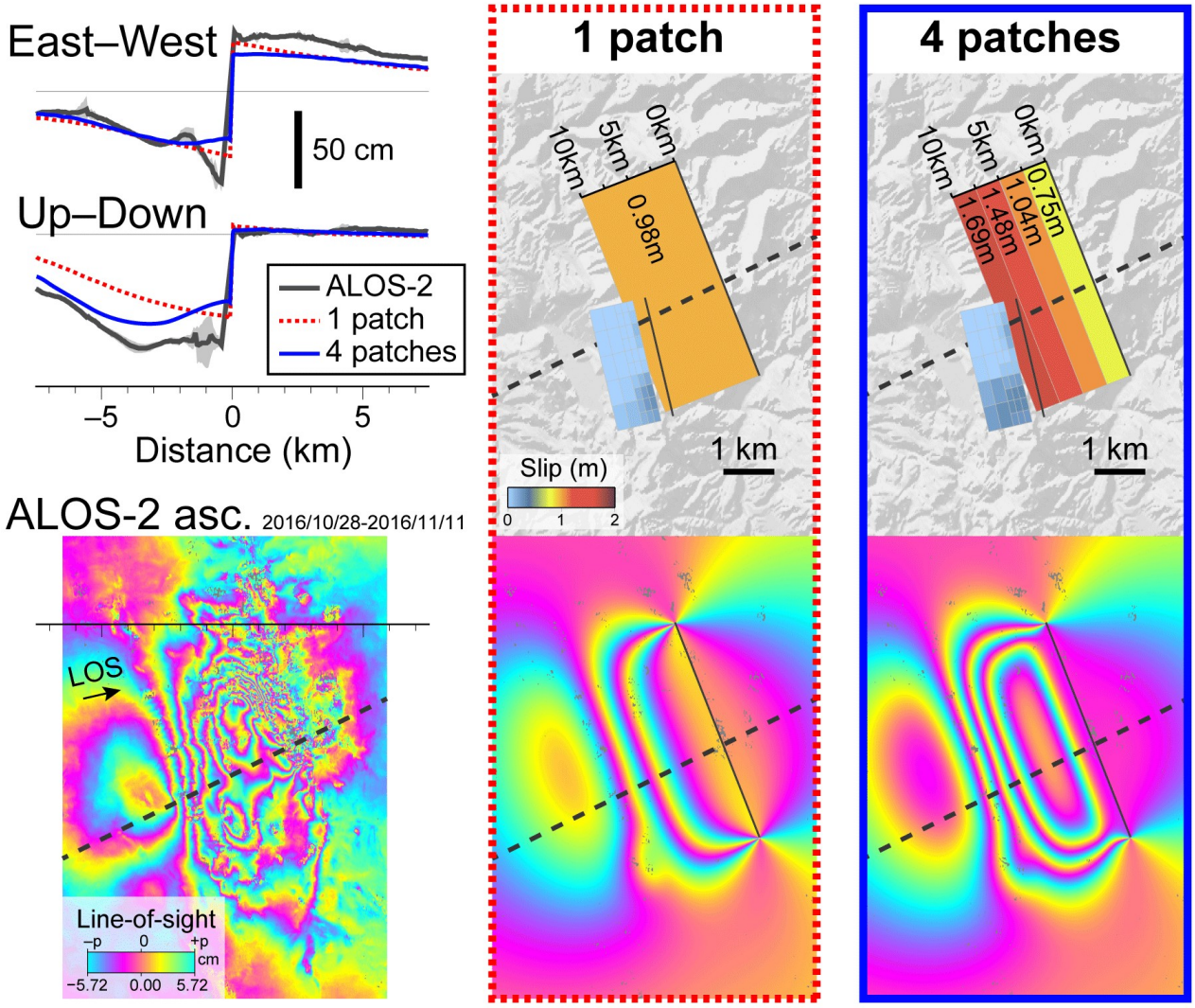

Figure S12. Synthetic tests of first-order slip distribution of the 30 October 2016 Norcia earthquake. Observations of E-W, up-down and line-of-sight displacement from ALOS-2 are compared with predictions from two alternative scenarios. Red: the MVF consists in a single patch with uniform slip. Blue: the fault is divided in four patches evenly distributed along-dip, slipping with an increasing magnitude toward the surface. A significantly improved fit to the observations, both in map view and in cross-section, is achieved for the model accounting for a slip decrease toward the surface.

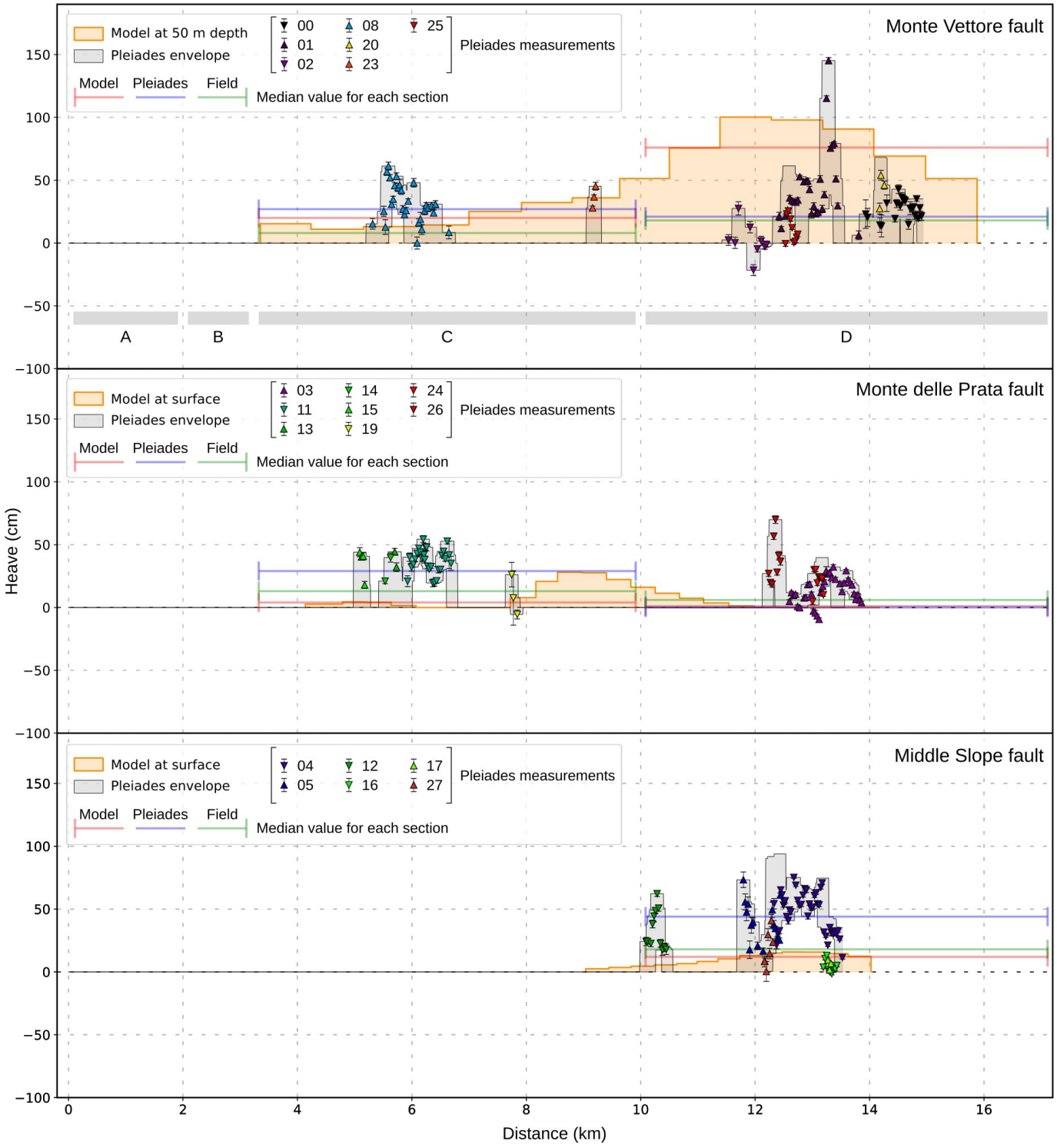

Figure S13. Heave at the surface, measured on the Pleiades horizontal deformation maps (colored triangles) and stemmed from modeling (surface patches are represented by light orange step curves). Each set of Pleiades measurements – one set by rupture mapped – is assigned to one of the three main fault systems – MVF, MPF and MSF – used as an input in the inversion (Figure 3a). Each measurement location and each model patch location is projected along a baseline of azimuth N155°E (Figure 3a). For each Pleiades

measurement, the strike-perpendicular direction used is relative to the azimuth of the corresponding model patch. A positive (respectively negative) heave indicates extension (respectively compression). Regarding the Pleiades measurements, in order to facilitate comparison with the model, minimum and maximum cumulative slip envelopes (light grey step curves) are computed, to estimate the total slip over multiple sub-parallel ruptures as a function of the distance along the baseline (see Figure S16 for the method used). For each section A, B, C and D, the median value is represented for the model (red line), the Pleiades measurements (blue line) and the field observations (green line).

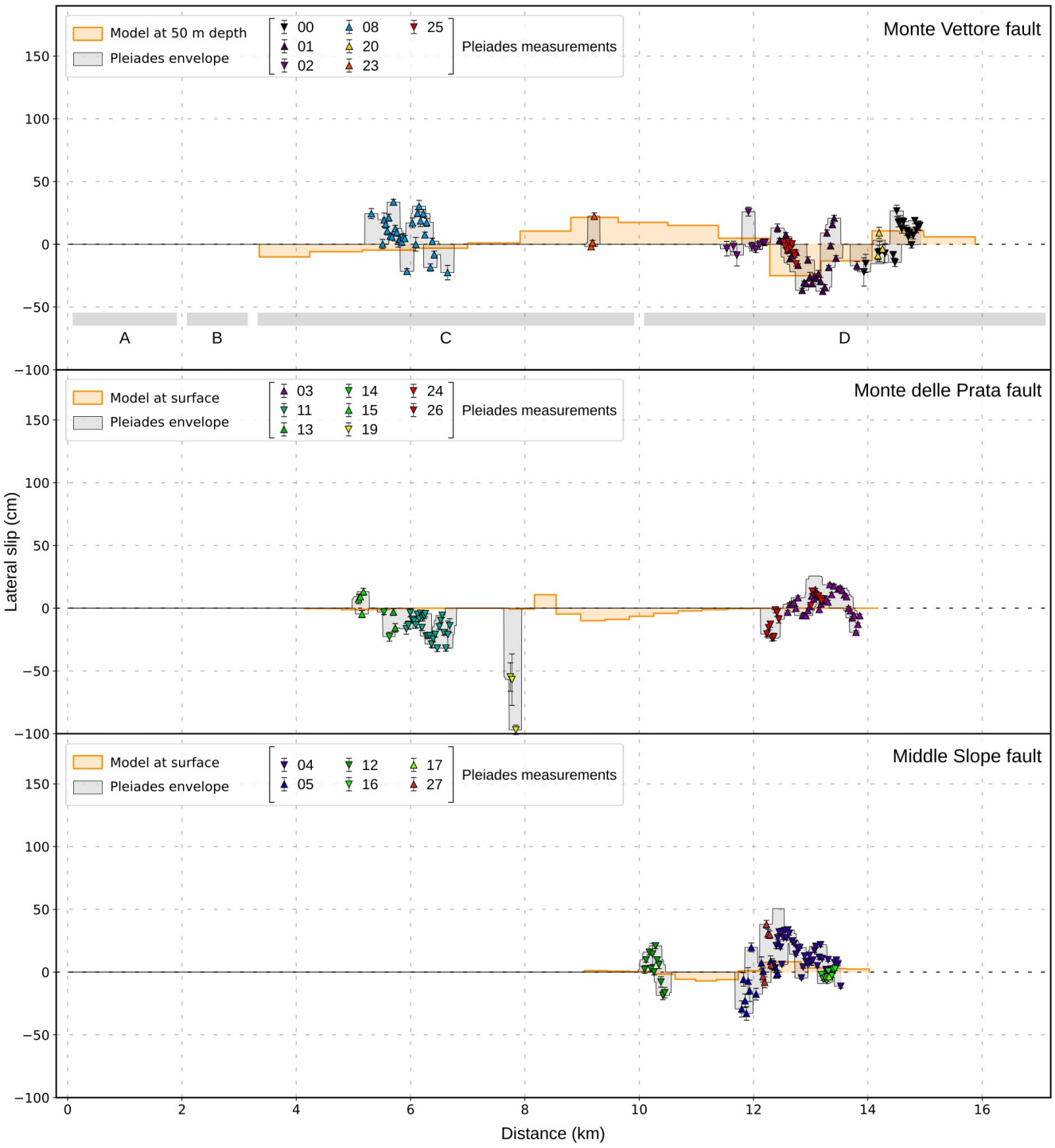

Figure S14. Lateral slip at the surface, measured on the Pleiades horizontal deformation maps (colored triangles) and stemmed from modeling (surface patches are represented by light orange step curves). Each set of Pleiades measurements – one set by rupture mapped – is assigned to one of the three main fault systems – MVF, MPF and MSF – used as an input in the inversion (Figure 3a). Each measurement location and each model patch location is projected along a baseline of azimuth N155°E (Figure 3a). For each Pleiades measurement, the along-strike direction used is relative to the azimuth of the corresponding model patch. A positive (respectively negative) lateral slip

indicates a left-lateral (respectively right-lateral) motion. Regarding the Pleiades measurements, in order to facilitate comparison with the model, minimum and maximum cumulative slip envelopes (light grey step curves) are computed, to estimate the total slip over multiple sub-parallel ruptures as a function of the distance along the baseline (see Figure S16 for the method used).

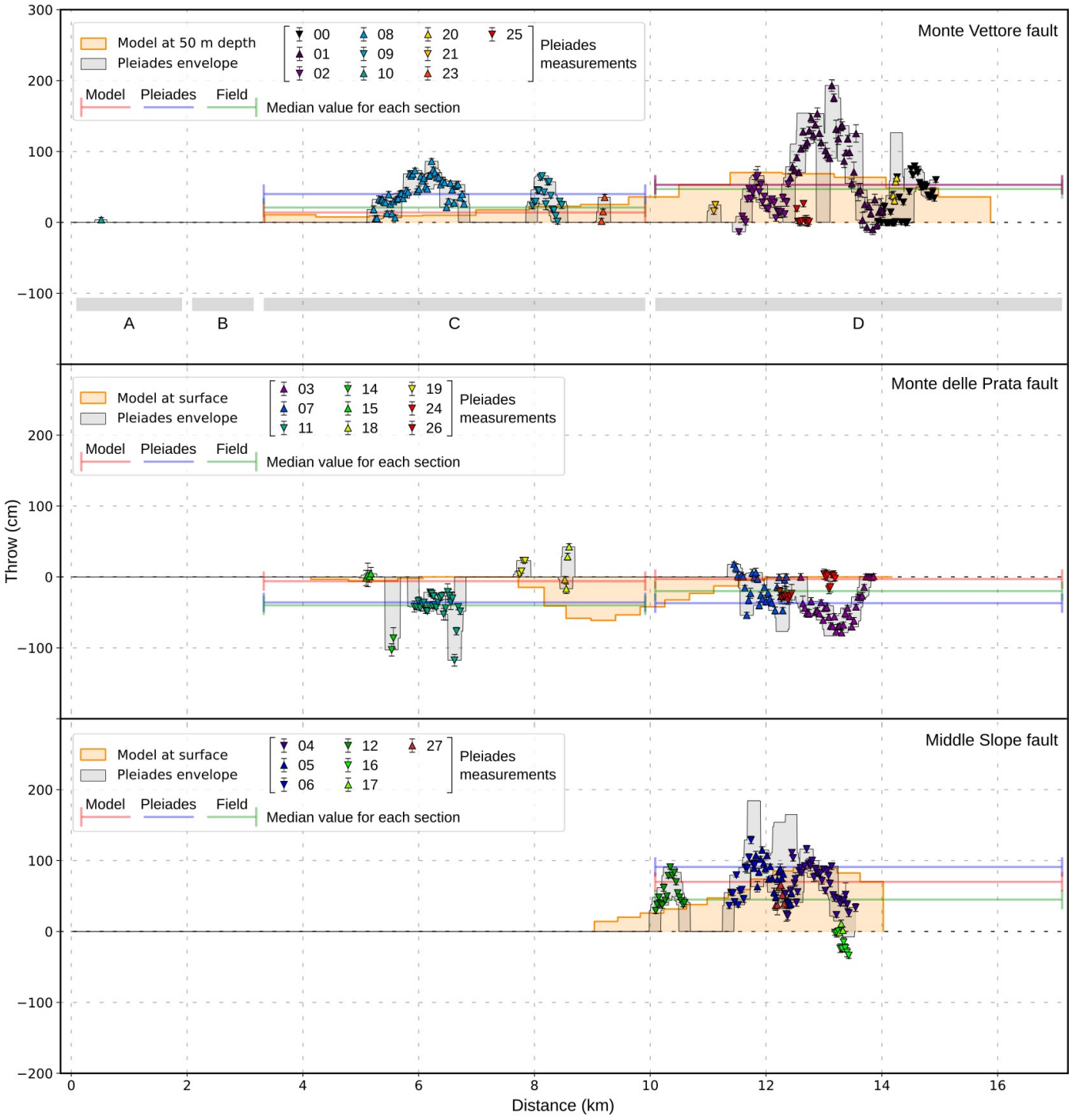

Figure S15. Throw at the surface, measured on the Pleiades vertical deformation map (colored triangles) and stemmed from modeling (surface patches are represented by light orange step curves). Each set of Pleiades measurements – one set by rupture mapped – is assigned to one of the three main fault systems – MVF, MPF and MSF – used as an input in the inversion (Figure 3a). Each measurement location and each model patch location is projected along a baseline of azimuth N155°E (Figure 3a). For normal faults, a positive (respectively negative) throw implies a dip toward the W (respectively E). Regarding the Pleiades measurements, in order to facilitate comparison with the model, minimum and maximum cumulative slip

envelopes (light grey step curves) are computed, to estimate the total slip over multiple sub-parallel ruptures as a function of the distance along the baseline (see Figure S16 for the method used). For each section A, B, C and D, the median value is represented for the model (red line), the Pleiades measurements (blue line) and the field observations (green line).

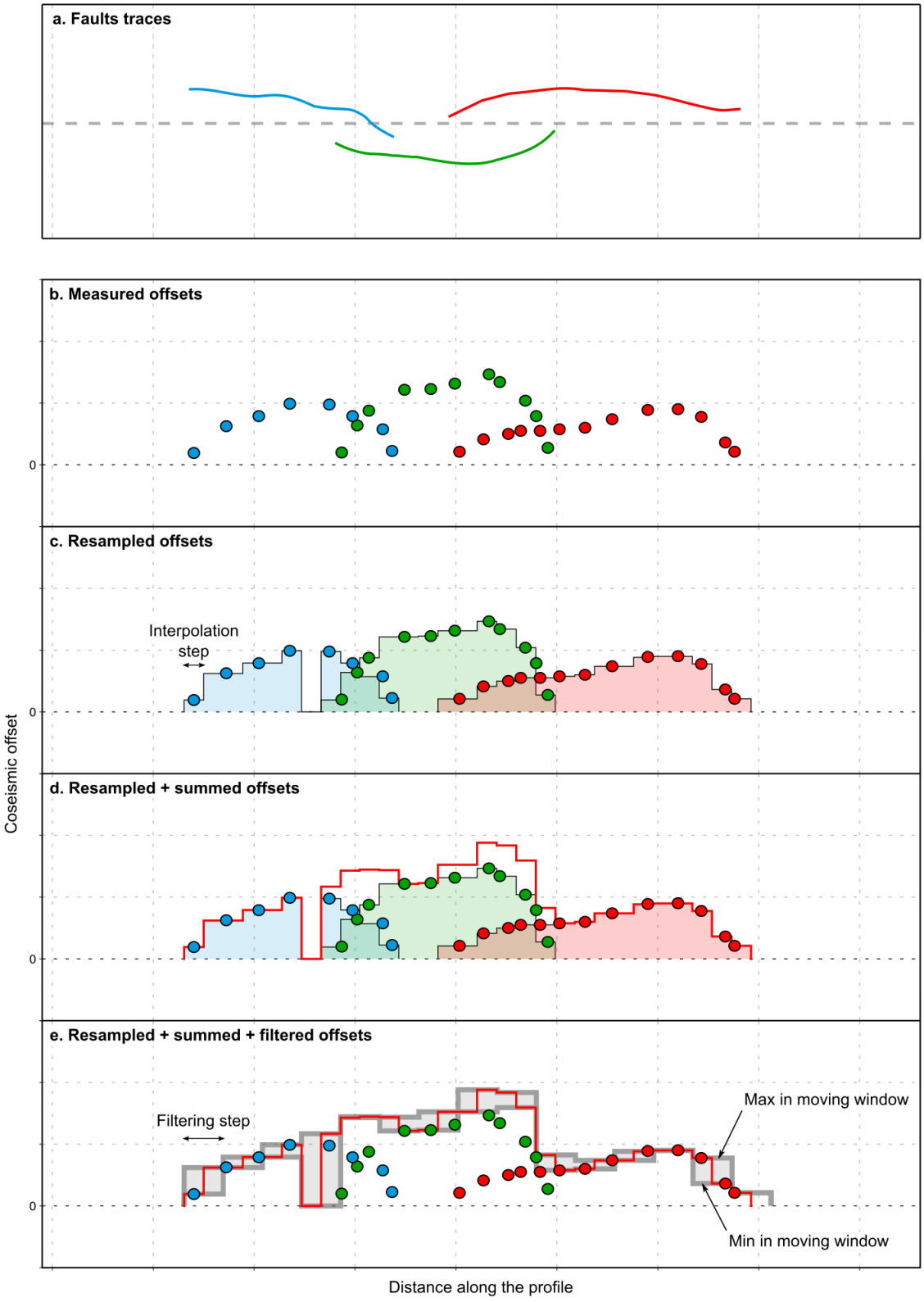

Figure S16. Method used to generate the minimum and maximum cumulative slip envelopes from the offset measurements derived from Pleiades. (a) Map of three sub-parallel surface ruptures (colored lines) and of the baseline on which the measurements are projected (grey dashed line). (b) Plot of the measured offsets as a function of the distance along the baseline. (c) Nearest neighbour interpolation is used to obtain a regular sampling

(represented by the step curves) from the isolated measurements. (d) The step curves are added up to generate a curve of cumulative slip. (e) A sliding window of defined width is used to filter the cumulative slip curve. This step is done twice to select consecutively the local minima and maxima, to produce minimum and maximum cumulative slip envelopes (in grey).

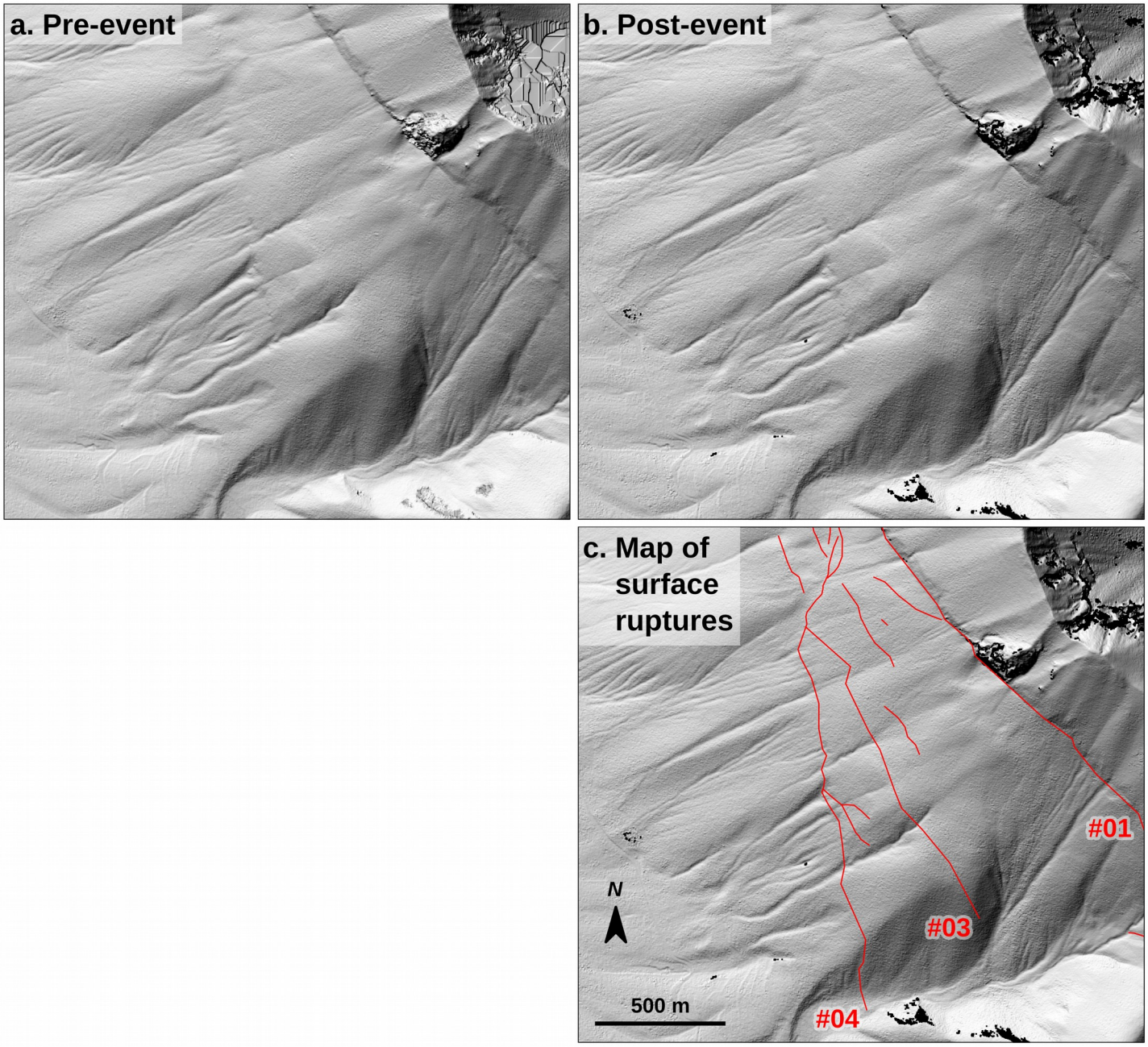

Figure S17. Close-up view of shaded relief images of the (a) pre- and (b) post-event Pleiades DSMs, located on the western slope of Monte Vettore. (c) Mapped surface ruptures corresponding to the 30 October 2016 Norcia earthquake are represented on the post-event shaded DSM (in red). Surface ruptures #01 and #04, attributed to the MVF and MSF, respectively, are easy to follow in the pre-event morphology, thanks to topographic steps across the faults and erosion caused by water flows, which appear in the slope just below the ruptures. Surface rupture #03, attributed to the MPF, is partly discernible in the pre-event morphology, as are some other secondary ruptures. This indicates that those ruptures have already recorded at least one slip episode before being activated during this earthquake. Ruptures #03 and #04 delimit a horst, which is incised by water flows coming from above.

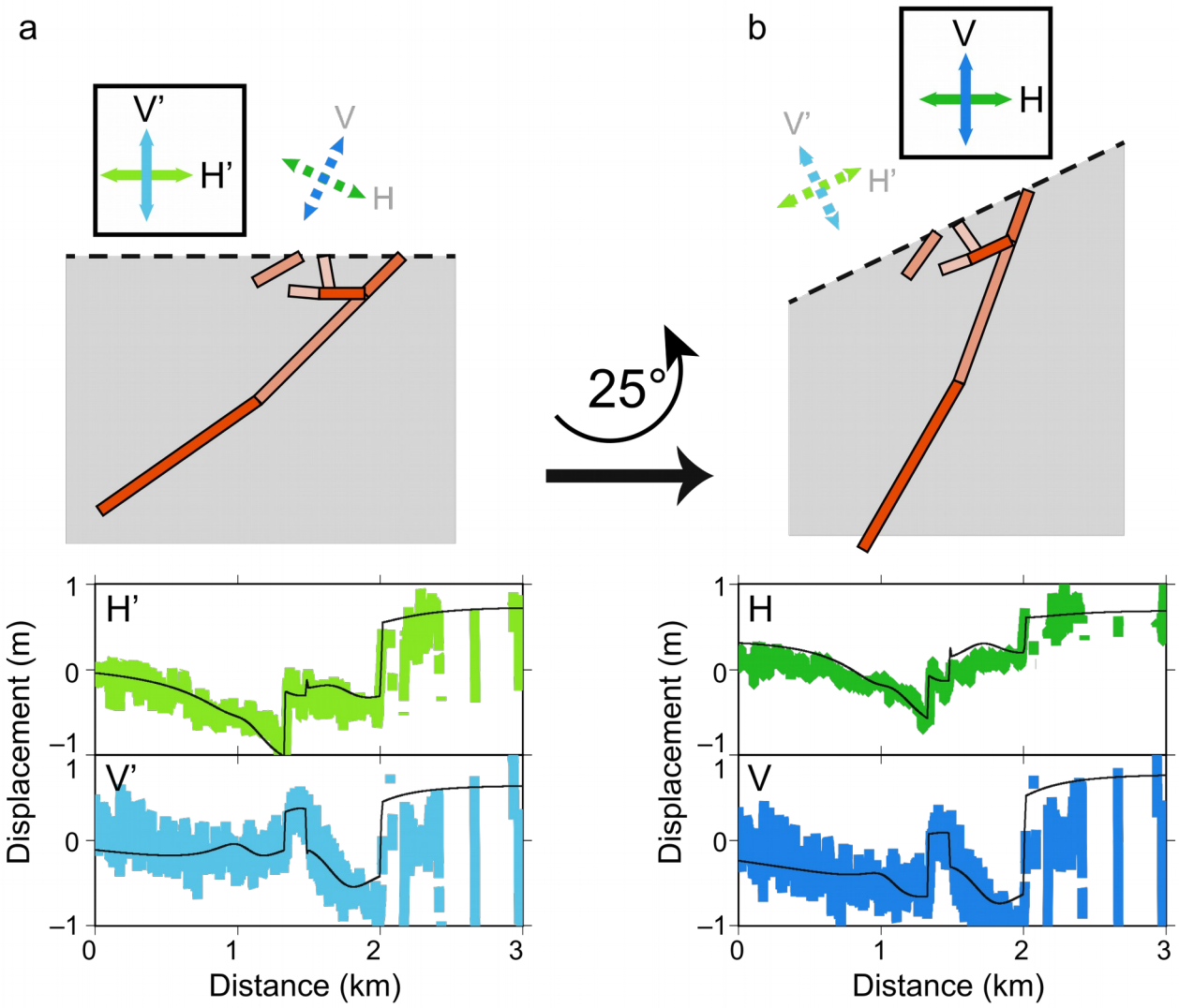

Figure S18. Summary of the methodology used to account for a sloping free surface. Left: a standard Okada simulation is carried out, after correcting fault dips so that the dip angle of the fault is equal to the relative angle between the fault and the actual local topography. This step is equivalent to rotating the dislocations clockwise about their point of intersection with the surface. Right: at post-processing stage, surface-parallel and surface-perpendicular displacements are combined to extract the horizontal and vertical components of displacement. This step is equivalent to defining a new coordinate system rotated clockwise with respect to the coordinate system used in the standard Okada simulation.

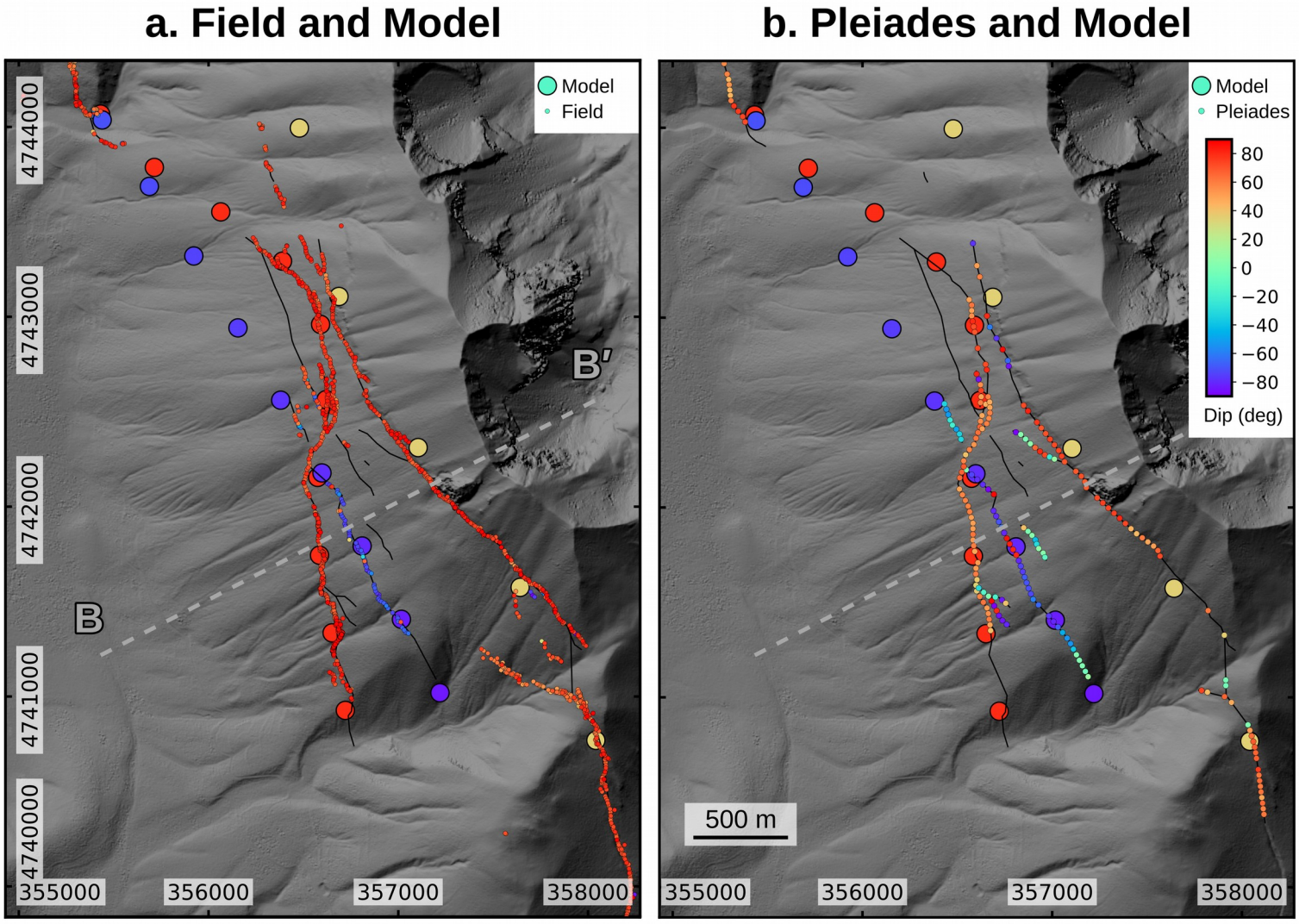

Figure S19. Close-up view of the Monte Vettore area (see location in Figure 1b). Comparison between dip at the surface deduced from the model – the big points represent the surface patches – and from the measurements made (a) in the field by Villani, Civico et al. (2018) and (b) in the Pleiades deformation maps. In this figure, dips toward the W (respectively E) are represented with positive (respectively negative) values. Profile B-B’ from Figure 7 is represented by a grey dashed line. In the background, shaded relief image of a 4 m resolution version of the post-event DSM processed from Pleiades. Pixels with poor correlation scores appear in black.

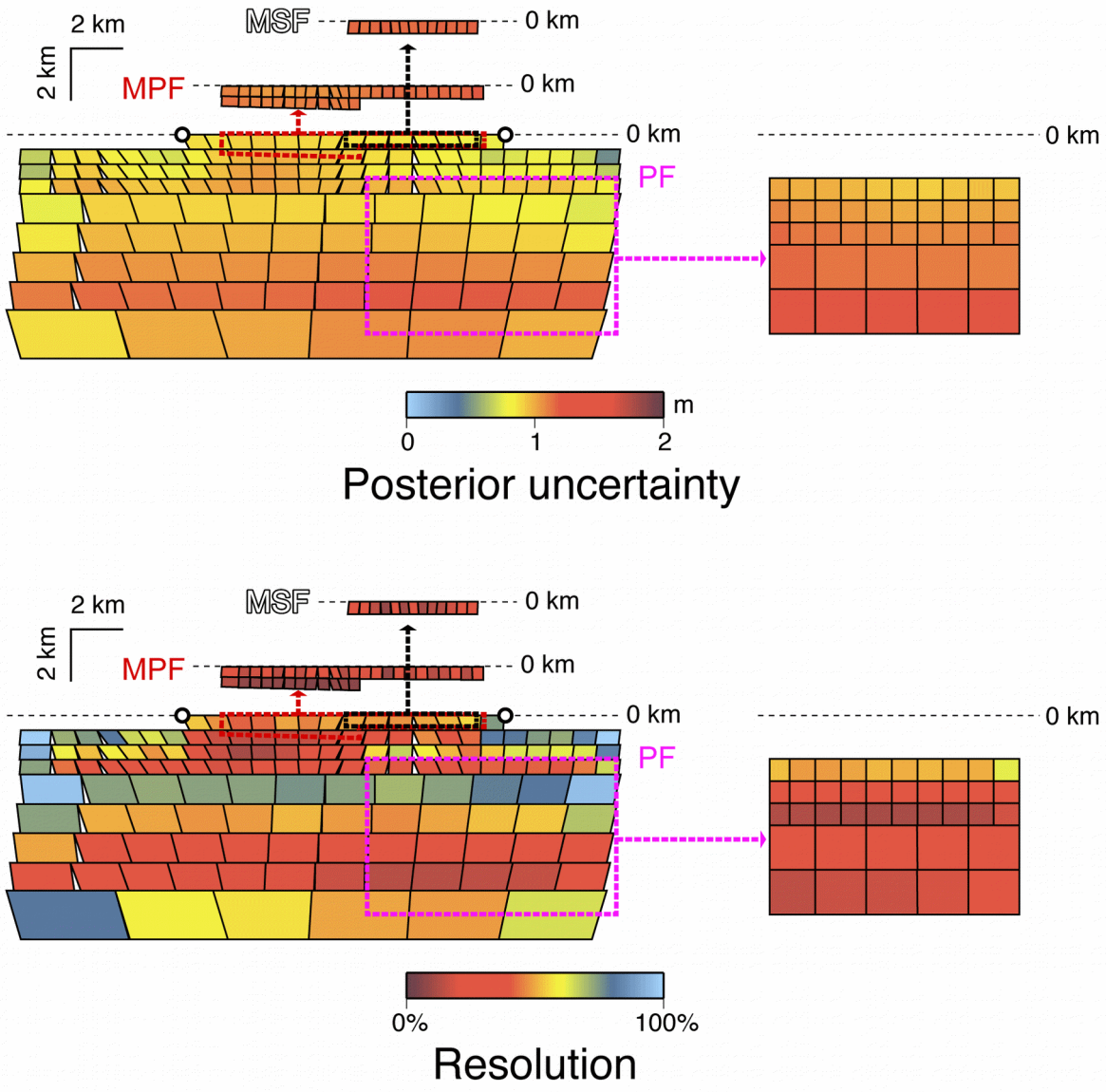

Figure S20. Uncertainties on slip inversions estimated following the approach of Tarantola (2005). Top: Diagonal terms of the posterior model covariance matrix (Eq. 3.38 of Tarantola (2005)). Bottom: Diagonal terms of the resolution operator (Eq. 3.63 of Tarantola (2005)).

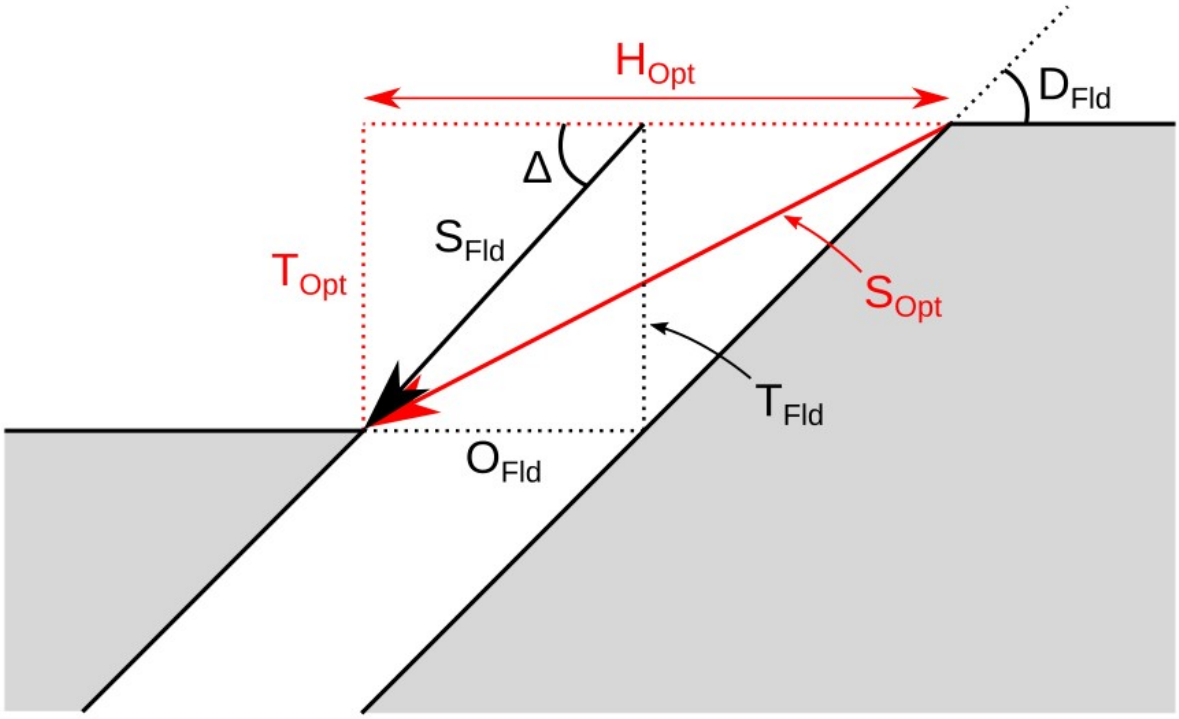

Figure S21. Throw (T_{Fld}), opening (O_{Fld}) and dip angle (D_{Fld}) values were collected in the field by Villani, Civico et al. (2018). Δ is the dip of the dip-slip vector (S_{Fld}), sum of T_{Fld} and O_{Fld}. Measurement points for which the difference Δ-D_{Fld} exceeds 10° are filtered out. Throw (T_{Opt}), heave (H_{Opt}), from the Pleiades optical data, and the dip-slip vector (S_{Opt}), sum of T_{Opt} and H_{Opt} are represented in red.

	Zone N		Zone S	
	Residuals before	**Residuals after**	**Residuals before**	**Residuals after**
Pre-event image 1	0.7323	0.2644	0.7900	0.2715
Pre-event image 2	1.0714	0.3323	0.9578	0.2744
Pre-event image 3	1.1297	0.3046	1.2647	0.3165
Post-event image 1	1.6538	0.3487	1.6770	0.3998
Post-event image 2	1.8199	0.3389	1.6959	0.3578
Post-event image 3	2.2059	0.3112	2.2696	0.3857

Table S1. Re-projection residuals (in pixels) of the tie points between the images, before and after the BBA, for both zones. Each value is the mean residual of all tie points within an image. For each image, almost all the tie points (> 99.9%) are preserved over iterations.

Table S2. (separate file Table_S2.csv) Heave and lateral slip offset measurements performed on the Pleiades horizontal deformation maps. The field “rupture_id” corresponds to the ruptures mapped in Figure 3a.

Table S3. (separate file Table_S3.csv) Throw offset measurements performed on the Pleiades vertical deformation map. The field “rupture_id” corresponds to the ruptures mapped in Figure 3a.

Fault	X coordinate (km)	X relative displacement (cm)	Z relative displacement (cm)	Dip-slip (cm)	Dip angle
Monte Vettore	2.00	44	113	121	69° (toward the W)
Monte delle Prata	1.48	19	-44	48	67° (toward the E)
Middle Slope	1.34	54	71	89	53° (toward the W)

Table S4. Parameters for dislocations intersecting the surface along profile B-B’ (see Figure 7). Dip-slip and dip angle are calculated from the X (profile-parallel) and Z (vertical) relative displacements.

Fault system	Quantity (and %) of observations with opening and throw values	Quantity (and %) of observations with no opening and/or throw values, but offset, plunge and rake values	Quantity (and %) of observations with no opening and/or throw values, with offset and plunge values, but no rake value
Monte Vettore	537 (83%)	40 (6%)	71 (11%)
Monte delle Prata	262 (74%)	15 (4%)	78 (22%)
Middle Slope	193 (82%)	0 (0%)	42 (18%)

Table S5. Quantity and proportion of field observations of the different categories considered, for which: (1) the opening and throw values are provided; (2) the opening and/or throw values are missing, but offset, plunge and rake values are provided; (3) the opening and/or throw values are missing, offset and plunge values are provided, but the rake value is missing.